Investigations of Metal Assisted Titanium Dioxide (TiO_2) Nanocrystals

Thesis

Submitted to

Delhi Technological University

in partial fulfilment for the requirements for the degree of

DOCTOR OF PHILOSOPHY

in

APPLIED PHYSICS

by

Mrityunjay Kumar Singh

(Reg. No. 2K16/Ph.D./AP/04)

Under the Supervision

of

Dr. Mohan Singh Mehata

Assistant Professor

DEPARTMENT OF APPLIED PHYSICS
DELHI TECHNOLOGICAL UNIVERSITY
DELHI-110 042, INDIA

SEPTEMBER-2021

Dedicated to…
My beloved family

DECLARATION

I hereby declare that the work presented in this thesis entitled ***"Investigations of Metal Assisted Titanium Dioxide (TiO_2) Nanocrystals"*** submitted to the Delhi Technological University (DTU), Delhi for the award of degree of ***"Doctor of Philosophy"*** in Applied Physics is a record of bonafide original research work carried out by me under the supervision of Dr. Mohan Singh Mehata, Assistant professor, Department of Applied Physics, Delhi Technological University, Delhi and has fulfilled the requirements for the submission of this thesis. I further declare that it has not formed the basis for the award of any degree, diploma, fellowship or associateship or similar title of any University or Institution. The extent of information derived from the existing literature has been indicated in the body of the thesis at appropriate places giving the references.

Mrityunjay Kumar Singh
Research Scholar
(Reg. No. 2K16/Ph.D./AP/04)

Date: **23/11/2021**
Place: **Delhi**

Delhi Technological University

Formerly Delhi College of Engineering

(Under Delhi Act 6 of 2009, Govt. of NCT of Delhi)

Shahbad Daulatpur, Bawana Road, Delhi-110042

CERTIFICATE

This is to certify that the thesis entitled ***"Investigations of Metal Assisted Titanium Dioxide (TiO_2) Nanocrystals"*** submitted to the Delhi Technological University (DTU), Delhi for the award of degree of "***Doctor of Philosophy***" in Applied Physics is a record of bonafide original research work carried out by ***Mr. Mrityunjay Kumar Singh*** under my supervision at Laser-Spectroscopy Laboratory, Department of Applied Physics, Delhi Technological University, Delhi and has fulfilled the requirements for the submission of this thesis. It is further certified that the work embodied in this thesis has neither been partially nor fully submitted to any other university or institution for the award of any degree or diploma.

Dr. Mohan Singh Mehata
Supervisor
Assistant professor
Department of Applied Physics
Delhi Technological University,
Delhi- 110 042

Submitted Through:

Prof. Rinku Sharma
Head of the Department
Department of Applied Physics
Delhi Technological University,
Delhi-110 042

ACKNOWLEDGEMENTS

The journey of my research is accomplished with the valuable support of many people. It is a pleasant aspect that I have now the opportunity to express my gratitude for all of them.

At the outset, I would like to my profound sense of gratitude, indebtedness and reverence to my supervisor, ***Dr. Mohan Singh Mehata****, Department of Applied Physics, Delhi Technological University, Delhi, who nurtured my research capabilities for a successful scientific career. It has been an honour to work under excellent, enthusiastic and distinguished supervisors. Their unremitting encouragement, constant help, meticulous supervision and constructive criticism throughout the course of my study for carving another milestone in my academic journey. Their immense knowledge of the subject, analytic gaze, farsightedness and perseverance were a constant source of inspiration during the course of this thesis work.*

I feel privileged to have worked under such a great supervision. I further stand ovated to ***Prof. Rinku Sharma****, Head, Department of Applied Physics, DTU, for her valuable help and suggestions. My heartfelt recognitions for* ***Prof. S.C. Sharma****, DRC Chairman, former Head Department of Applied Physics, DTU, my SRC & DRC committee members for their enduring support and appropriate propositions. I express my sincere gratitude especially to* ***Dr. Hem Chandra Joshi*** *(Scientist SG), Institute of Plasma Research, Gandhi Nagar, Gujarat,* ***Prof. B. D. Malhotra****, Department of Biotechnology, DTU, and* ***Dr. Pawan Kumar Tyagi****, Department of Applied Physics, DTU for their timely advice and support as SRC members.*

I express my sincere gratitude to ***Dr. Amrish K. Panwar*** *(Applied Physics, DTU) and* ***Prof. Ram Singh*** *(Applied Chemistry, DTU) for their valuable help, suggestions and availing the lab equipment. It is my pleasure to express my sincere thanks to all the faculty members of Department of Applied Physics, DTU for their continuous encouragement and*

help during my research work. I am also grateful technical and non-technical staff for their timely support and cooperation whenever required.

I express my sincere gratitude to our international research collaborators; ***Chair Prof. Nobuhiro Ohta****, Department of Applied Chemistry, National Yang Ming Chiao Tung University (NYCU), Taiwan for providing their research facilities and stay at NYCU. I would also like to thanks* ***Dr. Kamlesh Awasthi*** *and* ***Mr. Shailesh Rana*** *(National Yang Ming Chiao Tung University (NYCU), Taiwan for providing their help, co-operation and fruitful discussions.*

I sincerely thank my dear former and present lab-mates whose support helped in accomplishing my work. It is my pleasure to thank my seniors ***Dr. Ratneshwar Kr. Ratnesh****,* ***Dr. Vinay Kumar, Dr. Lucky Krishnia, Dr. Rakesh Sahora*** *and present labmates* ***Mr. Prateek Sharma, Mr. Vineet Sharma, Mr. Vijay Singh Meena****,* ***Mr. Deepak Kumar, Mr. Aaryan, Ms. Namrata*** *for their support. I sincerely thank my dear friends especially* ***Mr. Abhishek Bhardwaj, Mr. Mukesh Kr. Sahu, Mr. Gaurav Kumar, Mr. Hemendra Nath Jaiswal, Dr. Ripu Daman Dixit*** *for their support helped in accomplishing my work. I would also like to thank all the other research scholars of Department of Applied Physics, Delhi Technological University, Delhi for their help and advice. I wish to acknowledge the enjoyable company and suitable help rendered by my dear friends,* ***Mr. Rajat Bajaj, Mr. Lakhan Kumar, Mr. Uday Veer Singh, Ms. Suman Dahiya, Mr. Yashaswi Nandan, Mr. Ujjwal, Mr. Sharad, Mr. Indrajeet, Mr. Vikas, Mr. Shailendra Singh, Mr. Abhishek Kumar Sharma*** *for their help and support during this tenure.*

Finally, I thank my family for their support and motivation, every moment of my research period. With heartful gratitude and love, I express my gratefulness to my father ***Mr. Basant Kumar Singh****, mother* ***Mrs. Radhika Devi*** *for their continual love and encouragement over the entire course of my life. I am thankful to my brother* ***Mr. Sanjay***

Kumar Singh *and sister* ***Ms. Priyanka Singh*** *for the valuable suggestions, care, love and having faith in me throughout my existence. I am thankful to my extended maternal and paternal family for helping me maintain a positive attitude throughout my studies. I always thankful to all my beloved friends across the globe for sharing my happiness and sorrow.*

I gratefully acknowledge the financial assistance provided by ***Delhi Technological University*** *in the form of Junior Research Fellowship and Senior Research Fellowship during the period of my research. I extend my gratitude to Delhi Technological University and staff in Administration, Accounts, Store & Purchase, Library and Computer Centre for their help and services.*

I thank one and all for helping me accomplish the successful realization of the thesis.

Thank you all!!!

Mrityunjay Kumar Singh

LIST OF PUBLICATIONS

Included in the thesis

1. **M. K. Singh** and M. S. Mehata, Phase-dependent optical and photocatalytic performance of synthesized titanium dioxide (TiO_2) nanoparticles***, Optik 193 (2019) 163011.***
2. **M. K. Singh** and M. S. Mehata, Enhanced photoinduced catalytic activity of transition metal ions incorporated TiO_2 nanoparticles for degradation of organic dye: Absorption and photoluminescence spectroscopy, ***Optical Materials* 109 (2020) 110309.**
3. **M. K. Singh** and M. S. Mehata, Temperature-dependent Photoluminescence (PL) and Time-resolved PL of different phases of TiO_2 Nanoparticles: Carrier dynamics and Trap states, ***Ceramics International 47 (2021) 32534–32544.***
4. M. S. Mehata, **M. K. Singh**, K. Awasthi, P. Sharma, S. Rana, N. Ohta, Temperature-Dependent Electric Field Induced Optical Transitions of 2D-Molybdenum Disulfide (MoS_2) Thin Films: Temperature-Dependent Electroabsorption and Absorption, ***The Journal of Physical Chemistry: C 2021 (Manuscript Accepted).***

Other than thesis work

5. P. Sharma, **M. K. Singh** and M. S. Mehata, Sunlight-driven MoS_2 nanosheets mediated degradation of dye (crystal violet) for the wastewater treatment, ***Journal of Molecular Structure 1249 (2022) 131651.***
6. D. Kumar, **M. K. Singh** and M.S. Mehata, Structural analysis of produced cobalt-doped zinc oxide nanoparticles and photodegradation of industrial dye ***(Communicated).***

Publications in conference/workshop proceeding

1. **M. K. Singh**, R.K. Ratnesh and M. S. Mehata, "Synthesis and Characterization of Titanium dioxide (TiO_2) via low temperature synthesis method" presented at "DAE-BRNS National Laser Symposium (NLS-26)" held on 20-23, December, 2017, at BARC, Mumbai.
2. **M. K. Singh** and M. S. Mehata, "Annealing effect on synthesized titanium dioxide (TiO_2) nanoparticles" presented at "International Conference on Recent Advances in Interdisciplinary Sciences" held on 11-12 January 2019, Jammu.
3. **M. K. Singh** and M. S. Mehata, "Dependency of photocatalytic performance on different phases of TiO_2 nanoparticles" presented at "International Conference on Sustainable Technologies for Environmental Management (STEM-2019)" held on 25-26, March, 2019, DTU, Delhi.
4. **M. K. Singh** and M. S. Mehata, "Photocatalytic degradation of Rhodamine B dye by synthesized TiO_2 nanoparticles" presented at "Trombay Symposium on Radiation & Photochemistry" held on 05-09 January 2020 at BARC, Mumbai.

CONTENTS

LIST OF FIGURES

LIST OF TABLES

Chapter-1

Introduction

1.1 Nanoscience and Nanotechnology

One of the leading branches of science is 'Nanoscience', which deals with the advantageous properties of the materials with the size ranges in the nanoscale region. On the other hand, nanotechnology is the branch of engineering that deals with manipulating the size-related properties of the materials in the nanoscale region. It includes the synthesis, characterization, exploration, and utilization of nanomaterials. Synthesis of the nanomaterials deals with the size reduction and the controlled management of the atoms, molecules, morphology, defects, and relationship between surface & volume. The involvement of nanotechnology revolutionized many aspects of industries, as it provides many new solutions to the existing problems on the industrial front. The multidisciplinary approach of nanotechnology leads many aspiring researchers to devote their time to further improving nanotechnology. Large industrialized countries such as the USA, China, Russia spend a considerable amount of money, more than US$ 10 billion annually, on this area of material features study [1]. This results in a favorable impact on employment and the economy.

Nanotechnology is a diverse field associated with many scientific fields such as materials sciences, organic chemistry, surface science, molecular biology, microfabrication, medical science, semiconductor physics, etc. [2]. These fields associated research and application are equally divergent, ranging from expansion of conventional device physics to the new Nano-technological approach to entirely new molecular self-assembly, from a new material with nanoscale dimension development to direct control of the matter at the atomic scale.

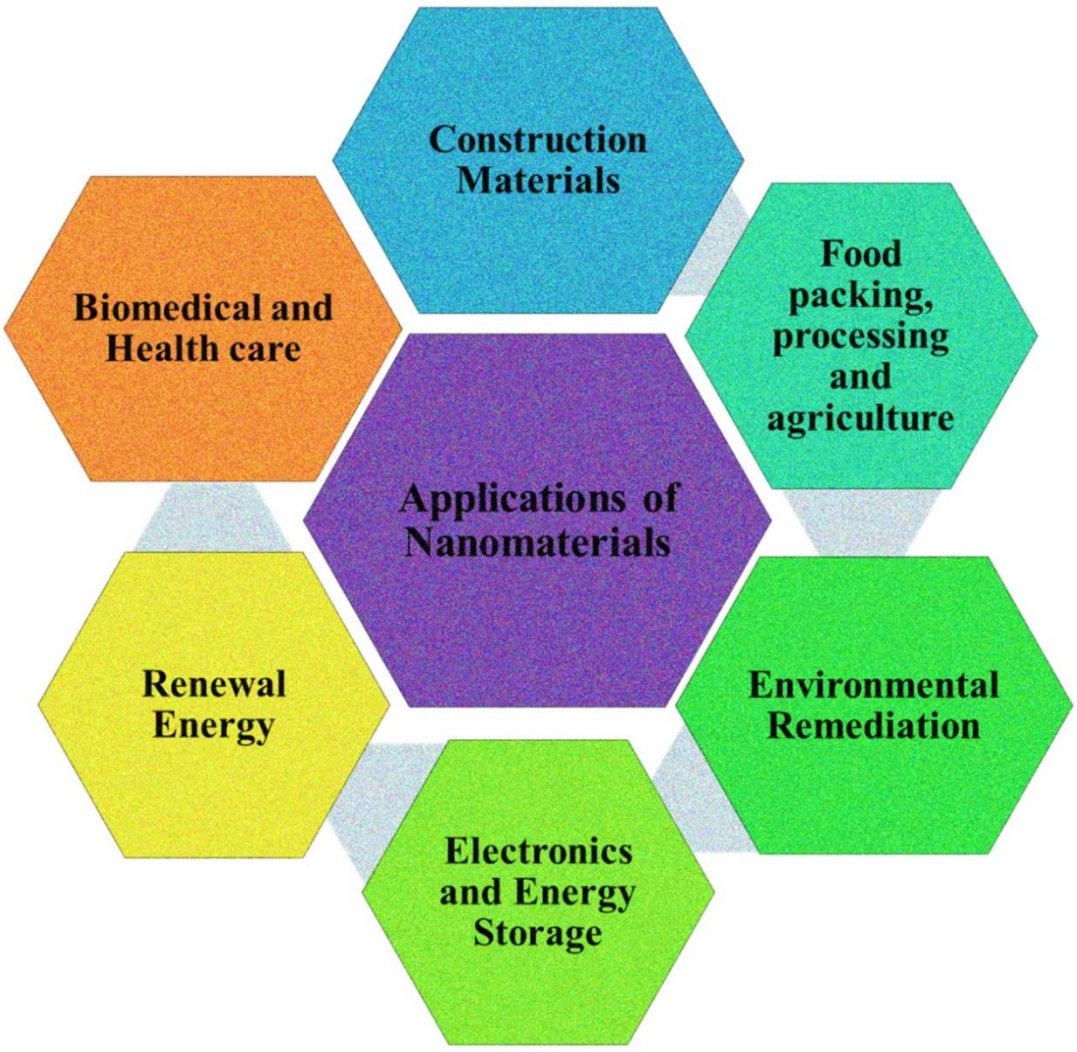

Figure 1.1 Schematic demonstration of the numerous applications of nanotechnology.

Many new nanomaterials are being developed, including fibers, polymers, ceramics and glass, which are present in the market with desired form and definite shape and became necessary in everyday life chores, i.e., from washing machines to architecture. Figure 1.1 represents the various application of nanotechnology. In 1959, the Nobel prize winner for Physics (1965), Richard P. Feynman, presented the conception of nano and aforesaid "there is plenty of room in the bottom" during the conference of American Physical Society. In this lecture, Feynman made the hypothesis, “Why can’t we write the entire 24 volumes of the Encyclopedia Britannica on the head of a pin?”, and described a vision of employing machines to construct smaller machines and down to the molecular level.

1.2 Nanomaterials

The principal characteristics of nanomaterials are their shape, size, and morphological sub-structure of the material. Materials with dimensions typically in the range from 1 to 100 nm are considered among nanomaterials [3]. The diameter of the human hair is 100,000 times bigger than a nanometer. To date, researchers have successfully synthesized various nanomaterials for numerous applications, which were helpful in the fulfillment of various day-to-day life activities [4–7]. Compared to the macroscale or microscale materials, the nanoscale materials exhibit different optical, electrical, physical and mechanical properties. This is mainly owing to (i) the availability of a large aspect ratio of nanomaterials, (ii) quantum confinement and change in conductivity and (iii) high surface energy [8,9]. The large definite nanomaterials surface area intensifies recognition sensitivity and helps in the miniaturization of the emerging devices [10]. Accordingly, the preparation of nanomaterials, separation and pre-concentration procedures play essential roles in many systematic actions, such as increasing analyte concentration and removing interfering species [11].

Among the various nanomaterial applications, one prime and practical utility are to degrade the waste and toxic materials to the eco-friendly and useful residue. Also, reducing the cost of degradation of industrial waste and toxic materials by using nanomaterials is another topic of interest. Nanomaterials catalyze the degradation of toxic and waste materials, which are unsafe to the environment and microorganisms [12]. Due to NPs significant potential among various sectors of the technology, it is expected to increase the utility of NPs and play a major role in the sustainable improvement of society.

1.3 Classification of nanomaterials

Nanomaterials are categorized into (i) dimension-wise and (ii) based on constituents, morphology, chemical composition, etc. The classification of nanomaterials [13] is shown

in figure 1.2.

1.3.1 Zero-Dimensional (0 D) nanomaterial

All three dimensions of 0-D nanomaterials are in the nanoscale range [14]. 0-D includes cubical nanomaterials, spherical, polygon, nanorods, hollow spheres, core-shell nanomaterials, and quantum dots (QDs). The most popular 0-D materials are nanoparticles and QDs. In 0-D, electrons have 3-D confinement. All three dimensions are around the Bohr exciton radius. Since we know that only atom nature is 3-D confinement, it is also called artificial atoms [3,14].

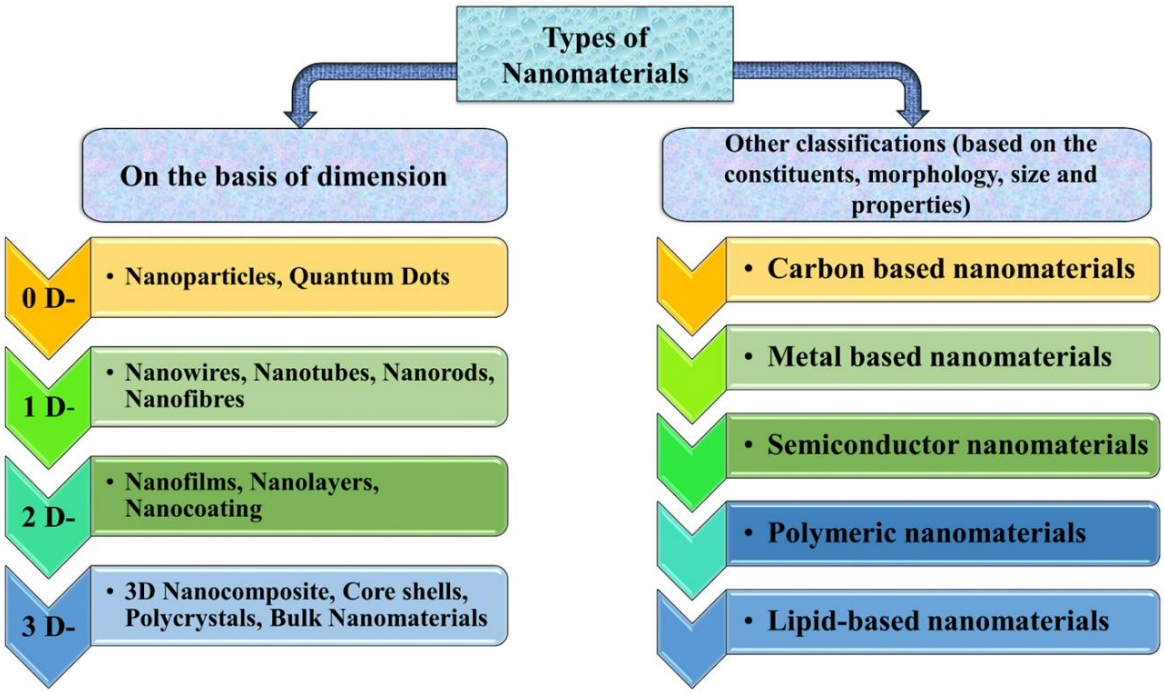

Figure 1.2 Schematic representation of different criteria wise the classification of nanomaterials.

1.3.2 One -Dimensional (1 D) nanomaterial

It is a structure where any one of the dimensions is larger than the nanoscale, and the other two dimensions are in the nano range (<100 nm). The example of the 1-D structure are nanorods, nanotube, quantum wire, nanowire. Transport characteristics of electrically conducting nanowires were affected by the quantum effect. Confinement of the conduction

electrons are in the transverse direction of the wire, and quantization of energy takes place into a series of distinct values [3,14].

1.3.3 Two -Dimensional (2 D) nanomaterial

In this class of nanomaterials, only one directional confinement is present, resulting in the formation of a quantum plane/well. Quantum well's length and breadth have been large compared to height, around the dimension of Bohr exciton radius. Nanodiscs, nanolayers, etc., are examples of this class of materials [3,14].

1.3.4 Three-Dimensional (3 D) nanomaterial

This class of materials has not confined all three dimensions in the nanoscale range [14]. Examples of 3D materials are bulk powders, bundles of nanowires, nanotubes, and multi-nanolayers [3,14].

1.3.5 Carbon-based nanomaterials

The carbon-based nanomaterials can be graphene, fullerenes, carbon nanofibers, and hollow tubes or spheres [15]. These types of nanomaterials have rich carbon content and various morphologies. The synthesis processes used to produce carbon-based nanomaterials include chemical vapor deposition (CVD), arc discharge, chemical routes and laser ablation.

1.3.6 Metal-based nanomaterials

These kinds of nanomaterials are prepared by the decomposition of metals and metal oxides [16]. Examples of metallic nanomaterials are Fe, Au, and Ag, etc., and the metal oxides are Al_2O_3, ZnO, MnO_2, and TiO_2 [17].

1.3.7 Semiconductor based nanomaterials

These categories of nanomaterials have a low bandgap energy (< 4 eV). The semiconductor materials are composed of different compounds from various periodic tables like III-V, II-VI and IV. Examples of semiconductor materials are germanium, silicon, ZnO, TiO_2,

GaAs, etc. Structural modification into the nanoscale range of semiconductors can change the material's physical and chemical properties [17]. This effect corresponds to the upsurge in the surface area or quantum size effect.

1.3.8 Polymeric nanomaterials

Polymeric nanomaterials are nanosized solid particles along with synthetic or natural polymers. Such materials are used in various applications like medical applications as drug release controllers and other pharmaceutical applications [18].

1.3.9 Lipid-based nanomaterials

These nanomaterials have nanostructured lipid carriers, solid lipid nanoparticles (NPs) and liposomes [19]. These materials are used in drug delivery as they are capable of transporting hydrophobic and hydrophilic molecules. These have low toxicity and are capable of controlled drug release in human body targets.

1.4 Why are nanomaterials important?

Nanomaterials have been getting much attention in current years due to their enhanced optical, magnetic, electrical, and mechanical properties. Several examples with applications of the nanomaterials are as follows:

(i) The ductile nature of the ceramics increases at the raised temperature as the particle size approaches the nanophase from the coarse-grained ceramics.

(ii) The quantum confinement effect, which leads to luminescence properties in the nanomaterials is shown by the semiconductor Q-particles.

(iii) Nanosized metallic powders are used to produce dense parts, porous coating, and gas-tight materials.

(iv) Semiconducting nanomaterials have a significant impact in the field of catalysis.

(v) Metal oxide nanomaterials (TiO_2, SiO_2, MnO_2, and ZnO) are used in the gas sensor (CO, CH_4, NO_x, CO_2, NH_3) with enhanced selectivity and sensitivity, batteries, solar cells, etc.

(vi) Polymer-based composites with a high dielectric constant and a high concentration of inorganic particles are promising materials for photonic bandgap structures.

1.5 Synthesis of nanomaterials

There are mainly two methods used to prepare the nanomaterials, top-down and bottom-up. In top-down approaches, the macroscopic bulk material is broken down into the preferred size of the NPs by diverse methods. The examples of top-down are etching, grinding/milling, e-beam lithography, ball milling and physical vapor deposition (PVD) [16].

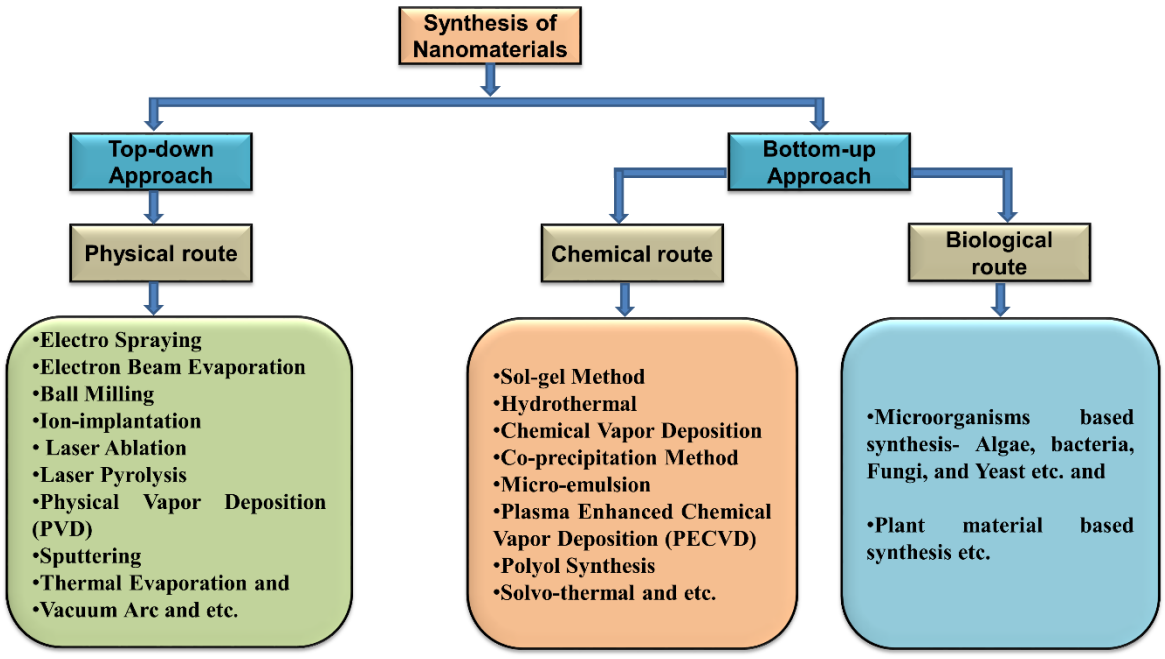

Figure 1.3 The nanomaterials synthesis routes via top-down and bottom-up approaches.

In the bottom-up technique, the materials are brought at the atomic level, held together with covalent forces and switched into the required NPs. Integration follows the production of NPs from colloidal dispersion and powder generation from sol-gel techniques. The instance of bottom-up is hydrothermal method, chemical vapor deposition (CVD), green synthesis,

electrospinning, atomic layer deposition, etc. The synthesis approaches from the different methods are shown in figure 1.3.

1.6 Introduction to titanium dioxide (TiO_2)

In recent years, nanoparticles application has covered different fields, including catalysis, medicine, sensor, and optoelectronics. Elemental composition, size, and structure are the chief parameters besides the quantum size effect in nanometer-scale materials for the favorable application in different technological sectors. Among the oxide-based metallic nanostructure, TiO_2 has been used widely in various fields, including catalysis, gas sensing, batteries, white pigments for paints, solar cells, organic pollutant degradation, cosmetics, and many more. The applications of TiO_2 depend on the morphology, particles size and crystalline structure [20,21].

Titanium dioxide (TiO_2), also well-known as titania semiconducting material, is deliberated the most promising catalyst among various semiconductors with many advantages, comprising the stability for the considerable duration, non-toxic and inexpensive, and entirely used to treat contaminated water [21,22]. TiO_2 occurs in three diverse crystalline structures, namely anatase, brookite, and rutile phases. Among these phases, the rutile phase has more thermodynamically stable as compared with anatase and brookite phases. Due to these crystalline phases and the physical properties of titania, for instance, dielectric constant, refractive index, chemical and photochemical reactivity differ from each other [21]. Among all crystalline phases, the anatase phase is favored for photocatalytic and solar cell application because of the larger bandgap (E_g = 3.2 eV compared to 3.0 eV for rutile). Titania is a potential candidate for generating photonic bandgap materials and other photonic applications due to its absorption in the UV-visible region and comparatively possesses a high valued refractive index (n) 2.4 for anatase and 2.9 for the rutile phase [23].

1.7 Structure of titanium dioxide

TiO_2 is one of the major kinds of transition metal oxides. Figure 1.4 illustrates the crystal structure of TiO_2 NPs, which have three distinct phases, specifically anatase, rutile and brookite phases [21]. In all three polymorphous phases, anatase and rutile phases have tetragonal structures, while brookite has orthorhombic structures. In the crystal structure of these phases, each titanium ion (Ti^{4+}) is surrounded by six oxygen (O^{2-}) atoms, while three titanium atoms encapsulate one oxygen atom. In the rutile phase, irregular octahedrons of six oxygen atoms with a slight orthorhombic distortion.

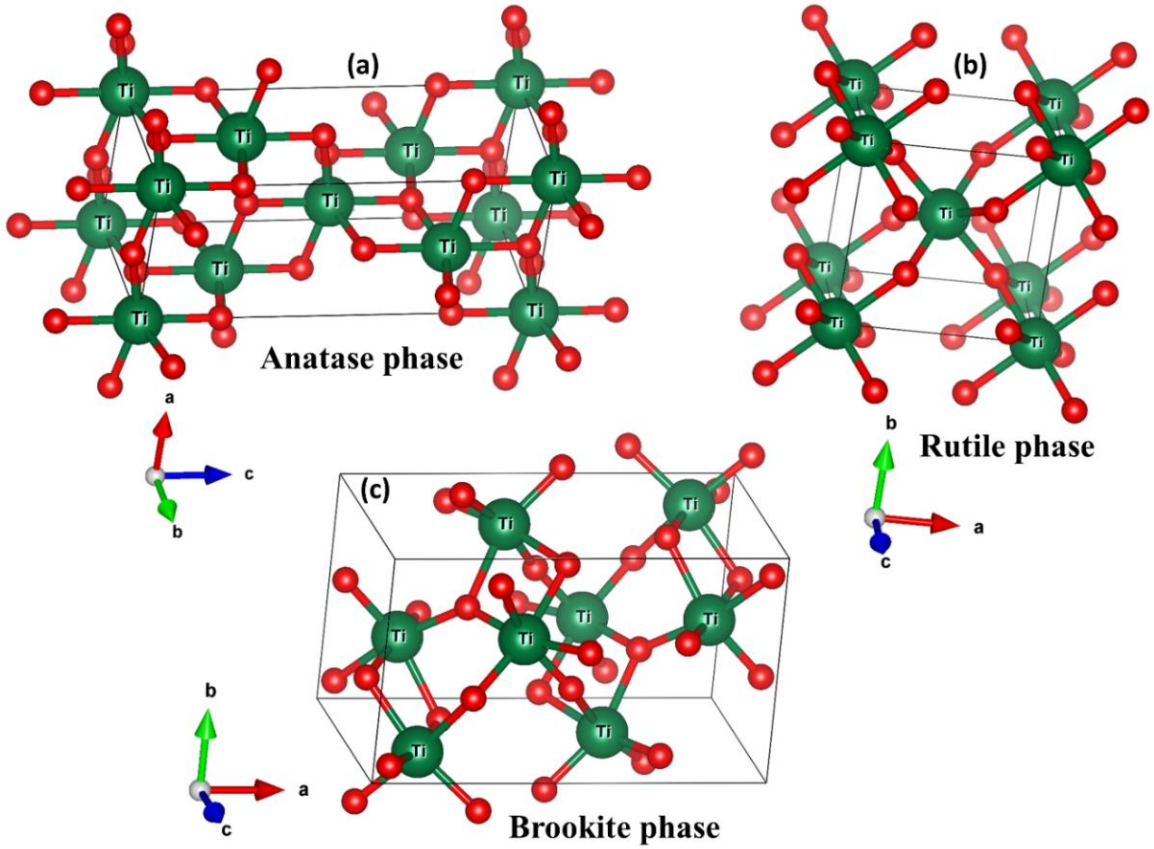

Figure 1.4 Unit cell crystal structure of anatase (a), rutile (b), and brookite phase (c) of TiO_2 NPs.

The significant distortion can be observed in the octahedron of six oxygen atoms in the anatase phase, resulting in a lower symmetry than orthorhombic. Anatase and rutile crystal structures can be demonstrated as the chains of TiO_6 octahedral with common edges.

Each octahedron in the rutile phase remains in contact with ten neighboring octahedrons (two sharing edge oxygen pairs and eight sharing corner oxygen atoms) [24]. In the anatase structure, each octahedron is in contact with 8 neighbors (four sharing an edge and four sharing a corner), while in the brookite structure, both edges and corners are shared to give an orthorhombic form [24]. Among the three major phases of titania, the anatase phase is primarily applied in numerous applications, which holds a key factor for various industrial purposes. The rutile phases are used in fundamental studies [25]. Anatase type of TiO_2 NPs found to be most photoactive and used in environmental applications such as wastewater treatment, air purification, etc. [26]. This occurs due to the lower level of the conduction band is located towards more negative than the rutile, producing photogenerated electrons with higher reduction potential. Whereas, in nanoscale TiO_2, there is an increase in the optical bandgap with slightly shifting the conduction band levels towards higher reduction potentials with the formation of more active, longer-life time radicals for photocatalytic applications. The crystal structure and physical characteristics of anatase, brookite, and rutile phase are represented in Table 1.1.

Table 1.1 Physical and structural properties of different phases of TiO_2 nanomaterials.

Properties	Anatase	Brookite	Rutile
Crystal structure	Tetragonal	Orthorhombic	Tetragonal
Lattice constant (Å)	a=3.784 b=3.784 c=9.515	a=9.184 b=5.447 c=5.154	a=4.5936 b=4.5936 c=2.9587
Space group	I41/amd	Pbca	P42/mnm
Density (g cm^{-3})	3.79	4.13	4.23
Molecule (cell)	2	4	2

Volume/molecule (Å^3)	34.061	32.172	31.216
O-Ti-O bond angle	77.7° 92.6°	77.0°–105°	81.2° 90.0°
Ti-O bond length (Å)	1.937 (4) 1.965 (2)	1.87-2.04	1.949 (4) 1.980 (2)

1.8 Synthesis of TiO_2 nanostructure

Titania was first commercially manufactured in the year 1923. This has been extracted from multiple ores. For TiO_2 NPs, several synthesis routes were proposed in the published articles, including hydrothermal method, microwave-assisted hydrothermal process, flame synthesis, sol-gel technique with alkoxide as precursors, ultrasonic irradiation, chemical vapor deposition (CVD), sputtering and thermal plasma [27–35]. Among these techniques, the most favored technique is the sol-gel technique due to its ability of mass production of NPs with improved crystallinity and greater aspect ratio [36].

1.8.1 Temperature effect on TiO_2 NPs

Heat treatment during the synthesis of the nanoparticles plays a vital role and affects the crystallinity, morphology, porosity, surface area, and causes the phase transformation [37]. Organic materials eradicate at high temperatures (400 °C and above). The surface area of NPs also diminutions with heating rates and calcination time. Resulting pores in the TiO_2 powder collapsing, which affected the phase transformation, i.e., from amorphous to crystalline anatase phase. TiO_2 usually undergoes anatase to rutile phase transformation at 550 to 700 °C temperature range. The phase transformation was also affected by the synthesis condition, impurities, precursors, primary particle size of anatase, and oxygen vacancies [37]. Both anatase and rutile phases have possessed nanosized dimension tend to exhibit properties it may be significantly different from the bulk TiO_2 materials.

1.9 Limitation and modification

Though titania is a very good photocatalyst, it has some restrictions. Due to its wide bandgap energy, it is only active under UV light illumination and has a higher recombination rate for the photogenerated electron-hole pairs [38]. The photocatalytic of titania critically depends on the oxygen defect in the surface region of the crystal substrate. Hence, doping and surface modification with different metal ions are vital for improving the catalytic activities of TiO_2 [39,40]. The TiO_2 has a highly crystalline structure, so these metal ions are either doped into the crystal lattice or intercalated in the TiO_2 or mononuclear complexes [41,42]. These modifications were made to reduce the bandgap energy or form the energy levels in the forbidden energy gap and decrease the rate of electron-hole pair recombination by trapping. The bandgap of 3.2 eV of the anatase phase [22,38] of TiO_2 lies in the near UV (ultraviolet) ranges of the electromagnetic spectrum. Hence, the results conclude that only UV light can create an electron-hole (e-h) pair in TiO_2. UV radiation accounts for only a tiny portion of the solar spectrum (3-5 %). Researchers have focused their attention on shifting the optical response of the TiO_2 towards the visible region. Numerous studies have given a potential solution to this problem by incorporating adequate transition metal ions [43–45]. Doping a smaller concentration of metal ions decreases the recombination rate of electron-hole pair and essentially reduces TiO_2 bandgap simultaneously; hence red shifted the absorption spectrum. However, the higher doping concentration of transition metal ions modified the nanoscale's redox potential results and morphologies. There are notable variations in the crystalline phase, the oxidation states of the host lattice, and dopant ions [46].

Table 1.2 Short review of literatures

Year	Synthesis techniques	Raw Materials (Precursors)	Particle size (nm)	References
1999	Sol-gel	Titanium isopropoxide, Ethanol, Di-water, HCl	58 nm	[47]
2000	Chemical vapor deposition (CVD)	Titanium (IV) chloride, Silica gel, Di-water, Nitrogen gas, Quartz disk, Ethanol	25-30 nm	[48]
2001	Sol-gel	Titanium (IV) butoxide, Ethanol Acetic acid, Tetrachloroauric Acid, Di-water	18.4-19.4	[49]
2002	Hydrothermal Process	TritonX-100,1hexanol, cyclohexane, Titanium (IV) butoxide, HNO_3 (conc.), HCl (conc.), and phenol	-	[50]
2003	Low-temperature	titanium tetrachloride, 1-butyl-3-Methyl-imidazolium-tetrafluoroborate, , Di-water	6.3 nm	[51]
2004	Solution Combustion Method	Hexamethylenetetramine, Titanyl nitrate, Nitric acid, Glycine, oxalyldihydrazide	6-18 nm	[52]
2005	Hydrothermal Method	Titanium disulfate, Ethanol, Cetyltri-methyl-ammonium bromide (CTAB), Di-water	2.1-2.8	[53]

2006	Thermal plasma oxidizing mists	Titanium tetra-n-butoxide, europium (III) nitrate, Di-ethanolamine, , citric acid, plasma sheath (10-90 L/min)	30-36 (anatase) 64-83 (rutile)	[54]
2007	Sol -gel	Titanium isopropoxide, citric acid, nitride acid, ammonia, ethanol, ethylene glycol, Di-water	13.8-19 nm	[55]
2008	Hydrothermal Process	Titanium tetraisopropoxide, Silver nitrate, Hydrazine, Cetyltri-methyl-ammonium bromide (CTAB), Ethanol, ferric nitrate, Di-water	15 nm	[56]
2009	Sol-gel	Titanyl sulphate, Nitric acid, sulphuric acid, urea, Ammonia, glucose, silver nitrate	40-44 nm	[57]
2010	Solvothermal	Titanium (IV) chloride, Tetrahydrofuran (THF), benzyl alcohol, Niobium(V) ethoxide, tert-Butyl alcohol, Pluronicm F127	4-15 nm	[58]
2011	Sol-gel	Tetrabutyl titanate, Manganese nitrate, Nitric acid, Ethanol, Acetic acid, Di-water	6.8-7.4 nm	[59]

2012	Sol-gel	Titanium tetra-isopropoxide, Manganese sulfate, Citric acid, Polyethylene glycol, Di-water	6-8 (anatase) 15-18 (rutile)	[60]
2013	Sol-gel	Titanium (IV) isopropoxide, Zirconium (IV) oxynitrate, Ethylene glycol, Glacial acetic acid, Di-water	11.4 nm	[61]
2014	Chemical vapor deposition (CVD)	Ammonium hexafluoro titanate, Hydrofluotitanic acid, Soda-lime glass, Nitric acid, Boric acid, Di-water	-	[62]
2015	Sol-gel	Titanium tetra isopropoxide, Cobalt Nitrate, Ethanol, 2-propanol, Di-water	15-25 nm	[63]
2016	Hydrothermal Process	Ti foil, Alcohol, Acetone, Hydrochloric acid, Di-water	40 nm	[64]
2017	Microwave-Assisted Hydrothermal	Titanium Tetraisopropoxide, Nitric acid, Ethanol, Sodium hydroxide, Di-water,	10-15 nm	[65]
2018	Co-precipitation	Titanium isopropoxide, Di-water, methanol	10-52 nm	[66]
2019	Co-precipitation	Titanium (IV) oxysulphate, Sodium hydroxide, Di-water	5-10 nm	[67]
2020	Hydrothermal method	Titanium sulfate, DI water, silver nitrate, Ethanol	18-20 nm	[68]

2021	Sol-gel	Titanium isopropoxide, Silver nitrate, Thiourea, Acetic acid glacial, Acetone, Barium acetate, Chromium acetate	6-8 nm	[69]
2021	Sol-gel	Titanium tetra isopropoxide, acetic acid, isopropanol, demineralized water	18-28 nm	[70]

1.10 Statement of problems and objectives

In the global scenario, TiO_2 and foreign elements doped TiO_2 are one of the current interests due to their wide application in various fields. Among the significant number of research articles discussing the preparation and application of TiO_2 NPs with different routes, sol-gel was the most convenient synthesis route opted by the researchers. TiO_2 has attracted tremendous attention owing to its high photocatalytic and non-toxicity activity, functionality with high thermal stability. The photocatalytic degradation of pollutants using undoped and doped TiO_2 NPs is very attractive for environmental protection applications as a possible solution for water purification. To prove suitable candidates for the photocatalytic application, the catalytic performance of undoped and metal-doped titania by the degradation of organic dyes has been carried out.

In the current thesis, doped and undoped TiO_2 NPs were prepared using the sol-gel method. These TiO_2 NPs were explored by measuring X-ray diffraction patterns, absorption spectra, photoluminescence spectra and time-resolved photoluminescence decays at room and low temperatures. The crystalline structures were identified. Distinct optical properties were obtained at low temperatures for different phases of TiO_2 NPs. These NPs were used as photocatalysts for the degradation of dyes under UV irradiation. Based on the extensive

characterization and measured properties, the outcome of the research work has been organized into seven chapters, including the absorption and electroabsorption spectra of MoS_2 nanosheets at low temperatures.

References

[1] A. Nouailhat, An introduction to nanoscience and nanotechnology. Vol. 10. John Wiley & Sons, 2010.

[2] R. Saini, S. Saini, S. Sharma, Nanotechnology: The future medicine, J. Cutan. Aesthet. Surg. 3 (2010) 32.

[3] V. V. Pokropivny, V. V. Skorokhod, Classification of nanostructures by dimensionality and concept of surface forms engineering in nanomaterial science, Mater. Sci. Eng. C. 27 (2007) 990–993.

[4] R.K. Sahu, R.K. Ojha Nano-material's and its potential applications in the field of renewable energy, Int. J. Eng. Technol. 3 (2015) 1–4.

[5] L. Kumar, V. Ragunathan, M. Chugh, N. Bharadvaja, Nanomaterials for remediation of contaminants: a review, Environ. Chem. Lett. 19 (2021) 3139–3163.

[6] A. Bratovcic, Different applications of nanomaterials and their impact on the environment, Int. J. Mater. Sci. Eng. 5 (2019) 1–7.

[7] I. Khan, K. Saeed, I. Khan, Nanoparticles: Properties, applications and toxicities, Arab. J. Chem. 12 (2019) 908–931.

[8] M.A. Gatoo, S. Naseem, M.Y. Arfat, A. Mahmood Dar, K. Qasim, S. Zubair, Physicochemical properties of nanomaterials: Implication in associated toxic manifestations, Biomed Res. Int. 2014 (2014) 1-8.

[9] A.B. Asha, R. Narain, Nanomaterials properties, Elsevier Inc., (2020) 343-359.

[10] N.M. Noah, design and synthesis of nanostructured materials for sensor applications, J. Nanomater. 2020 (2020) 1-20.

[11] A.O. Mulec, A. Mladenovič, A.M. Pranjić, P. Oprčkal, J. Ščančar, R. Milačič, Study of interferences and procedures for their removal in the spectrophotometric determination of ammonium and selected anions in coloured wastewater samples,

Anal. Methods. 12 (2020) 4769–4782.

[12] M. Rizwan, M.U. Ahmed, Nanobioremediation: Ecofriendly application of nanomaterials, Handb. Ecomater. 5 (2019) 3523–3535.

[13] H. Gleiter, Nanostructured materials: basic concepts and microstructure, Acta Mater. 48 (2000) 1–29.

[14] V. V. Pokropivny, V. V. Skorokhod, H. Gleiter, J.N. Tiwari, R.N. Tiwari, K.S. Kim, Zero-dimensional, one-dimensional, two-dimensional and three-dimensional nanostructured materials for advanced electrochemical energy devices, Prog. Mater. Sci. 48 (2012) 724–803.

[15] Z. Li, L. Wang, Y. Li, Y. Feng, W. Feng, Carbon-based functional nanomaterials: Preparation, properties and applications, Compos. Sci. Technol. 179 (2019) 10–40.

[16] T.A. Saleh, Nanomaterials: Classification, properties, and environmental toxicities, Environ. Technol. Innov. 20 (2020) 101067.

[17] T.A. Saleh, G. Fadillah, Recent trends in the design of chemical sensors based on graphene–metal oxide nanocomposites for the analysis of toxic species and biomolecules, TrAC - Trends Anal. Chem. 120 (2019) 115660.

[18] X. Yang, K. Lian, Y. Tan, Y. Zhu, X. Liu, Y. Zeng, T. Yu, T. Meng, H. Yuan, F. Hu, Selective uptake of chitosan polymeric micelles by circulating monocytes for enhanced tumor targeting, Carbohydr. Polym. 229 (2020) 115435.

[19] Q. Zhong, L. Zhang, Nanoparticles fabricated from bulk solid lipids: Preparation, properties, and potential food applications, Adv. Colloid Interface Sci. 273 (2019) 102033.

[20] H. Hao, J. Zhang, The study of Iron (III) and nitrogen co-doped mesoporous TiO_2 photocatalysts: synthesis, characterization and activity, Microporous Mesoporous Mater. 121 (2009) 52–57.

[21] M.K. Singh, M.S. Mehata, Phase-dependent optical and photocatalytic performance of synthesized titanium dioxide (TiO_2) nanoparticles, Optik 193 (2019) 163011.

[22] M.K. Singh, M.S. Mehata, Enhanced photoinduced catalytic activity of transition metal ions incorporated TiO_2 nanoparticles for degradation of organic dye: Absorption and photoluminescence spectroscopy, Opt. Mater.109 (2020) 110309.

[23] M. Pal, J. García Serrano, P. Santiago, U. Pal, Size-Controlled Synthesis of Spherical TiO_2 Nanoparticles: Morphology, Crystallization, and Phase Transition, J. Phys. Chem. C. 111 (2007) 96–102.

[24] A.L. Linsebigler, G. Lu, J.T. Yates, Photocatalysis on TiO_2 Surfaces: Principles, Mechanisms, and Selected Results, 95 (1995) 735–758.

[25] W.Q. Fang, X.Q. Gong, H.G. Yang, On the unusual properties of anatase TiO_2 exposed by highly reactive facets, J. Phys. Chem. Lett. 2 (2011) 725–734.

[26] M.R. Hoffmann, S.T. Martin, W. Choi, D.W. Bahnemann, Environmental Applications of Semiconductor Photocatalysis, Chem. Rev. 95 (1995) 69–96.

[27] S. Sakthivel, H. Kisch, Daylight photocatalysis by carbon-modified titanium dioxide, Angew. Chem. Int. Ed. 42 (2003) 4908–4911.

[28] T. H. Wang, Z. Fang, N. W. Gist, S. Li, D. A. Dixon, J. L. Gole, Computational Study of the Hydrolysis Reactions of the Ground and First Excited Triplet States of Small TiO_2 Nanoclusters, J. Phys. Chem. C. 115 (2011) 9344–9360.

[29] X. Chen, C. Burda, Photoelectron spectroscopic investigation of nitrogen-doped titania nanoparticles, J. Phys. Chem. B. 108 (2004) 15446–15449.

[30] B. H. K. Kammler, L. Madler, S. E. Pratsinis, Flame Synthesis of Nanoparticles, Chem. Eng. Technol. 24 (2001) 583–596.

[31] J. Shi, X. Wang, Growth of Rutile Titanium Dioxide Nanowires by Pulsed Chemical Vapor Deposition, Cryst. Growth Des. 11 (2011) 949–954

[32] S. Sugapriya, R. Sriram, S. Lakshmi, Effect of annealing on TiO_2 nanoparticles, Optik 124 (2013) 4971–4975.

[33] M. Arin, P. Lommens, S. C. Hopkins, G. Pollefeyt, Deposition of photocatalytically active TiO_2 films by inkjet printing of TiO_2 nanoparticle suspensions obtained from microwave-assisted hydrothermal synthesis, Nanotechnology 23 (2012) 165603.

[34] S. Vyas, R. Tiwary, K. Shubham, P. Chakrabarti, Study the target effect on the structural, surface and optical properties of TiO_2 thin film fabricated by RF sputtering method, Superlattices Microstruct. 80 (2015) 215–221.

[35] Y. Tanaka, T. Tsuke, W. Guo, Y. Uesugi, T. Ishijima, S. Watanabey, K. Nakamura, A large amount synthesis of nanopowder using modulated induction thermal plasmas synchronized with intermittent feeding of raw materials, J. Phys: Conf. Ser. 406 (2012) 012001

[36] N. Baig, I. Kammakakam, W. Falath, I. Kammakakam, Nanomaterials: A review of synthesis methods, properties, recent progress, and challenges, Mater. Adv. 2 (2021) 1821–1871.

[37] S.M. Gupta, M. Tripathi, A review of TiO_2 nanoparticles, Chinese Sci. Bull. 56 (2011) 1639–1657.

[38] J. Wang, W. Sun, Z. Zhang, Z. Jiang, X. Wang, R. Xu, R. Li, X. Zhang, Preparation of Fe-doped mixed crystal TiO_2 catalyst and investigation of its sonocatalytic activity during degradation of azo fuchsine under ultrasonic irradiation, J. Colloid Interface Sci. 320 (2008) 202–209.

[39] S. Liao, H. Donggen, D. Yu, Y. Su, G. Yuan, Preparation and characterization of ZnO/TiO_2, $SO_4^{2-}/ZnO/TiO_2$ photocatalyst and their photocatalysis, J. Photochem. Photobiol. A Chem. 168 (2004) 7–13.

[40] C. Chen, Z. Wang, S. Ruan, B. Zou, M. Zhao, F. Wu, Photocatalytic degradation of

C.I. Acid Orange 52 in the presence of Zn-doped TiO_2 prepared by a stearic acid gel method, Dye. Pigment. 77 (2008) 204–209.

[41] T. Tong, J. Zhang, B. Tian, F. Chen, D. He, Preparation of $Fe3^+$-doped TiO_2 catalysts by controlled hydrolysis of titanium alkoxide and study on their photocatalytic activity for methyl orange degradation, J. Hazard. Mater. 155 (2008) 572–579.

[42] L. Deng, S. Wang, D. Liu, B. Zhu, W. Huang, S. Wu, S. Zhang, Synthesis, Characterization of Fe-doped TiO_2 Nanotubes with High Photocatalytic Activity, Catal. Letters. 129 (2009) 513–518.

[43] S.S. Penner, Steps toward the hydrogen economy, Energy. 31 (2006) 33–43.

[44] H.J. Choi, M. Kang, Hydrogen production from methanol/water decomposition in a liquid photosystem using the anatase structure of Cu loaded TiO_2, Int. J. Hydrogen Energy. 32 (2007) 3841–3848.

[45] L.S. Yoong, F.K. Chong, B.K. Dutta, Development of copper-doped TiO_2 photocatalyst for hydrogen production under visible light, Energy. 34 (2009) 1652–1661.

[46] J.L. Gole, S.M. Prokes, O.J. Glembocki, Efficient room-temperature conversion of anatase to rutile TiO_2 induced by high-spin ion doping, J. Phys. Chem. C. 112 (2008) 1782–1788.

[47] C.C. Wang, J.Y. Ying, Sol-gel synthesis and hydrothermal processing of anatase and rutile titania nanocrystals, Chem. Mater. 11 (1999) 3113–3120.

[48] Z. Ding, X. Hu, G.Q. Lu, P.-L. Yue, P.F. Greenfield, Novel silica gel supported TiO_2 photocatalyst synthesized by CVD method, Langmuir. 16 (2000) 6216–6222.

[49] X.Z. Li, F.B. Li, Study of Au/Au^{3+}-TiO_2 photocatalysts toward visible photooxidation for water and wastewater treatment, Environ. Sci. Technol. 35

(2001) 2381–2387.

[50] M. Andersson, L. Österlund, S. Ljungström, A. Palmqvist, Preparation of nanosize anatase and rutile TiO_2 by hydrothermal treatment of microemulsions and their activity for photocatalytic wet oxidation of phenol, J. Phys. Chem. B. 106 (2002) 10674–10679.

[51] Y. Zhou, M. Antonietti, Synthesis of Very Small TiO_2 Nanocrystals in a Room-Temperature Ionic Liquid and Their Self-Assembly toward Mesoporous Spherical Aggregates, J. Am. Chem. Soc. 125 (2003) 14960–14961.

[52] K. Nagaveni, M.S. Hegde, N. Ravishankar, G.N. Subbanna, G. Madras, Synthesis and structure of nanocrystalline TiO_2 with lower band gap showing high photocatalytic activity, Langmuir. 20 (2004) 2900–2907.

[53] T. Peng, D. Zhao, K. Dai, W. Shi, K. Hirao, Synthesis of titanium dioxide nanoparticles with mesoporous anatase wall and high photocatalytic activity, J. Phys. Chem. B. 109 (2005) 4947–4952.

[54] J.G. Li, X. Wang, K. Watanabe, T. Ishigaki, Phase structure and luminescence properties of Eu^{3+}-doped TiO_2 nanocrystals synthesized by Ar/O_2 radio frequency thermal plasma oxidation of liquid precursor mists, J. Phys. Chem. B. 110 (2006) 1121–1127.

[55] Q. Xiao, Z. Si, Z. Yu, G. Qiu, Sol-gel auto-combustion synthesis of samarium-doped TiO_2 nanoparticles and their photocatalytic activity under visible light irradiation, Mater. Sci. Eng. B Solid-State Mater. Adv. Technol. 137 (2007) 189–194.

[56] W. Wang, J. Zhang, F. Chen, D. He, M. Anpo, Preparation and photocatalytic properties of Fe^{3+}-doped $Ag@TiO_2$ core-shell nanoparticles, J. Colloid Interface Sci. 323 (2008) 182–186.

[57] N.N. Binitha, Z. Yaakob, M.R. Reshmi, S. Sugunan, V.K. Ambili, A.A. Zetty, Preparation and characterization of nano silver-doped mesoporous titania photocatalysts for dye degradation, Catal. Today. 147 (2009) 76–80.

[58] Y. Liu, J.M. Szeifert, J.M. Feckl, B. Mandlmeier, J. Rathousky, O. Hayden, D. Fattakhova-rohlfing, T. Bein, Niobium-doped titania nanoparticles:Synthesis and assembly into mesoporous films and electrical conductivity, ACS Nano. 4 (2010) 5373–5381.

[59] Q.R. Deng, X.H. Xia, M.L. Guo, Y. Gao, G. Shao, Mn-doped TiO_2 nanopowders with remarkable visible light photocatalytic activity, Mater. Lett. 65 (2011) 2051–2054.

[60] R. Chauhan, A. Kumar, R.P. Chaudhary, Structural and photocatalytic studies of Mn doped TiO_2 nanoparticles, Spectrochim. Acta - Part A Mol. Biomol. Spectrosc. 98 (2012) 256–264.

[61] K.M. Rahulan, L.D. Stephen, C.C. Kanakam, Spectral and nonlinear optical transmission studies of Zr^{4+}-doped TiO_2 nanoparticles, Appl. Surf. Sci. 266 (2013) 326–331.

[62] H. Maki, Y. Okumura, H. Ikuta, M. Mizuhata, Ionic equilibria for synthesis of TiO_2 thin films by the liquid-phase deposition, J. Phys. Chem. C. 118 (2014) 11964–11974.

[63] S. Mugundan, B. Rajamannan, G. Viruthagiri, N. Shanmugam, R. Gobi, P. Praveen, Synthesis and characterization of undoped and cobalt-doped TiO_2 nanoparticles via sol–gel technique, Appl. Nanosci. 5 (2015) 449–456.

[64] W.K. Wang, J.J. Chen, X. Zhang, Y.X. Huang, W.W. Li, H.Q. Yu, Self-induced synthesis of phase-junction TiO_2 with a tailored rutile to anatase ratio below phase transition temperature, Sci. Rep. 6 (2016) 1–10.

[65] B.A. Bregadiolli, S.L. Fernandes, C.F. de O. Graeff, Easy and Fast Preparation of TiO_2 - based Nanostructures Using Microwave Assisted Hydrothermal Synthesis, Mater. Res. 20 (2017) 912–919.

[66] W. Buraso, V. Lachom, P. Siriya, P. Laokul, Synthesis of TiO_2 nanoparticles via a simple precipitation method and photocatalytic performance, Mater. Res. Express. 5 (2018) 115003.

[67] N.C. Horti, M.D. Kamatagi, N.R. Patil, S.K. Nataraj, M.S. Sannaikar, S.R. Inamdar, Synthesis and photoluminescence properties of titanium oxide (TiO_2) nanoparticles: Effect of calcination temperature, Optik 194 (2019) 163070.

[68] Z. Wang, A. Ali Haidry, L. Xie, A. Zavabeti, Z. Li, W. Yin, R. Lontio Fomekong, B. Saruhan, Acetone sensing applications of Ag modified TiO_2 porous nanoparticles synthesized via facile hydrothermal method, Appl. Surf. Sci. 533 (2020) 147383.

[69] R.S. Dubey, S.R. Jadkar, A.B. Bhorde, Synthesis and characterization of various doped TiO_2 nanocrystals for dye-sensitized solar cells, ACS Omega. 6 (2021) 3470–3482.

[70] N. Saikumari, S.M. Dev, S.A. Dev, Effect of calcination temperature on the properties and applications of bio extract mediated titania nano particles, Sci. Rep. 11 (2021) 1–17.

Chapter-2

Experimental tool and techniques

2.1 Thermogravimetric analysis (TGA) & differential scanning calorimetry (DSC)

TGA is an idyllic characterization tool to study a material's thermal features with elevated temperature in a definite atmosphere. In TGA techniques, changes in percentage weight loss of materials are perceived as a consequence of a surge in temperature. The recorded weight loss plot reveals the information about thermal stability, change in materials compositions and kinetic parameters for the chemical reaction in materials. The high precision TGA equipment consists of a thermobalance, programmable temperature-controlled furnace, different gas atmospheres inlet/outlet facility and computer to store and process the results. The procedure to record TGA data initially placed the sample contained crucible in the groove on the sample platform and tare. The second step is steadily surging the temperature of the attached furnace, accordingly placed sample was heated and correspondingly weighed measured on an equipped microbalance. Finally, the mass changes are recorded if a thermal treatment involves removing volatile liquids, gasses, or components [1,2].

DSC is an ideal thermal investigation tool that records the heat flow into or out of a precursor material compared with the known reference sample or empty crucible as a function of elevated temperature with a particular time interval in a medium of a specific gas environment. From the DSC curve, numerous materials properties, i.e., melting point, specific heat capacity, oxidation nature, crystallization, thermal, etc., can be evaluated for the crystallization process of any metals or compounds. DSC observed a heat quantity at elevated temperature, which can absorb or radiate by the precursor sample based on temperature variance amid the precursor concerning reference material [3].

In the current thesis work, simultaneous TGA-DSC data were recorded by Perkin Elmer TGA 4000, as shown in Figure 2.1. Simultaneously weight changes and heat flow in precursor material were measured at elevated controlled temperature in an argon atmosphere.

Figure 2.1 Photograph of TGA instrument (Perkin Elmer TGA 4000)

Synchronized data records of the TGA-DSC curve can expand output and simplifying consideration of the outcomes. Also, the gratis data permits differentiation amongst exothermic and endothermic actions, which have no associated weight loss or loss during the calcination.

2.2 X-ray diffraction (XRD)

XRD is one of the ideally instantaneous analytical and characterization techniques primarily employed to identify the crystalline/amorphous phase of bulk and nanomaterials material. XRD can provide the crystal structures, unit cell dimensions, preferred orientation, thermal expansion and contraction, and atomic spacing information of any crystalline samples. X-ray diffraction functioned based on Bragg's law, which makes constructive interference of monochromatic X-rays when striking on crystalline materials and satisfies the diffraction rules. Diffraction peak arises when incident radiation

wavelength was comparable with atomic spacing sample and endure constructive interference based on Bragg's law. In the crystalline powder sample, the incident radiations were scattered from different lattice planes move apart by d. If the traveled path length of individual rays is equivalent to an integer multiple of incident radiation wavelength, then the constructive diffraction patterns formed. The formation of constructive interference from consecutive planes of the solid crystalline sample follows Bragg's law [4].

$$n\lambda = 2dsin\theta \quad (2.1)$$

here n denotes an integer, λ denotes the wavelength of incident radiation, and θ denotes the angle between scattering planes and incident ray. The crystallite size of the ceramic was evaluated using XRD pattern data, such as full width at half maxima (FWHM) at a diffraction angle [5].

$$D = \frac{K\lambda}{\beta cos\theta} \quad (2.2)$$

here, β denotes FWHM at Bragg angle θ, K denotes shape factor, λ represents the wavelength of X-rays ($CuK\alpha$= 1.54 Å).

The XRD patterns of the prepared different nanoparticles were attained from diffractometer, Brukar 8D advance system as shown in Figure 2.2. The diffractometer has CuKα (λ~1.54 Å) X-ray source that requires an electric supply with 40 kV voltage and 20 mA current. X-ray diffractometer contains an X-ray tube, which can generate radiation having the specific wavelength depends on the cathode metal, a sold slit, rotating samples holder and movable X-ray detector. For recording the XRD data, powder materials/thin film was put on the sample holder, which is in the path of incident X-ray source having a fixed wavelength, while θ and d vary. At a particular angle, the constructive interference formed, which was perceived by the X-ray detector. All these parts of XRD were connected and handled via computer software. The diffraction patterns can assess numerous

crystalline structural parameters, such as unit cell parameters, lattice constant, crystallite size, stress/strain present in the crystalline sample, etc.

Figure 2.2 X-ray diffractometer (Bruker 8D advance)

2.3 Fourier-transform infrared spectroscopy (FT-IR)

FT-IR is a characterization tool applied to acquire an infrared radiation pattern of emission or absorption by inorganic/organic samples. The FT-IR instrument provides spectral data over an extensive electromagnetic range. The total internal energy is the sum of rotational, symmetric/asymmetric vibrational and electronic energy levels. In this spectroscopy techniques, the interaction between active ions and electromagnetic source have been studied. In the infrared (IR) region, an electromagnetic wave is coupled mainly with the molecular vibrations and by absorbing IR radiation molecule is excited to the higher vibration state. Therefore, IR spectroscopy is one of the powerful techniques to find the structure of samples.

The FT-IR equipment work on the principle of Michelson's interferometer technique [6]. The interferometer consists of two mirrors situated at right angles to each other across the beam splitter. One of the mirrors moves its position to a certain distance, and the other one is fixed, and the output beam becomes a resultant of interference of the reflected beam from both the mirrors. On passing the beam through the sample, it creates an interferogram, and by using Fourier transform technique, the infrared spectrum of the material is obtaining. In the current study, FT-IR spectra are obtaining via FT-IR spectrometers (Perkin Elmer), as demonstrated in Figure 2.3.

Figure 2.3 Photograph of spectrum two FT-IR spectrometers (Perkin Elmer)

2.4 Raman Spectroscopy

Raman spectroscopy is the most effective analytical system by which scattered light is perceived to compute the vibrational energy behaviors of materials. Raman spectroscopy is similar to FI-IR, which too provides structural information due to vibrational and rotational modes of the molecular system. When the photon emitted from the laser source interacts with matter in IR to n-UV regions. After photon and matter interactions, three

possibilities to be observed are as follows. The first possibility is that the emitted photons have the same energy as those absorbed, known as Rayleigh scattering. The second possibility is that emitted photons have lost in the form of vibrational energy can be Stokes shift. The third one is that emitted photons have received energy, which is considered as Anti Stokes lines. The latter two possibilities are equally spaced from the Rayleigh line in the Raman spectrum [7].

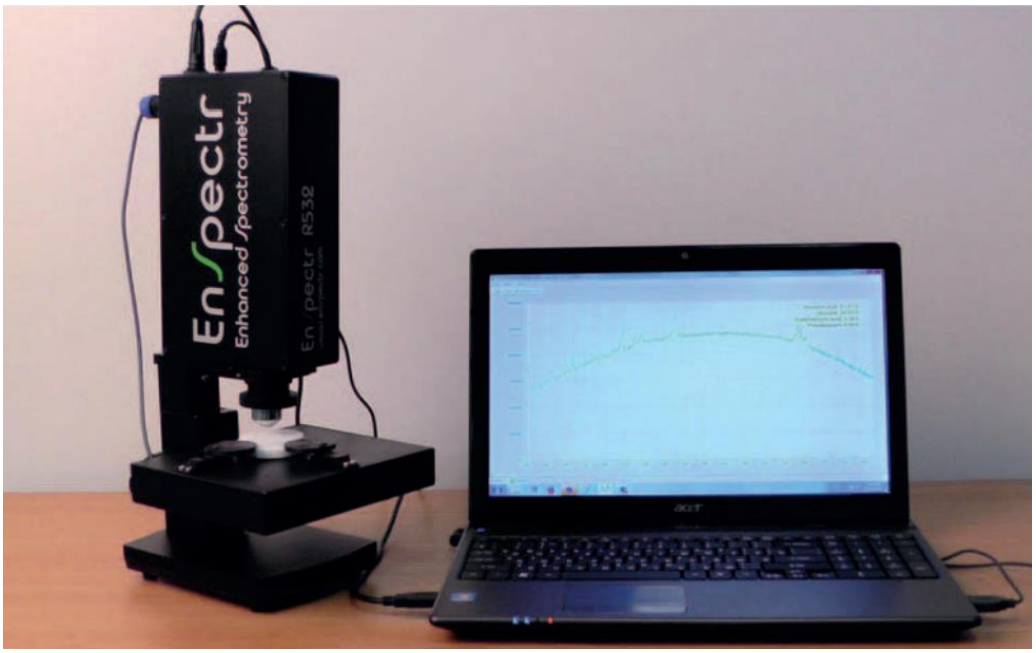

Figure 2.4 Photograph of Enspectr R-532 Raman spectroscopy.

These energy shifts make available essential information about the vibrational modes in the samples. The FT-IR and Raman spectroscopy complement each other because the two techniques define the complete information regarding a material's structural property. However, the main difference between them is the kind of molecular transition observed due to these performances. Raman transition can occur when there is a variation in polarizability of the molecule during vibration transition. It means the electron cloud of the molecule must endure positional change. While for IR demonstrable transition, there must be a change in the dipole moment during vibration [6]. In the present work, Enspectr R-532 Raman spectrograph was used, as displayed in Figure 2.4.

2.5 Field Emission Scanning Electron Microscope (FE-SEM)

FE-SEM is one of the utmost typical characterizations tools to examine the material morphology (particle shapes & size), surface deficiencies, metallographic details and surface topology of micro or nanomaterials. This equipment is also used to explore the elemental conformations within the bulk or nanomaterials samples. The principle of FE-SEM is a most helpful microscope that captures the images of specimen samples by faster scan the high-energy beam of electrons ejected or scattered from the specimen. The principle of FE-SEM is similar to that of the conventional SEM. The only difference lies in the source of electrons produced via field emission rather than thermionic emission. The produced electrons intermingle with the atoms of the sample and producing secondary electrons/signals that comprise evidence about the sample's surface morphology, sample composition, micro/nano size of the sample, and electrical conductivity of the samples [8].

FE-SEM contains a field emission gun, functioned as cathode, anode, scanning coils, magnetic lens, sample stage, secondary and a backscattered electron detector. All these setups were specific software controlled by the high configuration computer system. The emission of electrons from the surface of a cathode tip into a vacuum environment under the stimulus of a very high electric field, recognized as cold emission. It transpires for the reason that the wave function of an electron does not disappear. Thus, there is a finite probability that the electron will be found outside the barrier. A high-energy electron beam was generated from a field emission gun and augmented in a vacuum environment with a very high electrical field potential gradient. These primary electron beams are deflected and focused by electronic lenses, producing a fine directional electron beam that incident on the object.

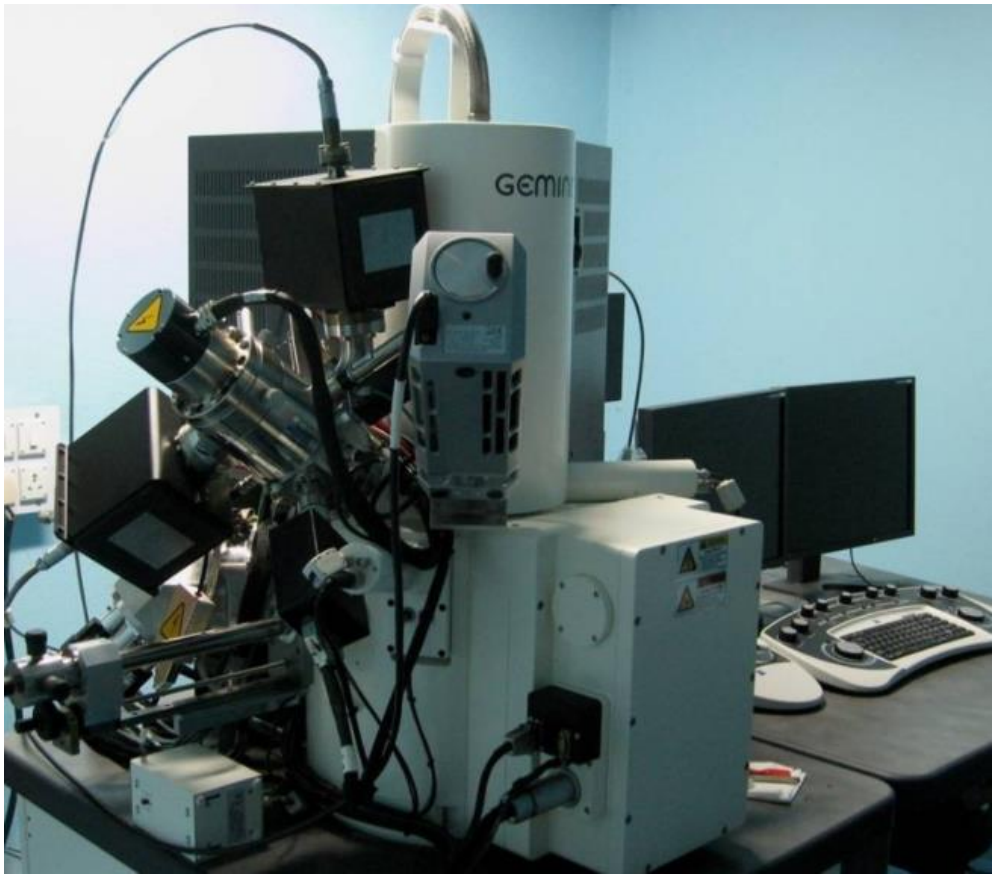

Figure 2.5 Photograph of FE-SEM, Gemini electron-optics

Accordingly, secondary, backscattered electrons, radiation and transmitted electrons are secreted for each sample area. These secondary electrons disclose the morphological feature of the specimen. Many various detectors catch the X-rays, backscattered signals and generate a corresponding electronic signal. This electronic signal is amplified several times and transformed to the final picture that can be seen on a computer monitor and saved for further analysis.

2.6 High-resolution transmission electron microscopy (HR-TEM)

HR-TEM is a prevailing system for determining the nanostructured materials and identifying the phase of materials. A resolution of nearly and high magnification is readily available in TEM these days. The electrons beam is made to fall on the sample from the electron gun, which is transmitted from a very thin specimen where it undergoes interaction. An image is created due to the interface of the transmitted electrons via the

sample in the Cu grid. The produced image is focused and extravagant on an imaging device by a sensor (CCD camera).

The electron interaction with the specimen interactions creates the possibilities of electron microscopy. The energetic electrons in the microscope bombarded the sample, which makes three possibilities; unscattered electrons, scattered electrons elastically and inelastically. Unscattered electrons are transmitted through the thin specimen lacking any interaction exclusive to the sample specimen, which formed darker/lighter images. Atoms scattered elastically scattered electrons in the sample without any loss of energy. The part of scattered electrons was transmitting from the residual servings of the specimen. This pattern can produce information about the atomic arrangements, orientation, and phases of the sample. Scattered electrons in an inelastic manner lost energy during interaction with atoms in a sample. These electrons are then transmitted through the rest of the specimen. These losing energies are exclusive to each bonding state of each element, which can be used to examine the bonding and compositional data of the sample [8,9]. HR-TEM images are conquered from HRTEM, TALOS at an accelerating voltage of 200 kV as seen in Figure 2.6.

HR-TEM includes a multifaceted optical geometry such as a series of objective and condenser lens. At the top electron gun is placed, which generating a stream of high energetic electrons. A series of condenser lenses can focus electron stream into a thin, coherent beam/point source. The highly coherent electron beam incident on the specimen and parts of it are transmitted. The objective lens focuses this transmitted portion into a picture. Finally, the image of the specimen was captured for further analysis. Selected area electron diffraction (SAED) is a crystallographic investigational tool equipped with the HR-TEM/TEM. It gives suggestions and information about crystallographic lattice matching, material phase, d-spacing, plane and defects.

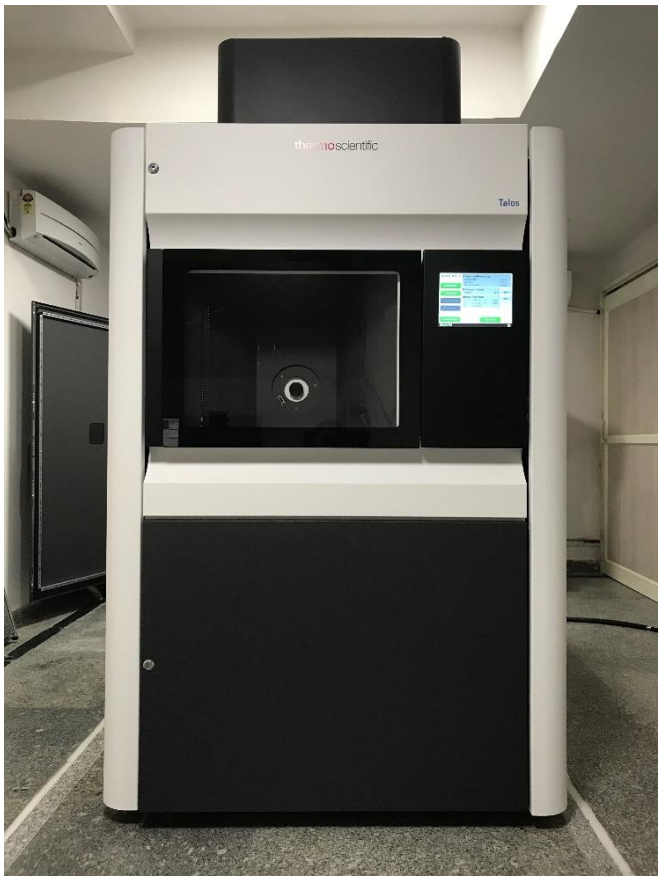

Figure 2.6 Photograph of HRTEM, TALOS

In SAED, the thin crystalline specimen is exposed to a coherent beam of energetic electrons. At this stage, electrons have functioned as wave nature having few thousandths of a nanometer wavelength. The spacing between atoms in crystalline solid is much higher and acts as a grating to the electrons, which creates a diffraction pattern of the crystalline sample. Accordingly, the image on the screen will be a sequence of spots of the diffraction pattern. Each area was conforming to a fulfilled diffraction condition of the crystal structure of the sample.

2.7 UV-Vis spectroscopy

UV-Vis spectrophotometry is a quantifiable apparatus, which can measure the amount of ultraviolet or visible part of light absorbed/transmitted by liquid/solid/thin-film materials concerning the referenced sample. Spectra were obtained based on interaction amongst

matter and light. When the matter transmits or absorbs the light, it experiences excitation and de-excitation, consequential in the conception of a spectrum. According to the Beer-Lambert law, a monochromatic light beam manifestation on a sample comprises a constituent and absorbs a part of radiation. Then the absorbance of a sample is directly proportionate to the concentration of the absorbing constituent in the solution and the path length. Therefore, at the fixed path length, UV/Vis spectroscopy was used to regulate the concentration of the absorber in a solution. The deviations in absorbance with attention were occupied from references solution or samples [10].

Figure 2.7 UV–vis spectrometer of PerkinElmer, Model- lambda 750.

The UV–vis absorption spectroscopy is measured via a dual-beam spectrophotometer made by PerkinElmer, model lambda 750, as illustrated in Figure 2.7. The UV-visible spectrophotometer consists of a light source, monochromators, sample/reference sample, detector, amplifier and recording devices. Tungsten and Deuterium lamps are extensively used as light sources, covering the UV to visible radiation range. Monochromators usually include prisms and slits, which can disperse the primary light source and radiate two monochromatic radiation beams having desired identical wavelength to the sample and reference cell. These two monochromatic radiation beams were passed over the sample solution and the reference solution. The PMT detector can receive the beam from the sample and the reference sample. The signal intensity is very low from the detector, so the amplifier can amplify the signals many times and generate

clear recordable signals. Computers with appropriate software can function as recording devices, storing all the data and visualizing the recorded spectrum.

2.8 Photoluminescence (PL) Spectrofluorometer

PL spectrofluorometer is a contact-less, multipurpose, non-destructive technique to measure excitation and emission spectra of any light-sensitive material, i.e., powder, liquid, glass, or thin-film samples. Characteristically, a light beam impinges a solid or liquid sample, absorbing and getting excited after a specific time de-excited via releasing the radiative emission, preferably in the visible region, along with some non-radiative relaxations [11,12]. PL is the physical phenomenon in which various sources of photonic emission from material at particular excitation energy are achieved. These emitted photons can be composed and studied spectrally and temporally. In semiconductor materials, the radiative transition occurs among the conduction and valence bands, with the energy variance recognized as the optical/energy bandgap. The emitted photons energy narrates the variance in energy levels amid the two-electron states involved in the excited and equilibrium state transition. Mainly, PL measurement setups comprehend a specific wavelength of light generated from a Xenon lamp passed through a monochromator and directed to the sample. The sample absorbed the particular radiations, got excited and later emitted light. The emitted photons from the solid/liquid sample were passed through lenses followed by a monochromator and sensed via a photodetector. The electrical signal produced through the photodetector is transformed into digital form by the convertor and plotted between intensity with respect to wavelength by software on a computer screen. PL excitation and emission spectra for the prepared samples were recorded via the spectrofluorometer (Horiba Jobin Yvon, Fluorolog-3) as presented in Figure 2.8. The PL setup was equipped with a Xenon lamp (450 W) as a source of excitation and double monochromators at both excitation and emission sides [13].

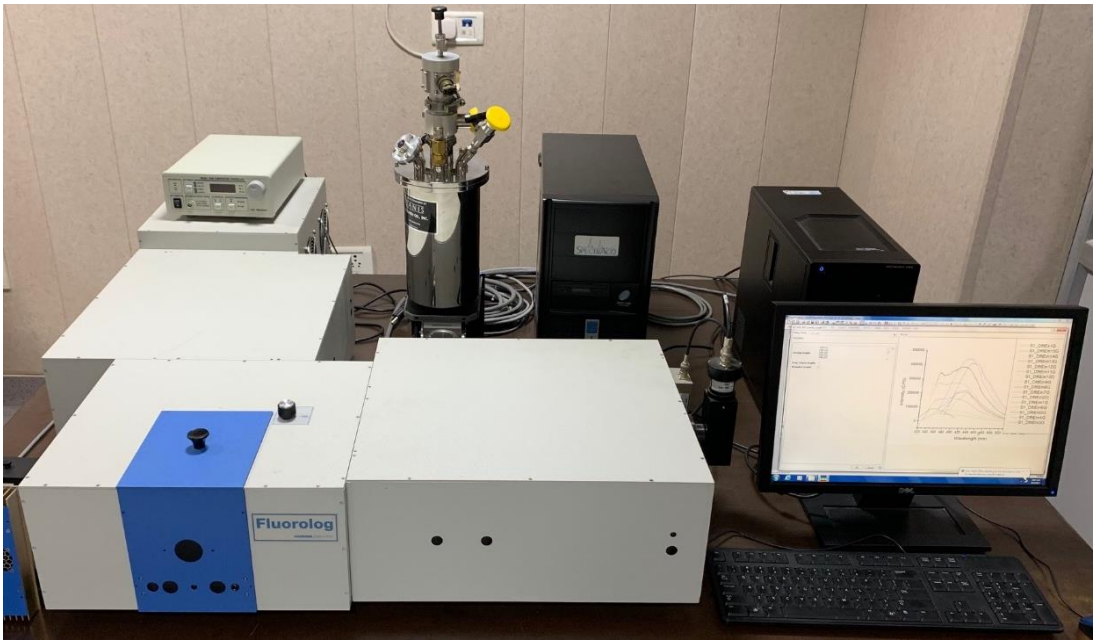

Figure. 2.8 Photograph of Cryostat equipped (Fluorolog-3) spectrofluorometer, Horiba Jobin Yvon.

The above model is also attached with the temperature controller cryostat system for low-temperature PL and decay measurements. The temperature controller system, Janis VNF-100 cryostat, is a multipurpose adjustable temperature by liquid nitrogen consisting of a temperature controller, 50 Ω cartridge heater and silicon diode thermometer. The sample is kept in a quartz cuvette solid sample holder and placed in a liquid Nitrogen vapor atmosphere. The sample temperature was accurately controlled between 77 K to 300 K.

2.9 Time-Resolved Photoluminescence (TRPL)

TRPL is an advancement to the standard spectrophotometer. A pulse light source is used for excitation, and a fast photodetector is used to record the emission of a sample as a function of time after excitation. This system can be applied to record material quality, recognize spectral emissions with definite emissive states, or study energy transfer from one constituent to an alternative in mixed composites/ samples. The recorded lifetime is an intrinsic feature of PL properties that makes available responsiveness to the species excited state dynamics [14,15]. TRPL is one of the most choices for reviewing fast/slow electronic

deactivation processes that result in the emission of photons, a process called decay time or lifetime. This lifetime can be affected by the surrounded molecular as well as contacts with other nearby molecules. Lifetime variations can consequently deliver the evidence nearby the chemical atmosphere or understandings into reaction mechanisms. Emission lifetimes ranged from Picosecond to milliseconds or second, depending on the type of materials or defect present in samples.

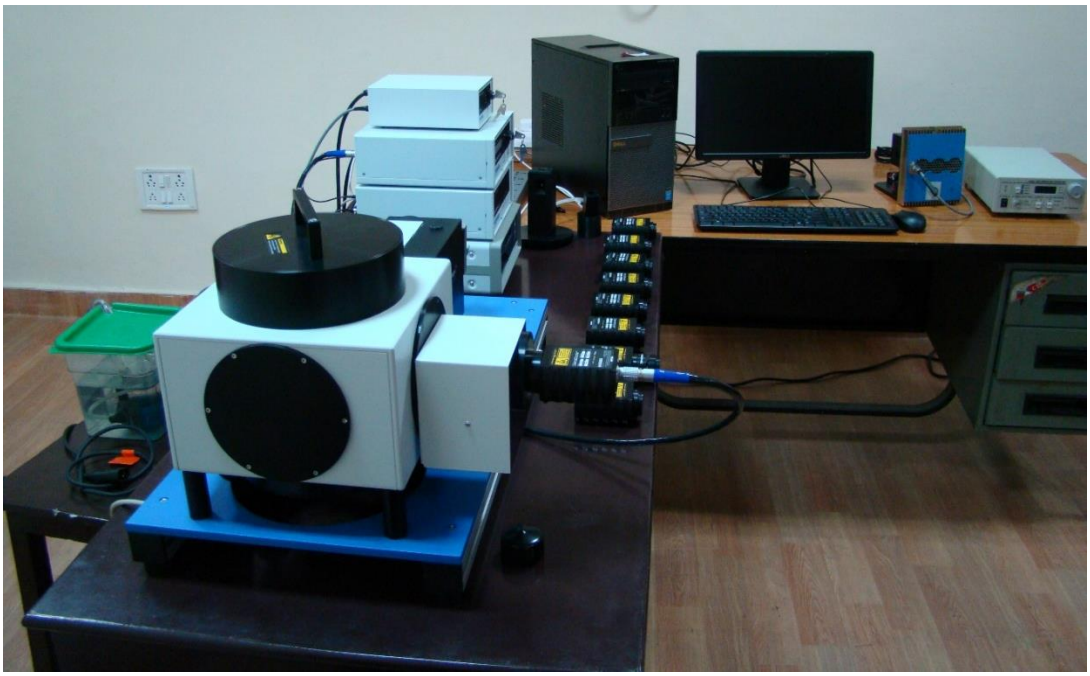

Figure 2.9 Photograph of TCSPC (DeltaFlex-01-DD) measurement unit.

The essential components of the TRPL system are the pulsed light source (pulsed laser, Diodes, LEDs, flash lamp), a monochromator, single-photon photodetector, recording parts such as computers with the proper software. Time-Correlated Single Photon Counting (TCSPC) is a widespread technique for characterizing the TRPL decay curves. The decay curves are recorded with the help of DeltaFlex-01-DD, Horiba Jobin Yvon, as seen in Figure 2.9. Delta diodes laser as pulse source and photomultiplier tube as detector attached to the instrument. All the recorded decay curves were analysed through the least square fitting method. The instrument response function was taken by Ludox scatterer [13].

2.10 Electroabsorption (E-A) spectroscopy

External electric fields influenced optical spectra were extensively used to examine photoexcitation dynamics and electronic structures of the samples. The E-A signal measurement is a powerful procedure to the determination of the magnitude of changes in polarizability ($\Delta\alpha$) and electric dipole moment ($\Delta\mu$) following the Stark effects on optical transitions. The $\Delta\mu$ and $\Delta\alpha$ can be attained from the absorption spectrum and E-A signal, with the simulating of the detected E-A signal. A theory related to the electric field effect on the absorption of polarized light by an ensemble of mobile molecules was first developed by W. Liptay's, "Theory of the Stark effect" in 1974 [16-18]. Absorption and E-A spectra concerning a specified electronic transition were correlated, and the E-A signal was assumed as a linear combination of 0th, 1st and 2nd derivatives of the absorption spectrum. The $\Delta\mu$ and $\Delta\alpha$ can be calculated with the coefficients of derivative component of the E-A signal.

The aforementioned investigation procedure can be defined by the differential method, which is appropriate only when the separation exists between the absorption and the corresponding E-A bands. On the other hand, if there is no separation between the absorption band that corresponds to observed E-A bands, in that case, unidentified by the differential method. In this unidentified case, another type of analysis of the E-A signal is used named as an integral method. In the integral method, E-A signals were integrated along their wavenumber as a resulting signal are simulated with derivatives and integrals of the absorption spectra [19]. In the present absorption and E-A spectrum, we prefer the integral method rather than the differential method. Figure 2.10 shows the block diagram of the experimental setup of electric field modulation spectroscopy for absorption measurement. The absorption spectra of a thin film are measured with a Jasco, FP- 777 spectrophotometer using an external PMT.

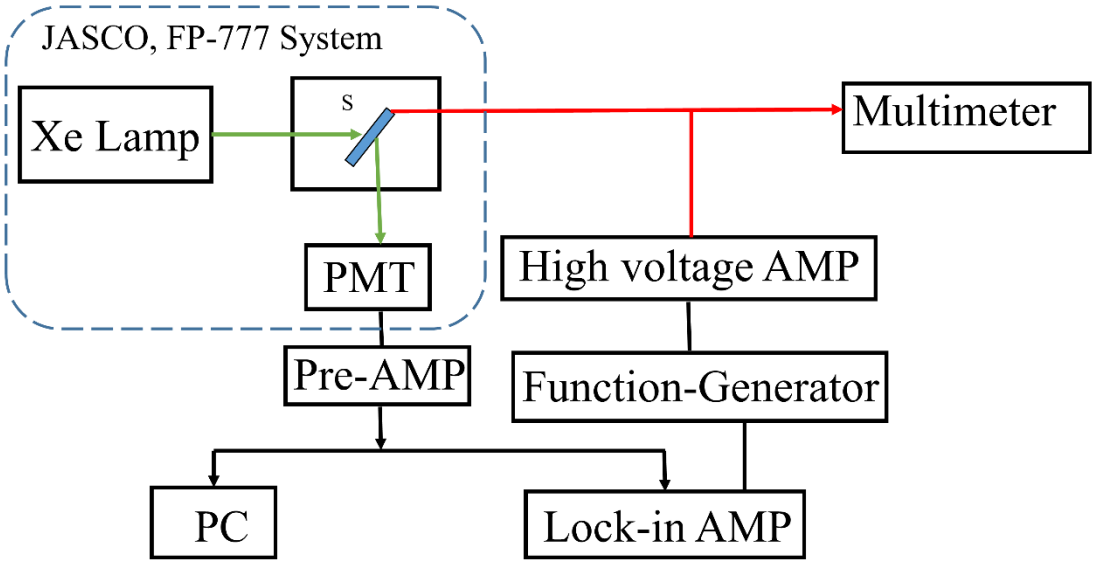

Figure 2.10 Experimental setup of electroabsorption measurement.

For the E-A measurement, a modulated external electric field was applied to the sample film, which was simultaneously shined by the 150 W continuous xenon lamp (from FP-777), incorporated and controlled altogether in the apparatus, as described elsewhere [20]. The temperature-dependent E-A spectra were obtained using Daikin, a V202C5LR cryogenic refrigerating system equipped with quartz optical windows. A temperature controller (Scientific Inst. model 9600) was used to control the sample film's temperature with a silicon diode thermometer attached to the sample. E-A spectra were obtained by plotting the field-induced change in absorption intensity as a function of wavenumber. The obtained experimental data are analyzed by using special software, which is known as IGOR software.

References

[1] M. Wagner, Thermal Analysis in Practice: fundamental aspects, Therm. Anal. Pract. (2017) 1–349.

[2] A. Nithya, H.L. Jeevakumari, K. Rokesh, K. Ruckmani, K. Jeganathan, K. Jothivenkatachalam, A versatile effect of chitosan-silver nanocomposite for surface plasmonic photocatalytic and antibacterial activity, J. Photochem. Photobiol. B Biol. 153 (2015) 412–422.

[3] S. Vyazovkin, N. Koga, C. Schick, (Eds.) Handbook of thermal analysis and calorimetry, Volume 6: Recent advances, techniques and applications; Elsevier: Amsterdam, The Netherlands, 2018.

[4] B. Cullity, Elements of x-ray diffraction, second edition., Addison-Wesley Publishing Company Inc., Reading MA, 1978.

[5] H.M. Moghaddam, S. Nasirian, Dependence of activation energy and lattice strain on TiO_2 nanoparticles? Nanosci. Methods. 1 (2012) 201–212.

[6] P. Larkin, Infrared and Raman spectroscopy: principles and spectral interpretation. Elsevier, 2017.

[7] G. Keresztury, Raman spectroscopy: Theory. Handbook of vibrational spectroscopy (2006).

[8] R.F. Egerton, Physical principles of electron microscopy: An introduction to TEM, SEM, and AEM, Phys. Princ. Electron Microsc. An Introd. to TEM, SEM, AEM. (2005) 1–202.

[9] S.M. Bhagyaraj, O.S. Oluwafemi, N. Kalarikkal, S. Thomas, Characterization of nanomaterials: Advances and key technologies, Charact. Nanomater. Adv. Key Technol. (2018) 1–390.

[10] G. Wypych, Handbook of UV Degradation and Stabilization: Second Edition, Handb. UV Degrad. Stab. Second Ed. (2015) 1–419.

[11] C.R. Ronda, Luminescence: from theory to applications, (2008) 260.

[12] J.R. Lakowicz, Introduction to Fluorescence, Princ. Fluoresc. Spectrosc. (1983) 1–18.

[13] M.K. Singh, M.S. Mehata, Enhanced photoinduced catalytic activity of transition metal ions incorporated TiO_2 nanoparticles for degradation of organic dye: Absorption and photoluminescence spectroscopy, Opt. Mater. 109 (2020) 110309.

[14] K. Wakabayashi, Y. Yamaguchi, T. Sekiya, S. Kurita, Time-resolved luminescence spectra in colorless anatase TiO_2 single crystal, J. Lumin. 112 (2005) 50–53.

[15] D. V. O'Connor, D. Phillips, Time-correlated single photon counting, (1984) 288.

[16] W. Liptay, in: E.C. Lim (Ed.), Excited States, Academic Press, New York, 1974, p. 129.

[17] G. U. Bublitz, S. G. Boxer, Stark Spectroscopy: Applications in chemistry, biology, and materials Science, Annu. Rev. Phys. Chem. 48 (1997) 0213–42.

[18] E . Jalviste, N. Ohta, Theoretical foundation of electroabsorption spectroscopy: Self-contained derivation of the basic equations with the direction cosine method and the Euler angle method, J. Photochem. Photobiol. C Photochem. Rev. 8 (2007) 30–46.

[19] K. Awasthi, T. Iimori, N. Ohta, Integral method analysis of electroabsorption spectra and its application to quantum dots of PbSe, J. Phys. Chem. C 118 (2014) 18170–6.

[20] S. Umeuchi, Y. Nishimura, I. Yamazaki, H. Murakami, M. Yamashita, N. Ohta, Electric field effects on absorption and fluorescence spectra of pyrene doped in a PMMA polymer film, Thin Solid Films 311 (1997) 239–45.

Chapter-3

Optical and photocatalytic performance of titanium dioxide nanoparticles*

3.1 Introduction

Titanium dioxide (TiO_2), also known as titania, has varied applications due to its crystalline structure and morphology. It has three different phases, namely anatase, brookite, and rutile phase (Fig. 3.1). Among these phases, anatase and rutile bear tetragonal structure, while brookite has an orthorhombic structure. The rutile phase is thermodynamically more stable than the other phases of titania.

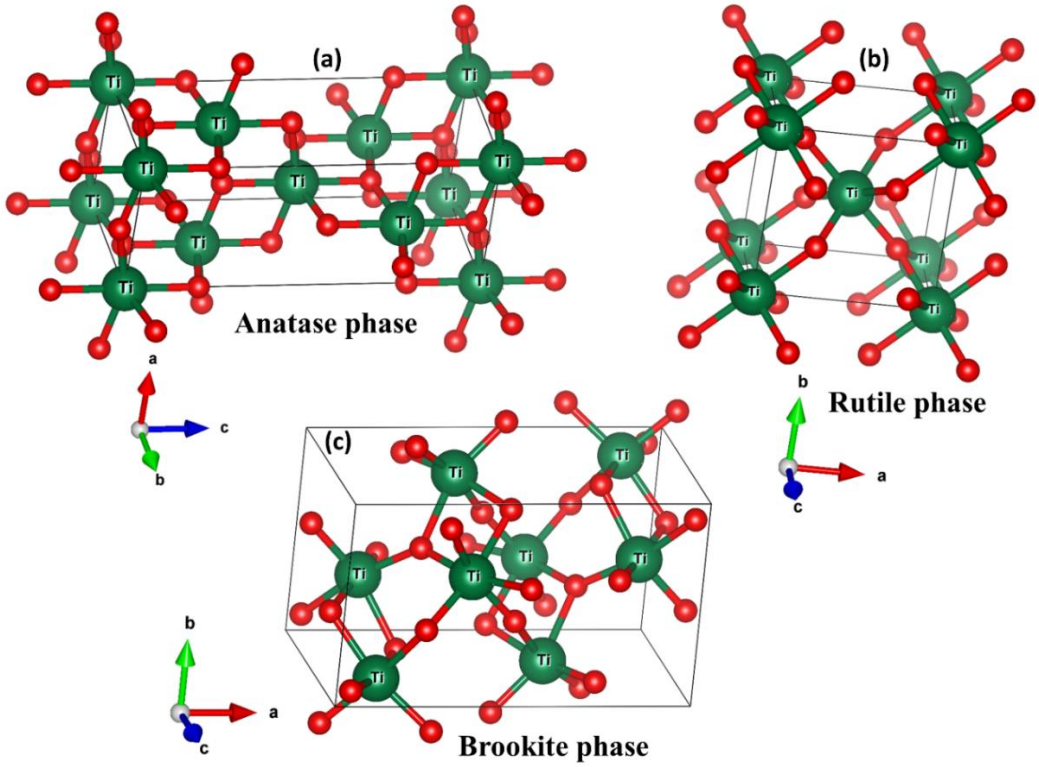

Figure 3.1. Crystal structure of anatase, rutile and brookite phase of TiO_2 NPs.

*Content of this chapter have been published in **Optik 193 (2019) 163011.**

Temperature-dependent transformation of TiO_2 occurs from amorphous to anatase and further to the rutile phase. Titania is a wideband semiconductor with an energy band gap of 3.2 eV for the anatase and 3.0 eV for the rutile phase [1]. TiO_2 has been extensively studied [1,2] in various electronics applications, transparent conductivity and utilization as a photocatalyst depending on its morphology, crystallite size and crystalline structures. Due to its light absorption properties, it may be used as an antibacterial agent to decompose small organisms [3,4].

In the present developing era, one of the major causes of pollution is industries producing paint, plastic, textile, paper, cosmetics, etc. Industries discharge many pollutants like heavy metals, aromatic compounds, petroleum hydrocarbons, toxic dyes, etc., which are hazardous to the environment. Among these pollutants, a fluorophore named Rhodamine B (RhB) belongs to the family of xanthene's dye broadly used in textile, cosmetic, laser and pigments [5,6]. This fluorophore drained out of industries is generally dumped in major water bodies causing critical health issues and sometimes responsible for cancer. Therefore, these harmful dyes need to degrade to preventing health issues. The photocatalytic activity of titania nanoparticles (NPs) is primarily identified by their crystalline phase (anatase and rutile), pore size, aspect ratio, and crystallinity [7–9].

TiO_2 has been produced by various methods such as sol-gel technique with alkoxide as precursors [10,11], hydrothermal method [12,13], ultrasonic irradiation [14,15], flame synthesis [8,16], chemical vapor deposition (CVD) [17], chemical precipitation method [18,19], microwave succoured hydrothermal technique [20], sputtering [21], thermal plasma [22]. Among these methods, the sol-gel technique is the most favourable because of the production of nanoparticles with improved crystallinity and large surface area nanoparticles [23–25]. Therefore, in this work sol-gel method is used to synthesize the titania nanoparticles. The sol-gel method gives approachability for synthesizing titania

nanoparticles with different morphologies such as particles, wires, sheets, rods, tubes, mesoporous and aerogels.

In the present work, titania NPs were synthesized by a sol-gel technique using titanium (IV) isopropoxide (TTIP) as a precursor. Calcination was performed at different temperatures to developed pure anatase, mixed (anatase and rutile) and pure rutile phases of TiO_2. The produced TiO_2 NPs were explored with different techniques to understand the morphology and especially their applications as photocatalytic activities of dyes [26].

3.2 Materials and Methods

All the chemicals and solvents used to prepare as-synthesized TiO_2 NPs were of spectroscopic grade and used without further purification. Titanium (IV) isopropoxide ($C_{12}H_{28}O_4Ti$, TTIP, Alfa Asear 97%), isopropyl alcohol ($(CH_3)_2CHOH$, Fisher scientific assay 99%), hydrochloric acid (HCl, Thomas Baker 35.4%), absolute ethanol (C_2H_5OH, analytical grade), Rhodamine B ($C_{28}H_{31}ClN_2O_3$, CDH) and deionized water (H_2O adrona B30/integrity+, 18.2 MΩ×cm) were used.

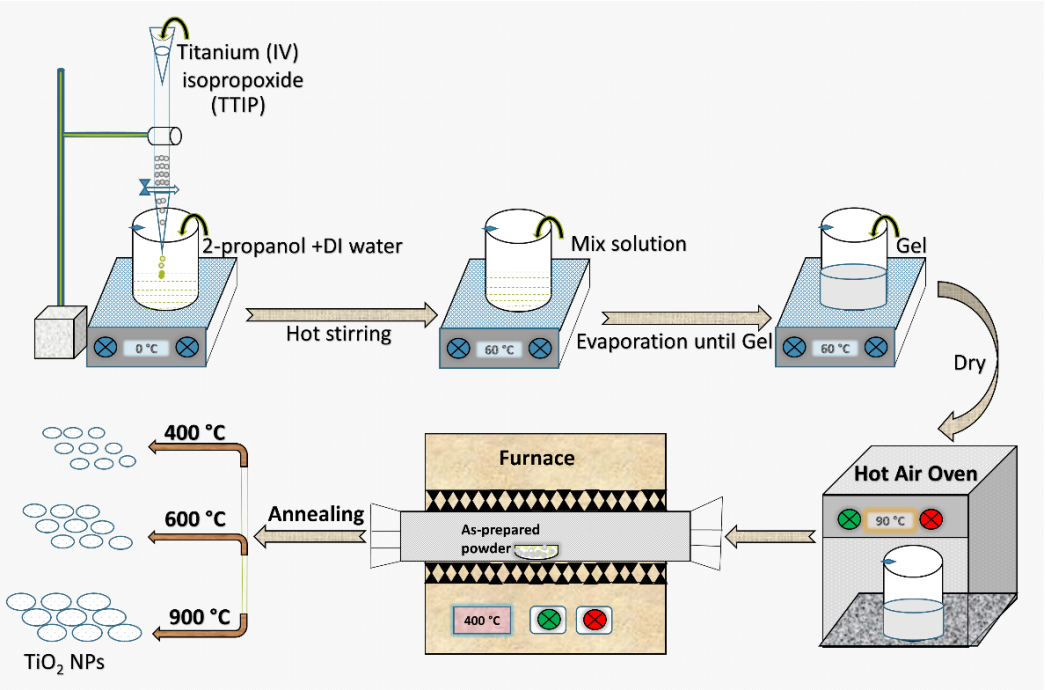

Figure 3.2. Schematic representation of the synthesis route of TiO_2 NPs.

All the substances were washed and dried before used. A 0.05M solution of TTIP was added dropwise into the 50 ml solution of isopropyl alcohol (IPA) and de-ionized (DI) water (9:1) under continuous stirring into a round bottom flask. After 2 h, diluted HCl was added into the TTIP solution to maintain the pH of the solution and kept under constant stirring at 60ºC until the gel was obtained. The obtained gel was dried and washed with DI water and ethanol then heated at 90 ºC temperature in the oven. After annealing (using tubular furnace of MTI, OTF-1200X, USA) at different temperatures of 400, 600 and 900 ºC (with an accuracy of ± 1 ºC), TiO_2 nanocrystalline powder was obtained. The schematic representation of the synthesis of titania nanoparticles is shown in Figure 3.2.

3.3 Characterization Techniques

The X-ray diffraction (XRD) patterns of TiO_2 were measured with Ultima IV, Rigaku equipped with CuKα radiation and an acceleration voltage of 40 kV and 20 mA applied current. Raman spectra were recorded by using Raman spectroscopy (Enspetr R-532, USA). The surface morphology of titania was recorded by using field emission scanning electron microscopy (FESEM, Gemini electron-optics) with an acceleration voltage of 0.1-30 kV. High-resolution transmission electron microscopy (HRTEM) images were obtained from (Jeol-2010) operated at an accelerating voltage of 200 kV. Differential scanning calorimetry (DSC) and thermogravimetric analysis (TGA) parameters were measured by Perkin Elmer TGA 4000. Fourier transform infrared spectroscopy (FTIR) spectra were obtained from spectrum two FTIR spectrometers (Perkin Elmer). Diffuse reflectance and absorption spectra of TiO_2 NPs were recorded by UV/VIS/NIR spectrometer (Lambda-750, Perkin-Elmer). Photoluminescence (PL) and PL-excitation spectra were recorded with Fluorolog-3 (Horiba Jobin Yvon)equipped with double-grating at excitation and emission monochromators [24]. Samples were irradiated with a Cole-Parmer UV lamp (8 watts, 254 nm, 1.2 mW/cm^2).

3.4 Results and discussion

The TGA curve of TiO_2 NPs is shown in Figure 3.3(a). The aggregate weight loss observed in the temperature range 27 – 900 °C was 17.03% for TiO_2 NPs. The weight loss of the sample with temperature occurs in three stages. The first stage of weight loss is noticed from room temperature (27 °C) to 150 °C due to the evaporation of absorbed water from the surface of the nanoparticles. The second stage of the weight loss occurs from 150 to 420 °C is caused by the loss of the chemisorbed water, solvents and organic groups available within the sample [27]. In the third stage, between 420 – 900 °C, the mass loss is relatively low and is about 0.58%.

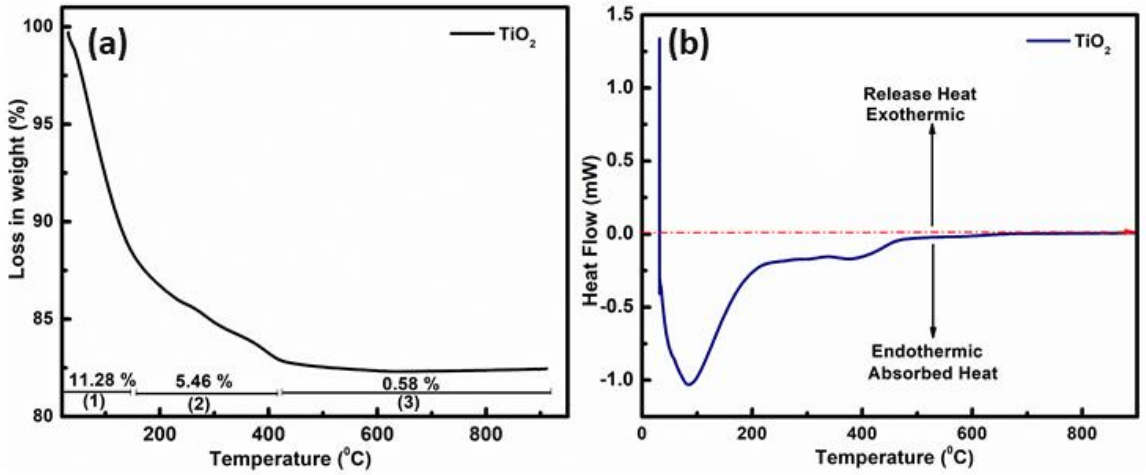

Figure 3.3. TGA curve (a) and DSC curve (b) of TiO_2 nanoparticles.

Figure 3.3 shows the DSC curve of TiO_2 NPs. The endothermic peak observed at around 96 °C is attributed to the release of physisorbed water and the decomposition of organic solvents and other elements that constituted the alkoxide [28,29]. The peak at around 400 °C in the TiO_2 NPs shows a phase transformation from amorphous to crystalline structure [30].

Figure 3.4 shows the XRD diffraction patterns of developed TiO_2 powder calcined at different temperatures of 400, 600 and 900 °C. At 400 °C, the instant diffraction peaks appeared at 2θ are 25.27°, 38.02°, 47.92°, 54.35°, 55°, 52.80° and 68.96° corresponding

to the reflection from (101), (004), (200), (105),(211), (204) and (116) crystal planes, respectively of anatase phase with tetragonal titania structure.

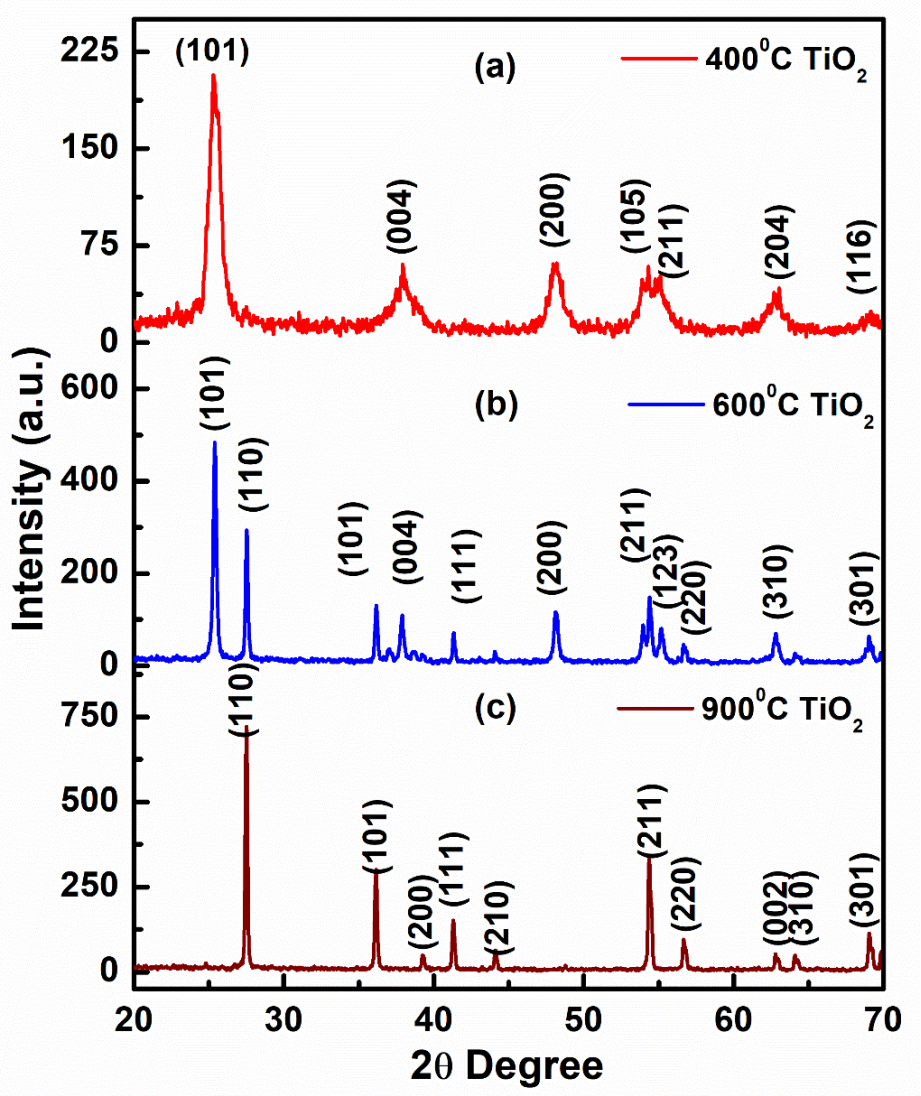

Figure 3.4. XRD patterns of TiO_2 NPs at produced at (a) 400°, (b) 600° and (c) 900°C.

When calcined at 600 °C, the instant diffraction peaks appeared at 2θ are 25.39°, 27.52°, 36.19°, 37.85°, 41.31°, 48.09°, 54.39°, 55.18°, 56.73°, 62.81° and 69.09° correspond to the reflections from (101), (110), (101), (004), (111), (200), (211), (123), (220), (310) and (301) crystal planes, respectively of mixed-phase (anatase and rutile) of TiO_2 structure. In the final stage, at 900 °C, the instant diffraction peaks appeared at 2θ are 27.52°, 36.15°, 39.24°, 41.29°, 44.14°, 54.36°, 56.67°, 62.85°, 64.08° and 69.10° correspond to reflections from (110), (101), (200), (111), (210), (211), (220), (002), (310),

(301) crystal planes of rutile phase with tetragonal TiO_2 structure. The observed XRD peaks are in good agreement with the standard spectrum of JCPDS no.: 01-21-1272, 01-084-1286 and 01-073-1765.

The average crystallite size (D) of synthesized TiO_2 NPs was estimated by using Scherrer's Eq. (3.1) [31].

$$D = \frac{k\lambda}{\beta \cos\theta} \quad (3.1)$$

Here, *k* denotes the shape factor having a value of 0.89, λ denotes the x-ray wavelength corresponding to Cu K_α radiation, β denotes the full-width at half maximum (FWHM) of observed peak and θ denotes the diffraction angle. The crystallite size calculated from Eq. (1) is 21, 36 and 54 nm for anatase, mixed, and rutile phases of TiO2 NPs. Also, it has been noticed that the characteristic peaks assigned to the rutile phase of TiO_2 are most intense as compared to the mixed and rutile phases, which might be due to the enhancement in the crystallite size upon increasing the calcination temperature, as shown in Fig. 3.4 (b,c).

Figure 3.5 illustrates the FESEM micrographs of titania nanopowder produced and calcinated at 400, 600 and 900 °C. The FESEM images clearly show the compact size of the NPs calcinated at 400 °C and seem to be agglomerated. With an increase in calcination temperature up to 900 °C, the particle size increases, the micrographs show the uniform distribution of well-connected grains and the crystallite size of NPs. While accelerating to the higher annealed temperature, the crystallinity of titania NPs increases, which might be due to the structural phase transformation of TiO_2 (Fig. 3.5c), as also reflected in the XRD patterns [32].

Figure 3.6 shows the HRTEM image of TiO_2 NPs annealed at 400 °C. The particles are non-spherical in shape with a size of about 12 to 18 nm. It is evident from the micrograph that the prepared TiO_2 NPs are considerably small and crystalline.

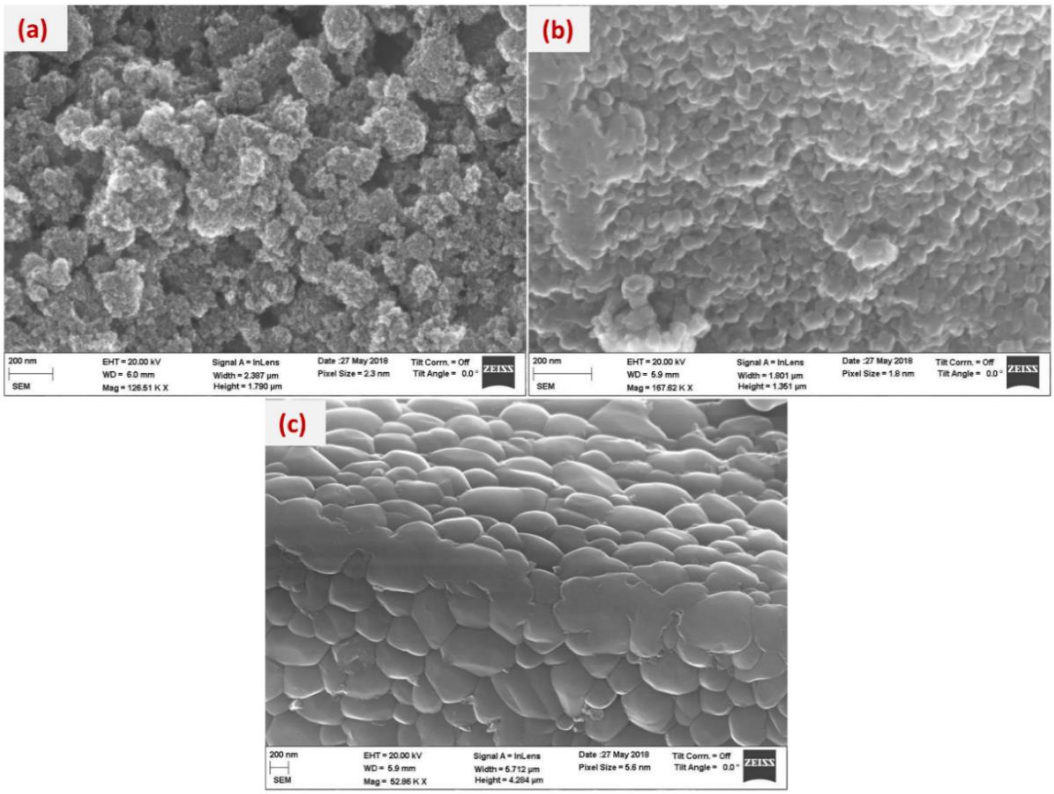

Figure 3.5. FESEM images of TiO_2 NPs at produced at (a) 400°, (b) 600° and (c) 900°C.

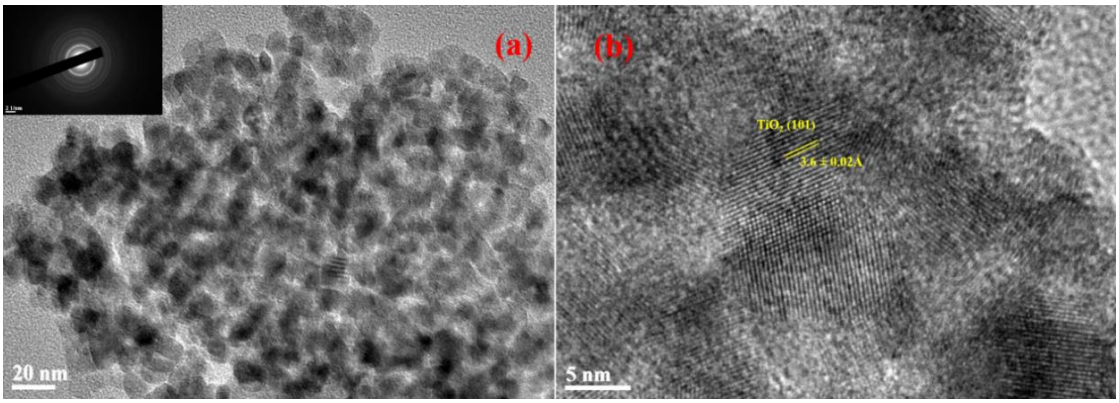

Figure 3.6. The HRTEM images of TiO_2 NPs (a, b). The inset of image (a) shows the corresponding SAED pattern.

The lattice image of TiO_2 nanoparticles (Fig. 3.6b) with a lattice spacing of 0.36 ± 0.02 nm indicates the (101) plane of the anatase phase. The bright spot in the center point (inset Fig. 3.6a) of the image corresponds to the randomly diffracted electron by the TiO_2 NPs hence further confirmation of the crystalline nature of the produced materials [33].

Figure 3.7 shows the FTIR spectra of prepared titania nanopowder calcined at a temperature of 400, 600 and 900 °C in the range of 400 – 4000 cm^{-1}. The IR absorption bands appeared at around 3305, 1634 cm^{-1} corresponds to the symmetric/asymmetric stretching mode of vibrations and bending mode of vibration of the hydroxyl group (–OH or O-H bond), respectively present in the sample, which might be due to the moisture and of the absorbed water molecules [34,35].

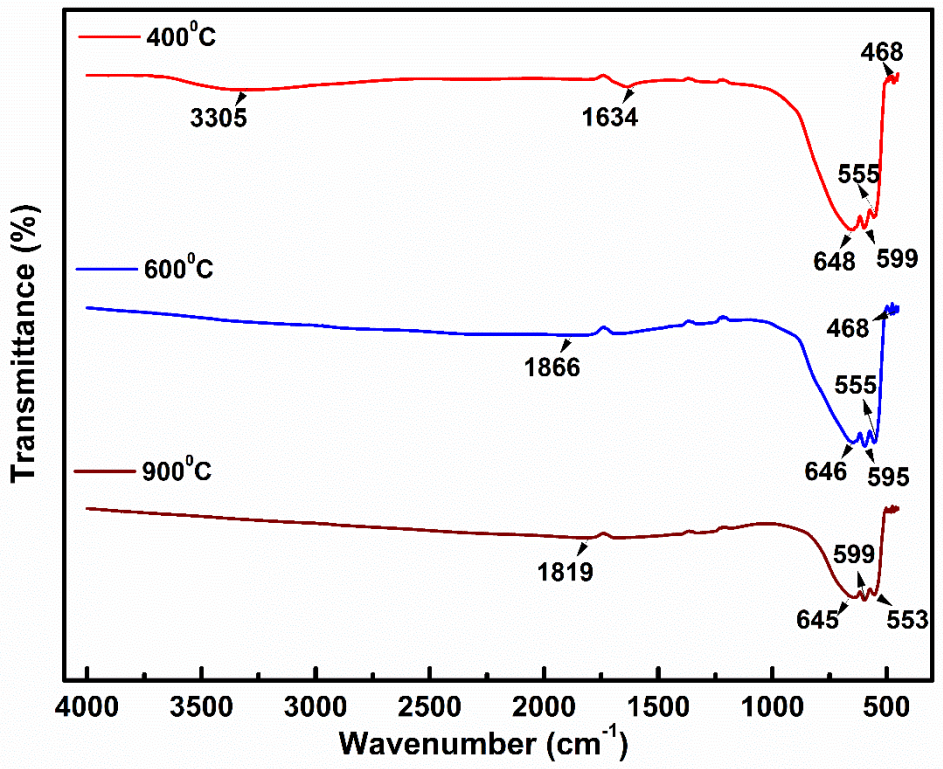

Figure 3.7. FTIR spectra of TiO_2 NPs produced at (a) 400, (b) 600 and (c) 900 °C.

The –OH bond-related peak in the spectrum is because of (H_2O) on the surface of NPs absorbed chemically and physically. At higher annealing temperatures, the observed IR absorption peaks at around 1866 and 1819 cm^{-1} correspond to C=C and C=O stretching modes of vibration, respectively. The broad-band that arises in between 1000 to 400 cm^{-1} is related to Ti-O and Ti–O–Ti stretching and bridging stretching modes, respectively [36]. The peaks at around 648, 599, 555 and 468 cm^{-1} are attributed to the characteristics peak of TiO_2 NPs.

Table 3.1. The FTIR absorption frequencies and their preliminary vibrational assignments of TiO_2 NPs.

Wavenumber (cm^{-1})			**Tentative vibrational assignments**
400 °C	**600 °C**	**900 °C**	
3305	-	-	O–H stretching
-	-	1819	C=O stretching
-	1866	-	C=C stretching
1634	-	-	O–H bending
648	646	645	Ti–O–Ti bond stretching
599	595	599	Ti–O–O bond
555	555	553	Ti–O bond
468	468	-	Anatase titania

It has been reported that the broad absorption band between 400- 900 cm^{-1} region is due to the vibration of the Ti–O–Ti linkage [37] and the peak at around 468 cm^{-1} is assigned to the vibrational of Ti–O bond in TiO_2 (anatase) lattice. The IR absorption frequencies observed in titania nanopowder at different annealing temperatures and the corresponding bond and mode of vibrations are summarized in Table 3.1.

Figure 3.8 illustrated the Raman spectra of the TiO_2 NPs produced at different annealing temperatures. According to factor group analysis, anatase has five Raman bands, i.e., $A_{1g}+B_{1g}+3E_g$. These five Raman bands are at 639.76 (E_g), 515.0 (A_{1g}), 401.50 (B_{1g}) and 199.49 cm^{-1} (E_g), 147.48 cm^{-1} (E_g) for titania nanopowder produced at 400 °C. The

147.48 cm^{-1} band is sharp and intense, and these peaks correspond to the TiO_2 NPs anatase phase [38].

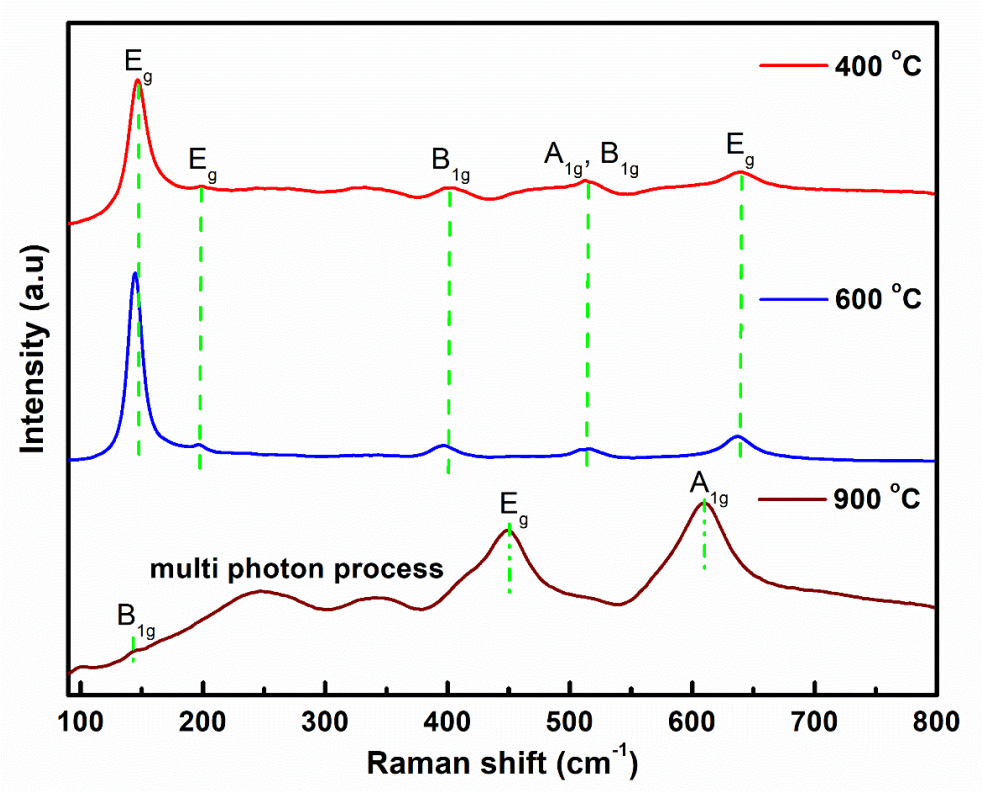

Figure 3.8. Raman spectra of TiO_2 NPs annealed at three different temperatures.

When the temperature increases up to 600 °C, the broadening of the peak is decreased; hence the crystallinity of the sample is increased. When the sample of TiO_2 is thermally treated at 900 °C, Raman bands at 141.80, 449.03, and 611.16 cm^{-1} are observed corresponding to the B_{1g}, E_g and A_{1g} modes of rutile phase, respectively [39]. The bands at 248.26 and 339.03 cm^{-1} assigned to the multiphoton process of the rutile phase of TiO_2 NPs [40].

Figure 3.9 shows the UV-Vis reflectance and absorption spectra of TiO_2 NPs calcinated at various temperatures. The reflectance edge and absorption peak of TiO_2 NPs shift towards red, i.e., from 326 to 380 nm, while increasing the annealing temperature. The apparent shift in absorption is correlated to the phase transformation from anatase to rutile.

This is further related to increased NPs size and crystallinity, which may be due to charge transfer towards the surface.

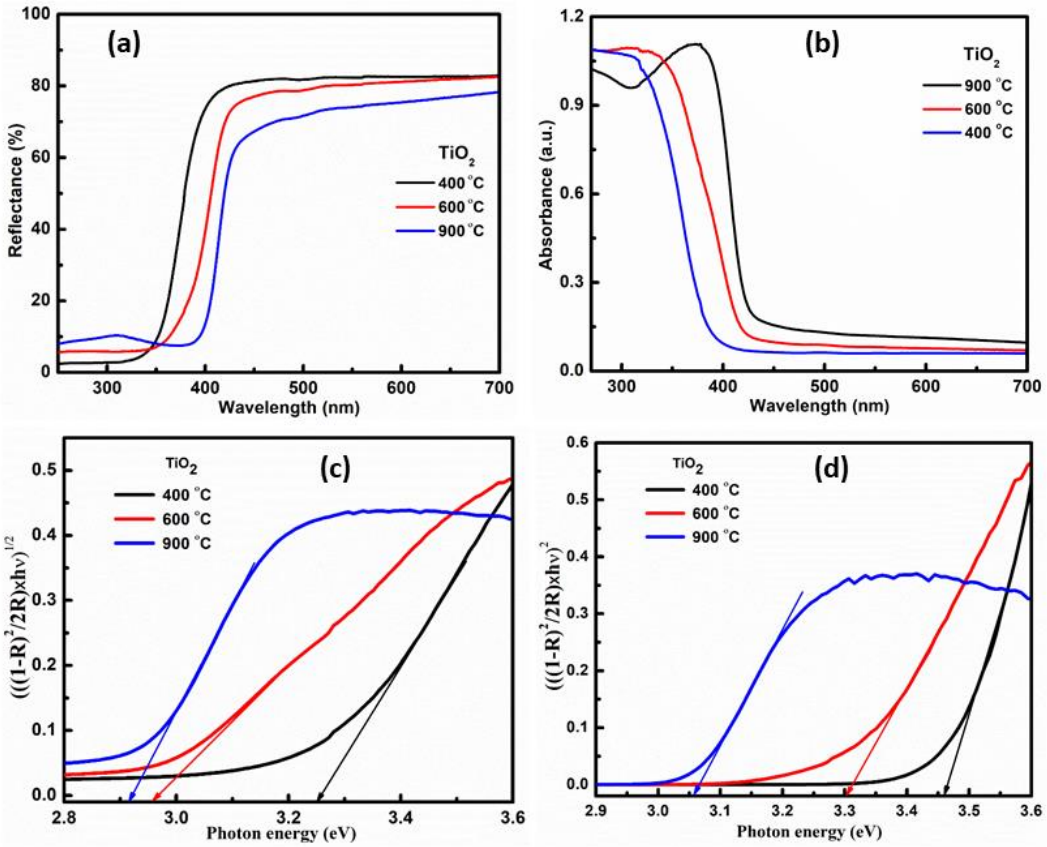

Figure 3.9. UV-Vis diffuse reflectance spectra (a), absorption spectra (b) and Tauc plots for the possibility of indirect bandgap (c) and direct bandgap (d) of TiO_2 NPs.

For the estimation of the optical band gap (shown in Fig. 3.9c,d), the observed diffuse reflectance spectrum is converted to Kubelka-Munk function (K-M) or F(R). The F(R) method is based on the following equation [41,42].

$$\frac{\alpha}{S} = \frac{(1-R)^2}{2R} = F(R) \qquad (3.2)$$

where R is the reflectance, F(R) is proportional to the extinction or absorption coefficient (α) and ***s*** scattering coefficient. The K-M function can be reproduced using Tauc [43,44] Eq. (3.3).

$$(h\nu\alpha)^{1/n} = A(h\nu - E_g) \qquad (3.3)$$

$$(F(R) \times h\nu)^{1/n} = A(h\nu - E_g) \quad (3.4)$$

where ***h*** is Planck's constant (J.s) and ν is the light frequency (s^{-1}) and hν is photon energy and the coefficient ***n*** associated with an electronic transition. The bandgap of TiO_2 NPs can be obtained from the modified K-M equation, in which ***n = 1/2*** for a direct bandgap transition and ***n=2*** for an indirect bandgap transition. The bandgap of TiO_2 NPs is obtained by plotting Eq. (3.4) as a function of the photon energy (h*ν*) in eV and the estimated values are given in Table 3.2. The bandgap for anatase has corresponded to the indirect bandgap, whereas for rutile, it is close to the direct bandgap [45]. TiO_2 NPs show the indirect bandgap structure at a lower temperature of 400 °C and the direct bandgap at a higher temperature of 900 °C. Thus, the bandgap of TiO_2 NPs decreases with the phase transformation from anatase to rutile.

Table 3.2. Bandgap energies for bare TiO_2 nanoparticles.

Temperature (°C)	Direct bandgap (eV)	Indirect bandgap (eV)
400 °C	3.46	3.21
600 °C	3.30	2.95
900 °C	3.05	2.90

The photoluminescence (PL) spectra of the three structures of TiO_2 NPs obtained at different temperatures (400 - 900 °C) are shown in Figure 3.10. The PL spectrum of the pure anatase phase of the NPs has a broad band with a maximum at 414 nm and is independent of the excitation wavelength. The PL band of mix phase with similar shape-shifts towards longer wavelength region and shifted further for pure rutile phase of TiO_2 NPs and peaked at 427 nm. The PL-excitation measured at PL maximum is shown in the inset of Figure 3.10 and is quite similar to the absorption spectra indicating that there are

no excited state reactions. Stoke's shift estimated using absorption and PL is maximum for the anatase phase (98 nm) and indicated towards the indirect bandgap structure.

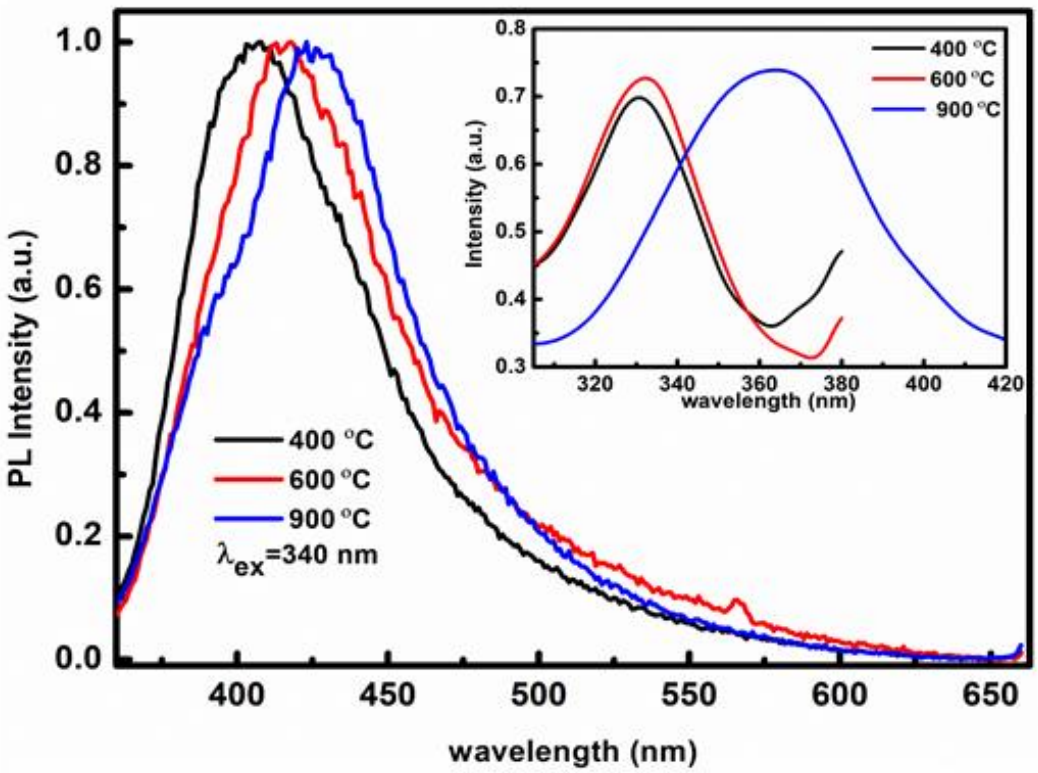

Figure 3.10. PL spectra and PL-excitation spectra (instead Fig.) of TiO_2 NPs produced at different temperatures. The excitation wavelength was 340 nm and PL-excitation spectra were monitored at the peak of the PL band.

In contrast, the value of 52 nm reflects the direct bandgap of the rutile phase. The significant PL is originated from the recombination of the conduction band electron with trapped holes. For all three structures, only a single PL band maximum is observed. On the other hand, multiple PL bands were also noticed while prepared at similar annealing temperatures [46].

3.5 Photocatalytic activity of different phases of TiO_2 NPs

The photocatalytic activity of all the three NPs structures was examined by considering one of the commonly used laser dyes, Rhodamine B (RhB); the obtained results are demonstrated in Figure 3.11. TiO_2 NPs were used to degrade Rhodamine B (RhB) dissolved

in an aqueous solution in the presence of UV radiation. During the process, the anatase phase of TiO_2 NPs (~ 25 mg) was dispersed in a 25 ml aqueous solution of RhB (Conc. 6×10^{-6} M) in a beaker and the mixture was continuously stirred for 60 min under dark conditions to bring equilibrium condition following the adsorption-desorption process.

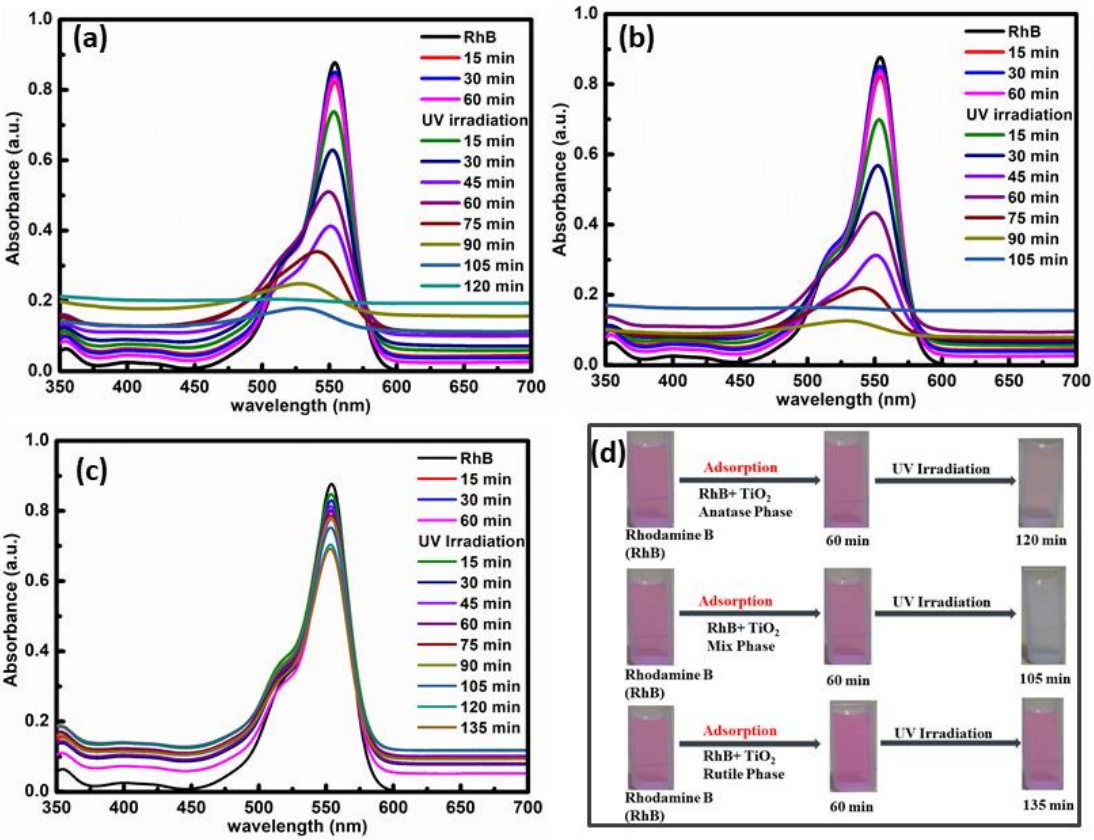

Figure 3.11. Absorption spectra of RhB solution in the presence of (a) anatase (b) mixed and (c) rutile phases of TiO_2 NPs upon UV irradiation. (d) Digital photographs of the RhB solution upon photoirradiation in the presence of NPs.

After that, a 4 mL sample was taken out and centrifuged at 5000 rpm for 3 min to remove the catalyst from the solution to maintain the concentration of the RhB in the solution. The relative concentration of RhB in the solution was determined by comparing its absorption maximum (at 554 nm) and PL spectrum obtained for the initial solution (Figs. 3.11-3.13). The photodegradation rate of the sample solution with RhB was very low without photo-irradiation. After that, the sample solution was irradiated with a UV lamp of

8 watts, 254 nm, 1.2 mW/cm^2. The degradation of RhB dye started upon photoirradiation, as illustrated in Fig. 10a. Similar experiments were carried out for mixed and rutile phases of TiO_2 NPs, and the results are quite different (Fig. 3.11b, c). When the mixed phase of TiO_2 NPs was chosen as a photocatalyst, the degradation of RhB became faster and degraded the dye entirely within 105 minutes (Fig. 3.11b), which was not observed while using the anatase phase.

On the other hand, the rutile phase of TiO_2 NPs containing RhB solution remains unaffected upon photoirradiation, i.e., there are no such photodegrading effects observed for the rutile phase of TiO_2 (Fig. 3.11c). The images of a different phase of TiO_2 containing RhB solution with and without photoirradiation are shown in Figure 3.11d. The images clearly show that the maximum effect was observed when the mixed phase of NPs is used for the degradation. The reaction rate constant ***k*** is calculated by relation ln $(C/C_0) = -kt$, where C is the concentration at time ***t***, C_0 is the initial concentration of RhB solution and ***t*** is the reaction time, respectively. The kinetics plots between $\ln(C/C_0)$ and irradiation time for the photocatalysts are nearly linear (Fig. 3.12), demonstrating that the RhB degraded by TiO_2 following photoirradiation and also followed pseudo-first-order kinetics [47]. However, the slop is different for different phases of NPs (Fig. 3.12a), maximum for mix phase of TiO_2 NPs hence, has the maximum rate constant and is about 0.0208 min^{-1} as shown in Figure 3.12(b) and smaller for other phases of NPs.

Here, it has to be mentioned that a specific phase of TiO_2 NPs was investigated, which shows prominent photocatalytic activity for the photodegradation of dyes. Thus, the mixed-phase of TiO_2 NPs can be used to degrade harmful dyes used in industries and laboratories. The mixed-phase of TiO_2 NPs possesses the best photocatalytic activity out of three phases because the recombination of photogeneration electron-hole pairs boosts the

photocatalytic activity. On the contrary, the rutile phase produced at 900 °C leads to poor photocatalytic activity.

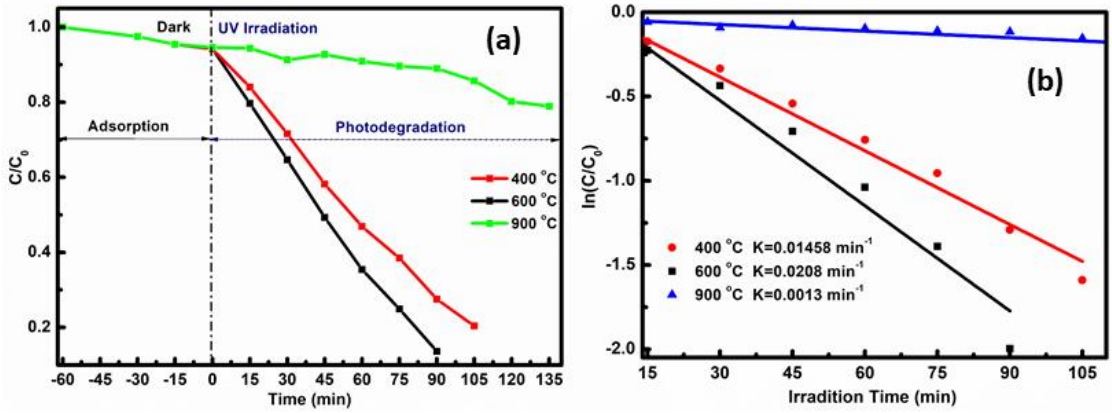

Figure 3.12. Plots of concentration ratio C/C_0 of RhB in presence and absence of different TiO_2 NPs as a function of time (a) and first-order reaction rate constants *k* against reaction time of different TiO_2 NPs used as photocatalysts (b).

Furthermore, the degradation of the RhB dye was also examined by measuring the PL of the dye solution containing different phases of TiO_2 NPs with photoirradiation. The PL intensity was measured in the same experimental conditions as used for the absorption. A very similar result was observed with photoirradiation. Note the measurement time of each spectrum is less than one minute; hence during the measurement, the irradiation effect with excitation energy was ignored, keeping the silt width 1.0 nm both for excitation and emission.

The PL intensity of the anatase and mixed-phase is diminished (Fig. 3.13a,b). In contrast, there is negligible change in PL intensity for the rutile phase of NPs (Fig. 3.13c) and the trend is similar to that observed for the absorption. In mixed-phase, a small band originates at a shorter wavelength region upon photoirradiation; however, we cannot comment on it at present. The rate of degradation is plotted as a function of time and is shown in Figure 3.13d.

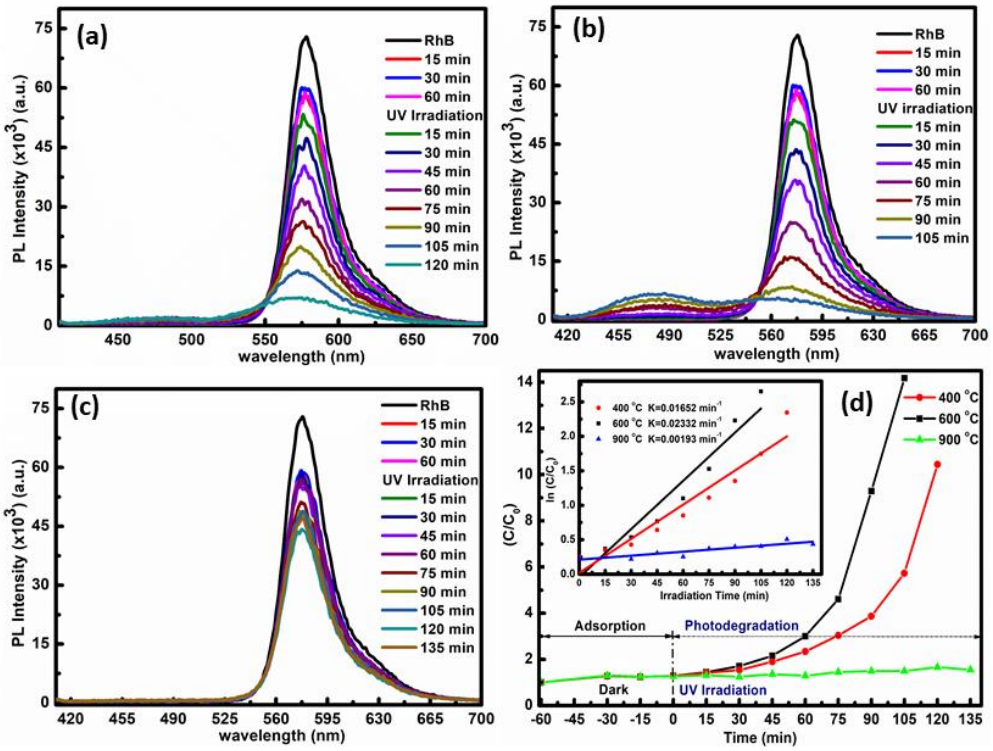

Figure 3.13. PL spectra of RhB solution in the presence of (a) anatase (b) mixed and (c) rutile phases of TiO_2 NPs upon UV irradiation, (d) plots of photocatalytic degradation of RhB in the presence of TiO_2 NPs as a function of time and first-order reaction rate constants *k* against reaction time for different TiO_2 NPs photocatalysts (inset plots).

The valence bands are composed of O 2p and some Ti 3d states, indicating the p–d hybridizations between O 2p and Ti 3d orbitals. This type of hybridization exists within the valence band, also known as the bonding state. These hybridizations are responsible for broadening the valence band, thereby promoting the transfer of photogenerated holes. In addition to this, the conduction band is composed by Ti 3d states, mixed with some O 2p and Ti 3p states. In this case, the hybridization between Ti 3d and O 2p orbitals formed antibonding states [46,48]. The average effective masses of electron and hole in anatase structure are smaller than that of rutile structure, which sustained the migration of the photogenerated electron-hole (e-h) pairs (charge carriers) and shows higher photocatalytic activity. The same may be true for the mixed phase of TiO_2. Upon photoirradiation, e-h

pairs are generated between the ground state, the valence band (VB) and excited state, the conduction band (CB).

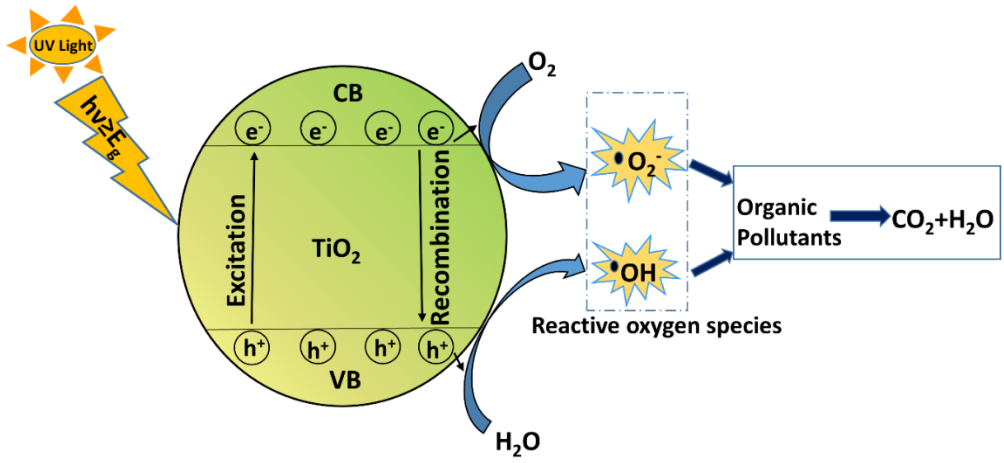

Figure 3.14. The schematic diagram of TiO_2 NPs photocatalytic activity under UV irradiation.

Then the photogenerated electrons and holes take part in the photocatalytic degradation of RhB molecules (Fig. 3.14). When incident light of energy is equal or greater than the bandgap of the NPs, an electron-hole pair is generated. Subsequently, the excited electrons combined with oxygen (O_2) to form super-oxygen ions ($.O_2^-$) and the holes generated in the valence band combine with hydroxyl ions (OH^-) to form hydroxyl radicals (.OH) [49,50]. These typically reactive oxygen species/radicals degrade RhB molecules into smaller hydrocarbons and finally to CO_2 and H_2O [51].

3.6 Conclusions

TiO_2 NPs were developed by considering a low-temperature synthesis route to be employed in environmental applications. The TiO_2 nanoparticles were formed through the facile sol-gel technique followed by annealing at three different temperatures, i.e., 400, 600 and 900 °C. As a result, three different crystal structures of TiO_2 NPs were formed. The change in the annealing temperature from 400-900 °C leads to the phase transformation of TiO_2 NPs from the anatase to mixed and rutile phase. The structural changes occurred during the

phase transformation from anatase to rutile. The particle size of the TiO_2 NPs was increased, the expansion in the grain boundaries occurred, and the different morphologies were noticed for three distinct phases. The estimated crystallite size for anatase, mixed and rutile phases of TiO_2 NPs are 21, 36 and 54 nm, respectively. The indirect bandgap structure changed into the direct bandgap during the structural transformation. Both absorption and PL spectra shifted towards lower energy regions, which might be due to the increase in size or the induced oxygen vacancies produced at a higher temperature. Furthermore, it is to be mentioned that out of three different structures used for photocatalytic activity, the mixed-phase of TiO_2 NPs is most efficient for the degradation of dye (RhB) under UV irradiation. On the other hand, the rutile phase TiO_2 NPs has nearly negligible photocatalytic activity.

References

[1] D. A. H. Hanaor, C. C. Sorrell, Review of the anatase to rutile phase transformation, J. Mater. Sci. 46 (2011) 855–874.

[2] H. Nakano, N. Hasuike, K. Kisoda, K. Nishio, T. Isshiki, H. Harima, Synthesis of TiO_2 nanocrystals controlled by means of the size of magnetic elements, J. Phys.: Condens. Matter. 21 (2009) 064214.

[3] Y. Xing, X. Li, L. Zhang, Q. Xu, Z. Che, W. Li, Y. Bai, K. Li, Effect of TiO_2 nanoparticles on the antibacterial and physical properties of polyethylene-based film, Prog. Org. Coat. 73 (2012) 219–224.

[4] Y. S. Kim, L. T. Linh, E. S. Park, S. Chin, G. Bae, J. Jurng, Antibacterial performance of TiO_2 ultra fine nanopowder synthesized by a chemical vapor condensation method : Effect of synthesis temperature and precursor vapor concentration, Powder Technol. 215–216 (2012) 195–199.

[5] N. Pourreza, S. Rastegarzadeh, A. Larki, Micelle-mediated cloud point extraction and spectrophotometric determination of rhodamine B using Triton X-100, Talanta 77 (2008) 733–736.

[6] M. Beija, C. A. M. Afonso, J. M. G. Martinho, Synthesis and applications of Rhodamine derivatives as fluorescent probes, Chem. Soc. Rev. 38 (2009) 2410–2433.

[7] D. S. Kim, S. J. Han, S. Kwak, Synthesis and photocatalytic activity of mesoporous TiO_2 with the surface area, crystallite size, and pore size, J. Colloid and Interface Sci. 316 (2007) 85–91.

[8] K. K. Akurati, A. Vital, G. Fortunato, R. Hany, F. Nueesch, T. Graule, Flame synthesis of TiO_2 nanoparticles with high photocatalytic activity, Solid State Sci. 9 (2007) 247–257.

[9] Y. Sakatani, D. Grosso, L. Nicole, Optimised photocatalytic activity of grid-like mesoporous TiO_2 films : effect of crystallinity, pore size distribution, and pore accessibility, J. Mater. Chem. 33 (2006) 1–6.

[10] S. Sakthivel, H. Kisch, Daylight Photocatalysis by Carbon-Modified Titanium Dioxide, Angew. Chem. Int. Ed. 42 (2003) 4908–4911.

[11] C. Lettmann, K. Hildenbrand, H. Kisch, W. Macyk, W. F. Maier, Visible light photodegradation of 4-chlorophenol with a coke-containing titanium dioxide photocatalyst, Appl. Catal. B 32 (2001) 215–227.

[12] N. Godbout, D. R. Salahub, J. Andzelm, E. Wimmer, Optimization of Gaussian-type basis sets for local spin density functional calculations. Part I. Boron through neon, optimization technique and validation, Can. J. Chem. 70 (1992) 560–571.

[13] T. H. Wang, Z. Fang, N. W. Gist, S. Li, D. A. Dixon, J. L. Gole, Computational Study of the Hydrolysis Reactions of the Ground and First Excited Triplet States of Small TiO_2 Nanoclusters, J. Phys. Chem. C. 115 (2011) 9344–9360.

[14] X. Chen, C. Burda, Photoelectron spectroscopic investigation of nitrogen-doped titania nanoparticles, J. Phys. Chem. B. 108 (2004) 15446–15449.

[15] T. Mikulas, Z. Fang, J. L. Gole, M. G. White, D. A. Dixon, The presence of Ti(II) centers in doped nanoscale TiO_2 and $TiO_{2-x}N_x$, Chem. Phys. Lett. 539–540 (2012) 58–63.

[16] B. H. K. Kammler, L. Madler, S. E. Pratsinis, Flame Synthesis of Nanoparticles, Chem. Eng. Technol. 24 (2001) 583–596.

[17] J. Shi, X. Wang, Growth of Rutile Titanium Dioxide Nanowires by Pulsed Chemical Vapor Deposition, Cryst. Growth Des. 11 (2011) 949–954.

[18] S. Mahshid, M. Askari, M. S. Ghamsari, Synthesis of TiO_2 nanoparticles by hydrolysis and peptization of titanium isopropoxide solution, J. Mater. Process.

Technol. 189 (2007) 296–300

[19] S. Sugapriya, R. Sriram, S. Lakshmi, Effect of annealing on TiO_2 nanoparticles, Optik 124 (2013) 4971–4975.

[20] M. Arin, P. Lommens, S. C. Hopkins, G. Pollefeyt, Deposition of photocatalytically active TiO_2 films by inkjet printing of TiO_2 nanoparticle suspensions obtained from microwave-assisted hydrothermal synthesis, Nanotechnology 23 (2012) 165603.

[21] S. Vyas, R. Tiwary, K. Shubham, P. Chakrabarti, Study the target effect on the structural, surface and optical properties of TiO_2 thin film fabricated by RF sputtering method, Superlattices Microstruct. 80 (2015) 215–221.

[22] Y. Tanaka, T. Tsuke, W. Guo, Y. Uesugi, T. Ishijima, S. Watanabey, K. Nakamura, A large amount synthesis of nanopowder using modulated induction thermal plasmas synchronized with intermittent feeding of raw materials, J. Phys: Conf. Ser. 406 (2012) 012001

[23] T. Corrales, C. Peinado, N. S. Allen, M. Edge, G. Sandoval, F. Catalina, A chemiluminescence study of micron and nanoparticle titanium dioxide : effect on the thermal stability of metallocene polyethylene, J. Photochem. Photobiol. A 156 (2003) 151–160.

[24] R. K. Ratnesh, M. S. Mehata, Tunable single and double emission semiconductor nanocrystal quantum dots : a multianalyte sensor, Methods Appl. Fluoresc. 6 (2018) 35006.

[25] R. K. Ratnesh, M. S. Mehata, Investigation of biocompatible and protein sensitive highly luminescent quantum dots/nanocrystals of CdSe, CdSe/ZnS and CdSe/CdS, Spectrochim. Acta Part A Mol. Biomol. Spectrosc. 179 (2017) 201–210.

[26] M.K. Singh, M.S. Mehata, Phase-dependent optical and photocatalytic performance of synthesized titanium dioxide (TiO_2) nanoparticles, Optik 193 (2019) 163011.

[27] K.P. Biju, M. K. Jain, Effect of crystallization on humidity sensing properties of sol-gel derived nanocrystalline TiO_2 thin films, Thin Solid Films 516 (2008) 2175–2180.

[28] A. Verma, A. K. Bakhshi, S. A. Agnihotry, Effect of different precursor sols on the properties of CeO_2 – TiO_2 films for electrochromic window applications, Electrochim. Acta 51 (2006) 4639–4648.

[29] R. P. Hernandez, D. M. Anaya, M. E. Fernandez, A. G. Cortes, Synthesis of mixed ZrO_2 – TiO_2 oxides by sol-gel : Microstructural characterization and infrared spectroscopy studies of NO_x, J. Mol. Catal. A: Chem. 281 (2008) 200–206.

[30] H. Bensouyad, H. Sedrati, H. Dehdouh, M. Brahimi, F. Abbas, H. Akkari, Structural, thermal and optical characterization of TiO_2 : ZrO_2 thin films prepared by sol-gel method, Thin Solid Films 519 (2010) 96-100.

[31] A. Patterson, The Scherrer Formula for X-Ray Particle Size Determination, Phys. Rev. 56 (1939) 978.

[32] D. J. Kim, S. H. Hahn, S. H. Oh, E. J. Kim, Influence of calcination temperature on structural and optical properties of TiO_2 thin films prepared by sol-gel dip coating, Mater. Lett. 57 (2002) 355–360.

[33] Y. Yu, X. Yin, A. Kvit, X. Wang, Evolution of Hollow TiO_2 Nanostructures via the Kirkendall Effect Driven by Cation Exchange with Enhanced Photoelectrochemical Performance, Nano Lett. 14 (2014) 2528−2535.

[34] J. Wei, L. Zhao, S. Peng, J. Shi, Z. Liu, W. Wen, Wettability of urea-doped TiO_2 nanoparticles and their high electrorheological effects, J. Sol-Gel Sci. Technol. 47 (2008) 311–315.

[35] A. Kathiravan, R. Renganathan, Photosensitization of colloidal TiO_2 nanoparticles with phycocyanin pigment, J. Colloid Interface Sci. 335 (2009) 196–202.

[36] H. Bin Lu, Y.Z. Zhou, S. Vongehr, S. C. Tang, X.K. Meng, Effects of hydrothermal

temperature on formation and decoloration characteristics of anatase TiO_2 nanoparticles, Sci. China Technol. Sci. 55 (2012) 894–902.

[37] X. Lu, X. Lv, Z. Sun, Y. Zheng, Nanocomposites of poly(l-lactide) and surface-grafted TiO_2 nanoparticles: Synthesis and characterization, Eur. Polym. J. 44 (2008) 2476–2481.

[38] T. Ohsaka, F. Izumi, Y. Fujiki, Raman Spectrum of Anatase, TiO_2, J. Raman Spectrosc. 7 (1978) 321–324.

[39] S. P. S. Porto, P. A. Fleury, T. C. Damen, Raman Spectra of TiO_2, MgF_2, ZnF_2, FeF_2, and MnF_2, Phys. Rev. 154 (1967) 522-526.

[40] H. L. Ma, J. Y. Yang, Y. Dai, Y. B. Zhang, B. Lu, G. H. Ma, Raman study of phase transformation of TiO_2 rutile single crystal irradiated by infrared femtosecond laser, Appl. Surf. Sci. 253 (2007) 7497–7500.

[41] S. S. Abdullahi, S. Guner, Y. Koseoglu, I. M. Musa, B. I. Adamu M. I. Abdulhamid, Simple Method For The Determination of Band Gap of a Nanopowdered Sample Using Kubelka Munk Theory, J. Nigerian Assoc. Math. Phys. 35 (2016) 241-246.

[42] V. S. Kirankumar, S. Sumathi, Structural, optical, magnetic and photocatalytic properties of bismuth doped copper aluminate nanoparticles, Mater. Chem. Phys. 197 (2017) 17–26.

[43] E. A. Davis, N. F. Mott, Conduction in non-crystalline systems V. Conductivity, optical absorption and photoconductivity in amorphous semiconductors, Philosophical Magazine 22 (1970) 903-922.

(i) [44] R. K. Ratnesh, M. S. Mehata, Controlled synthesis and optical properties of tunable CdSe quantum dots and effect of pH, AIP Advances 5 (2015) 097114.

[45] S. Valencia, J. M. Marin, G. Restrepo, Study of the Bandgap of Synthesized Titanium Dioxide Nanoparticles Using the Sol-Gel Method and a Hydrothermal

Treatment, Open Mater. Sci. J. 4 (2010) 9-14.

[46] J. Zhang, P. Zhou, J. Liu, J. Yu, New understanding of the difference of photocatalytic activity among anatase, rutile and brookite TiO_2, Phys.Chem.Chem.Phys 16 (2014) 20382-20386.

[47] X. Zhu, L. Pei, R. Zhu, Y. Jiao, R. Tang, W. Feng, Preparation and characterization of Sn/La co-doped TiO_2 nanomaterials and their phase transformation and photocatalytic activity, Sci. Rep. 8 (2018) 1–14.

[48] D. K. Pallotti, L. Passoni, P. Maddalena, F. D. Fonzo, S. Lettieri, Photoluminescence Mechanisms in Anatase and Rutile TiO_2, J. Phys. Chem. C 121 (2017) 9011 − 9021.

[49] T. Wang, J. Wei, H. Shi, M. Zhou, Y. Zhang, Q. Chen, Z. Zhang, Preparation of electrospun Ag/TiO_2 nanotubes with enhanced photocatalytic activity based on water/oil phase separation, Phys. E Low-Dimensional Syst. Nanostructures. 86 (2017) 103–110.

[50] A. Kadam, R. Dhabbe, D. Shin, K. Garadkar, J. Park, Sunlight driven high photocatalytic activity of Sn doped N-TiO_2 nanoparticles synthesized by a microwave assisted method, Ceram. Int. 43 (2017) 5164–5172.

[51] P. Khare, A. Singh, S. Verma, A. Bhati, Sunlight-Induced Selective Photocatalytic Degradation of Methylene Blue in Bacterial Culture by Pollutant Soot Derived Nontoxic Graphene Nanosheets, ACS Sustain. Chem. Eng. 6 (2017) 579-589.

Chapter-4

Photoinduced catalytic activity of metal ions incorporated TiO_2 nanoparticles*

4.1 Introduction

A large number of synthetic dyes have been produced and used in various industries worldwide. The trace concentration of dye in effluent streams has a major risk to animals, plants, the atmosphere, and human health because of their highly toxic and non-biodegradable nature [1,2]. Thus, the removal of these hazardous dyes from wastewater is considered to be a significant environmental concern. Numerous methods, such as coagulation, adsorption, biodegradation, and membrane removal, have been suggested for their elimination. However, the heterogeneous photocatalysis method has become the most favorable option for degrading hazardous organic dyes and their decomposition to carbon dioxide and harmless byproducts [3–5].

Titanium dioxide (titania/TiO_2) has been widely used in various applications, such as dye synthesized solar cells, sensors, pigments, photocatalysts, and daily use products [6–10]. TiO_2 is one of the most studied semiconductor materials because of its low toxicity, better electrochemical properties, high chemical stability, and high photocatalytic efficiency. Primarily, TiO_2 has two polymorphic phases, rutile and anatase, with an optical band gap of 3.0 eV and 3.2 eV, respectively [11]. TiO_2 acts as a promising photocatalyst in the presence of ultraviolet (UV) light but not in visible light due to the larger optical bandgap. The solar spectrum consists of only 3-5% UV radiation, which can be utilized to stimulate

*Content of this chapter have been published in **Optical Materials 109 (2020) 110309.**

the valance band (VB) electrons (e^-) of TiO_2 and transfer them into the conduction band (CB). Furthermore, the transferred CB electrons (e^-) and correspondingly formed VB holes (h^+) transfer to the surface of the photocatalysts, which react with adsorbed oxygen and water species to initiate the oxidation and reduction process. In the oxidation state, the VB holes react with [H_2O] and [$OH]^-$ and produce the hydroxyl radicals (•OH) [12]. On the other hand, in a reduction state, the valance band electrons react with dissolved oxygen and create superoxide radicals ($•O_2^-$). These free radicals (•OH and $•O_2^-$) take part in the photooxidation process of the organic species, and these organic molecules are converted into stable compounds [13].

The efficiency of photocatalytic reaction increases with increasing lifetime, that is, the recombination time of electron-hole (*e-h*) in TiO_2 nanoparticles (NPs). Doping by metallic and non-metallic ions in TiO_2 NPs not only enhances the photocatalytic properties but also increasing the number of defects and vacancies that may alter various other features, which could be helpful for different applications. This also accelerates both the removal of CB electrons from particles and their reaction with oxygen [14]. In pristine TiO_2, the surface electron undergoes a fast recombination process, *i.e.*, the recombination rate of *e-h* is slower in doped TiO_2 [15]. Thus, the doping of metal ions in the TiO_2 particles slows down the *e-h* pair recombination rate and improves the efficacy of the photocatalytic reaction.

In the present work, various metal ions (Ag^+, Cu^{2+}, Ni^{2+}) doped TiO_2 NPs have been prepared via the sol-gel process. Acquired NPs were characterized by multiple techniques to examine their structure and morphology. These synthesized NPs were then used to degrade the dye, cationic methylene blue, and found to exhibit efficient photocatalytic activities [16].

4.2 Materials and Methods

All the solvents and chemicals were analytical grade and used without further purification. Titanium (IV) isopropoxide (TTIP, $C_{12}H_{28}O_4Ti$, 97%, Alfa sear), absolute ethanol (C_2H_5OH, analytical grade), iso-propyl alcohol (IPA, $(CH_3)_2CHOH$, 99%, assay), hydrochloric acid (HCl, Thomas Baker), nickel perchlorate hexahydrate ($Ni(ClO_4)_2.6H_2O$, Alfa Asear), silver nitrate ($AgNO_3$, Acros), copper perchlorate hexahydrate ($Cu(ClO_4)_2.6H_2O$, 98%, Sigma Aldrich), methylene blue ($C_{16}H_{18}ClN_3S$, CDH) have been used as raw materials. Deionized (DI) water having specific resistivity 18.2 MΩ×cm was used as a dispersive medium in the experiment.

The synthesis process of undoped TiO_2 NPs has been reported previously [7]. To prepare the metal-doped of TiO_2 NPs, the titanium isopropoxide (0.05 M) was added dropwise in a solution of IPA and DI water. After stirring for 15 minutes, 1.0 wt% of different metal dopants were added.

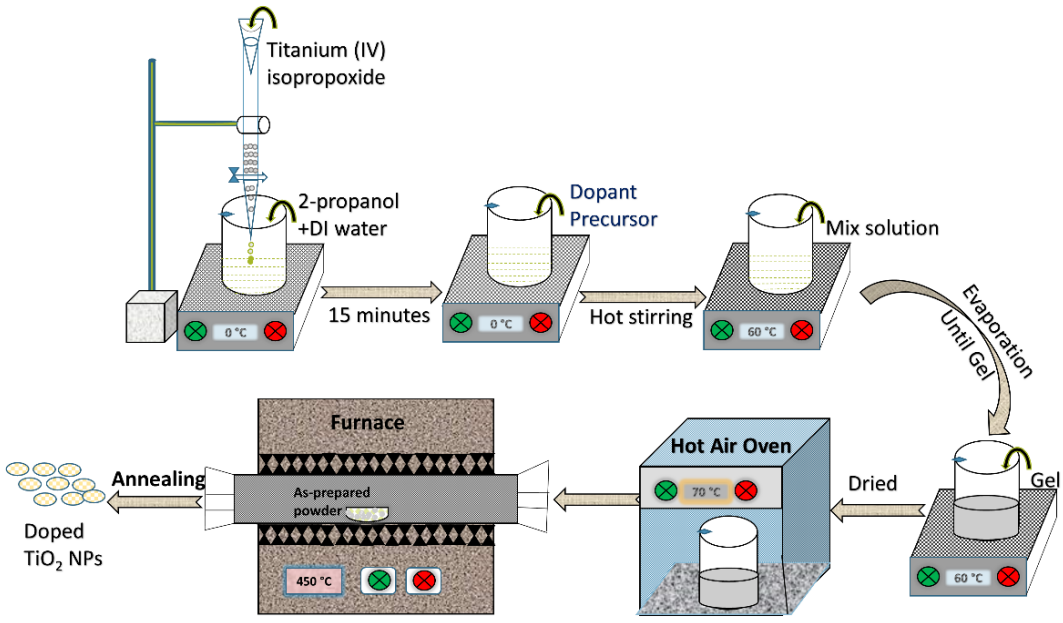

Figure 4.1. Schematic representation of the synthesis route of metal-doped TiO_2 NPs.

The pH of the solution was maintained by the dropwise addition of HCl with continuous stirring for 12h at 60 °C. After 24h of aging, gelation occurred and was followed

by drying in a hot air oven at 70 ℃ and washing three times with ethanol to obtain the final powdered sample. Further, the powder was dried overnight in an oven and calcined in air at 450 ℃ resulting in the desired doped TiO_2 nanostructures. The schematic representation of the synthesis of metal-doped titania nanoparticles is shown in Fig. 4.1.

4.3 Characterization Techniques

The diffraction patterns of undoped and doped TiO_2 NPs were obtained from X-ray diffractometer (XRD), Brukar 8D advance system having CuKα (λ~1.54 Å) source of radiation with a supply of 40 kV voltage and 20 mA current. The morphological and elemental analysis of undoped and doped TiO_2 NPs was done using field emission scanning electron microscopy (FE-SEM) and Energy-dispersive X-ray spectroscopy (EDS, Gemini electron-optics), respectively. High-resolution transmission electron microscopy (HRTEM) micrographs were obtained from HRTEM, TALOS at an accelerating voltage of 200 kV. Fourier transform infrared spectroscopy (FT-IR) spectra were recorded from spectrum two FTIR spectrometers (Perkin Elmer). The plot of UV-vis absorption intensity as a function of wavelength was recorded with a dual-beam spectrophotometer (Perkin Elmer, lambda 750). The photoluminescence (PL) and excitation spectra were recorded on a spectrofluorometer (Horiba Jobin Yvon, Fluorolog-3) equipped with a 450 W xenon lamp and double monochromators at each excitation and emission part [17,18]. The PL decay profiles were recorded with the time-correlated single-photon counting (TCSPC) arrangement (DeltaFlex-01-DD, Horiba Jobin Yvon IBH Ltd.) equipped with PMT (PPD 850) and Delta Diode of 300 nm and has a repetition rate of 10 MHz. To analyze the PL decays curves, the least square fitting and re-convolution methods were used. The total number of counts was kept at 10,000 in the peak channel. The instrument response function was taken by Ludox scatterer. The Cole-Parmer UV lamp was used as an irradiation source,

having a wavelength of 254 and 365 nm, 8-watt power, and their intensity is 1200 and 900 $\mu W/cm^2$, respectively.

4.4 Results and discussion

The XRD patterns of 1 wt% different transition metal ions doped and undoped TiO_2 NPs are shown in Figure 4.2(a), which demonstrated that all the samples exhibit anatase phase of TiO_2 with diffraction peaks at Braggs angles of 25.44° (101), 38.80° (004), 48.08° (200),

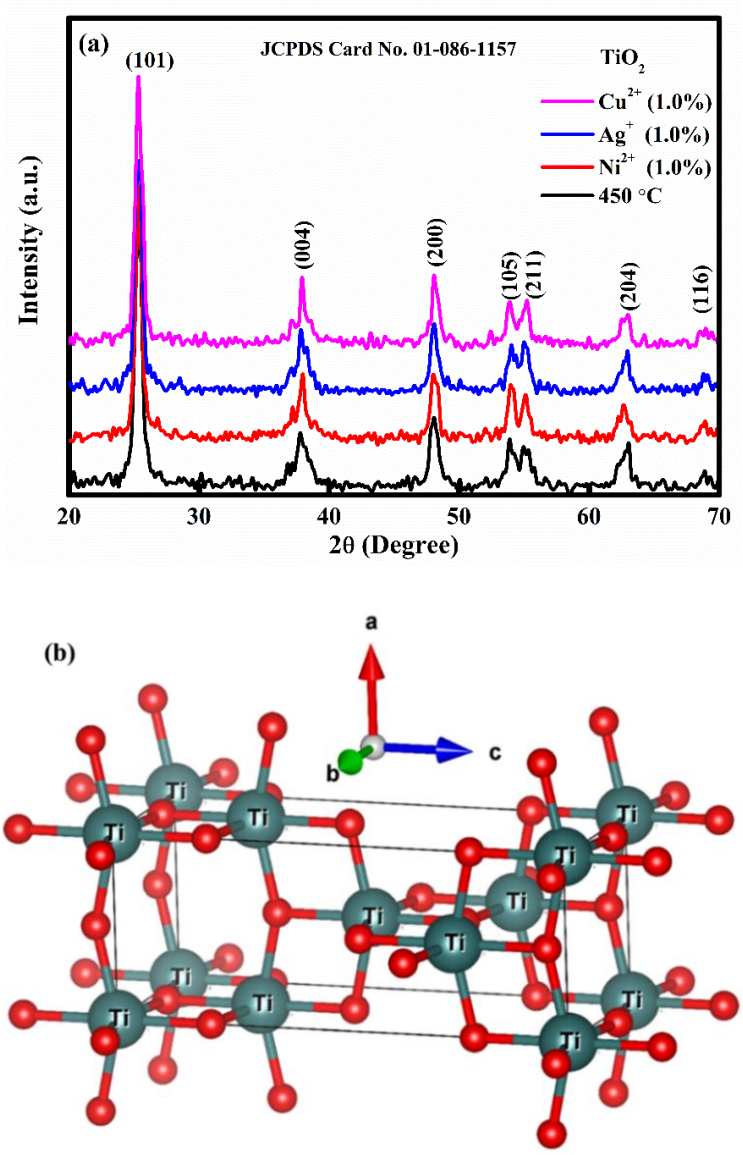

Figure 4.2. XRD patterns of undoped and metal-doped TiO_2 NPs (a) and the tetragonal crystal structure of anatase phase of TiO_2 NPs (b).

53.88° (105), 55.12° (211), 63.04° (204) and 68.88° (116). No characteristic peaks corresponding to the dopant metal ions were present in the diffraction patterns, indicating that metal ions may be present in the TiO_2 host matrix [19,20]. The average crystallite size of the samples is calculated by using Scherrer's equation, and the resultant sizes are 18, 22, 27, and 30 nm for Cu^{2+}, Ni^{2+}, Ag^{+} metal ions doped titania and pristine TiO_2, respectively. The metal-doped synthesized TiO_2 exhibits an anatase phase (JCPDS Card No. 01-086-1157) with a tetragonal crystal structure, as demonstrated in Fig. 4.2(b).

The FESEM micrographs together with the EDS spectra of undoped and metal ions doped TiO_2 NPs developed at a calcinated temperature of 450 °C are given in Fig. 4.3(a-d).

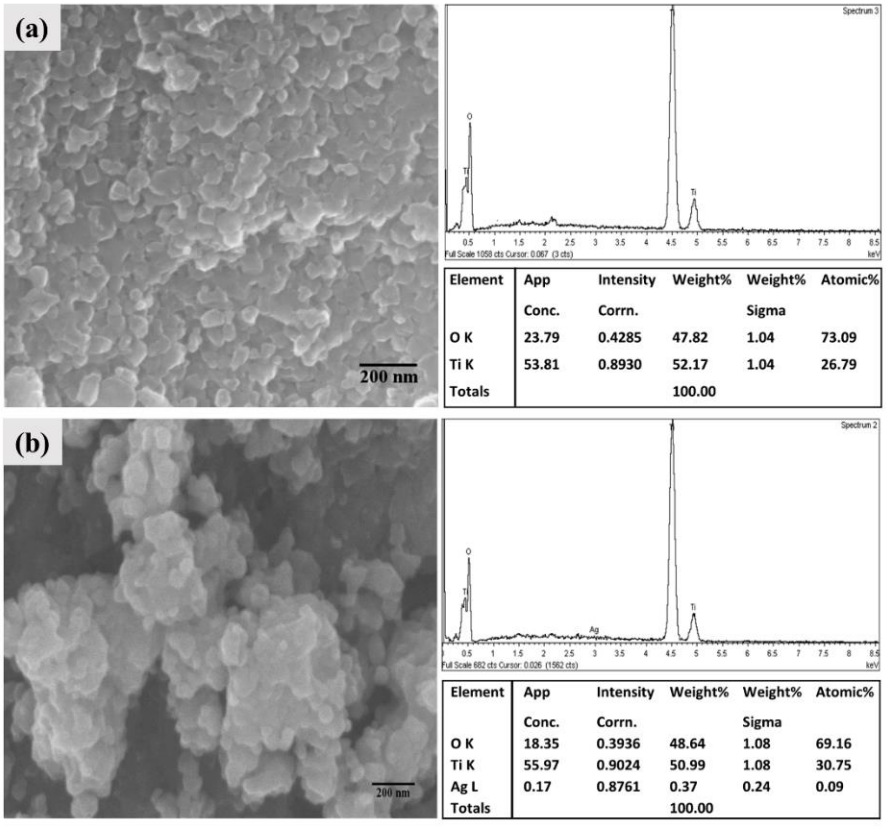

Element	App Conc.	Intensity Corrn.	Weight%	Weight% Sigma	Atomic%
O K	23.79	0.4285	47.82	1.04	73.09
Ti K	53.81	0.8930	52.17	1.04	26.79
Totals			100.00		

Element	App Conc.	Intensity Corrn.	Weight%	Weight% Sigma	Atomic%
O K	18.35	0.3936	48.64	1.08	69.16
Ti K	55.97	0.9024	50.99	1.08	30.75
Ag L	0.17	0.8761	0.37	0.24	0.09
Totals			100.00		

Figure 4.3. FESEM images together with EDS of undoped (a), Ag^{+}-doped (b) of TiO_2 NPs. It was observed that the doped sample particles were agglomerated into irregular morphology, but the Cu^{2+} doped sample displayed some uniformity compared to others.

The average particle size was in the range of 15 to 30 nm. The smaller particles can promote surface contact between dye molecules and photocatalyst, thus improving the performance of photocatalytic activity.

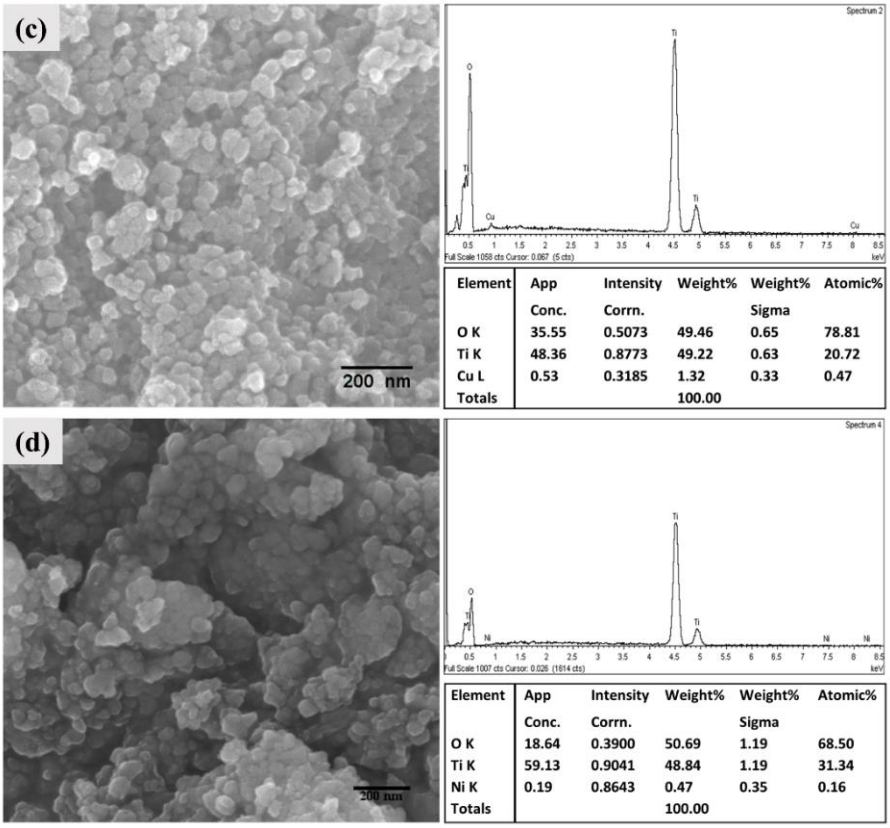

Element	App Conc.	Intensity Corrn.	Weight%	Weight% Sigma	Atomic%
O K	35.55	0.5073	49.46	0.65	78.81
Ti K	48.36	0.8773	49.22	0.63	20.72
Cu L	0.53	0.3185	1.32	0.33	0.47
Totals			100.00		

Element	App Conc.	Intensity Corrn.	Weight%	Weight% Sigma	Atomic%
O K	18.64	0.3900	50.69	1.19	68.50
Ti K	59.13	0.9041	48.84	1.19	31.34
Ni K	0.19	0.8643	0.47	0.35	0.16
Totals			100.00		

Figure 4.3. FESEM images together with EDS of Cu^{2+}-doped (c) and Ni^{2+}-doped (d) of TiO_2 NPs.

The elemental composition of transition metal ions (1% of Ag^{+}, Cu^{2+}, and Ni^{2+}) doped TiO_2 samples obtained from the EDS measurement are also shown in Figure 4.3(a-d). The EDS analysis (right panel of Fig. 4.3) clearly shows the composition of Ti, O, Ag, Cu, and Ni in the doped TiO_2 NPs.

Figure 4.4 demonstrated the HRTEM images of undoped and metal ions doped TiO_2 NPs were crystalline. Supporting the FESEM data, HRTEM also confirmed that the undoped TiO_2 NPs were in the range of 10 to 20 nm and exhibits a non-spherical shape

(Fig. 4.4a). The lattice spacing of 0.36 ± 0.02 nm specifies the (101) plane of the anatase phase (Fig. 4.4b).

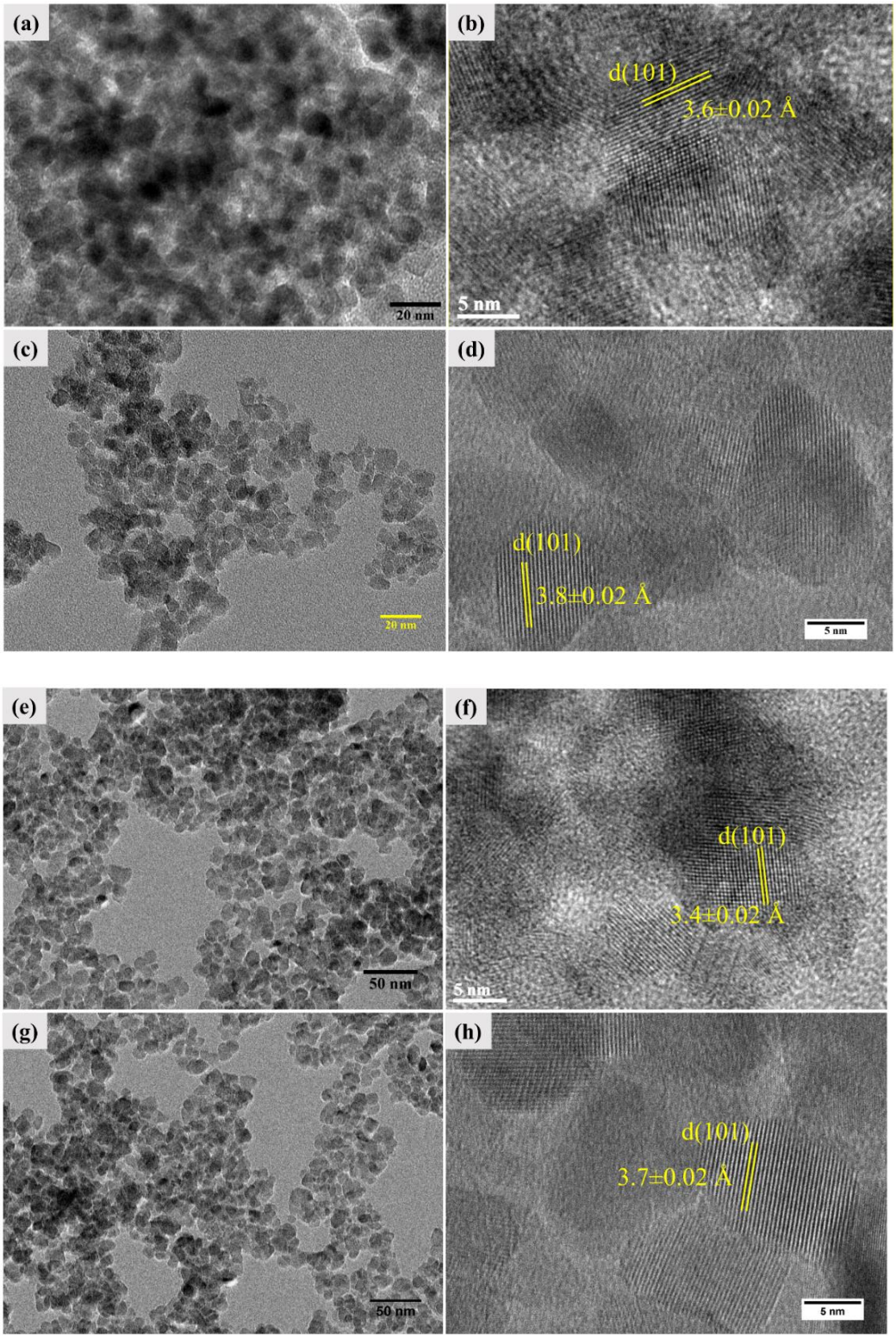

Figure 4.4. The HRTEM images of undoped (a,b) Ag^{+}-doped (c,d), Cu^{2+}-doped (e,f) and Ni^{2+}-doped (g,h) of TiO_2 NPs.

No significant morphological changes were observed for doped samples (Fig. 4.4 c,e and g). Figure 4.4 (d, f and h) depicts the lattice spacing 0.38 ± 0.02, 0.34 ± 0.02 and 0.37 ± 0.02 nm corresponding to the (101) plane.

Figure 4.5 illustrates the FTIR spectra of undoped and metals doped TiO_2 NPs in the 500 - 4000 cm^{-1} range. The bands at 3305 and 1634 cm^{-1} were assigned to the stretching and bending modes of vibrations of the hydroxyl group (–OH or O–H bond), respectively. This arises due to the presence of absorbed water molecules or moisture in samples [7,21]. In each of the samples, the strong broadband in between 400 to 1000 cm^{-1} region is associated with the Ti–O–Ti, Ti-O, R–O–Ti and R–O (where R= Ag, Cu, and Ni) bridging stretching and stretching modes [22–24].

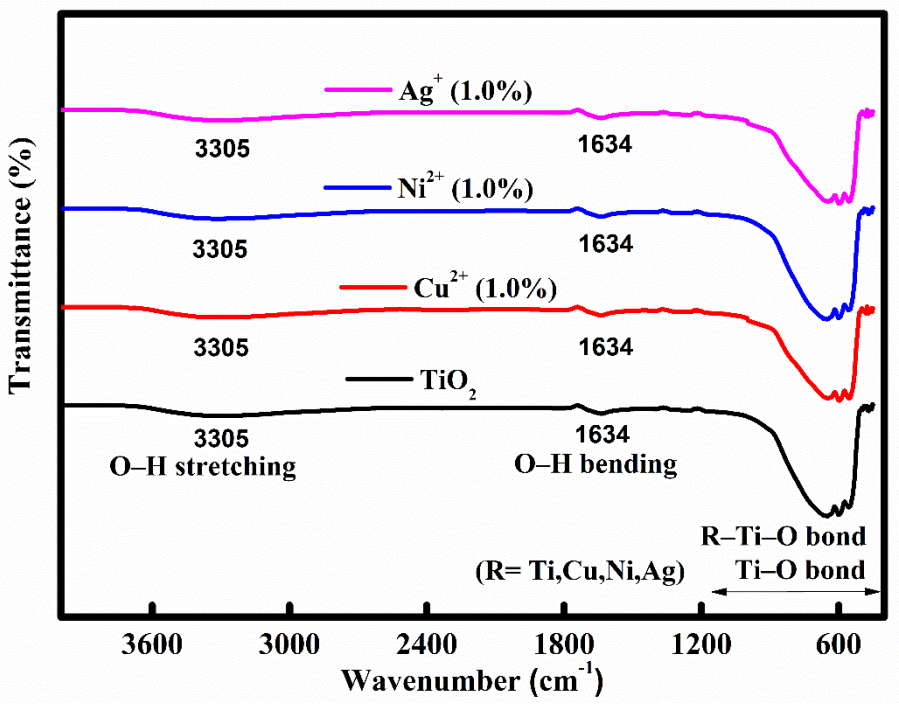

Figure 4.5. FTIR spectra of TiO_2 NPs doped with various transition metal ions.

The UV-vis reflectance and absorption spectra of undoped and metal ions doped TiO_2 NPs are presented in Figure 4.6(a,b). The reflectance/absorption edge shift towards red and exhibit lower energy bandgap of metal ions doped TiO_2 NPs relative to the pure titania, which may be due to the dopant effect on TiO_2 texture and structure. Such redshift in the

absorption spectra was also reported [25–27] for metal-doped oxide materials. The top of the VB and bottom of the CB corresponds primarily to O_{2p} and Ti_{3d} ionic states in the titania band structure. Thus, in bare titania, the band to band absorption transitions are corresponding to $O_{2p} \rightarrow Ti_{3d}$. In contrast, the slightly red-shifted absorption of doped titania NPs may originate due to the sp-d interaction between the band edge electron and the localized d electron of the doped metal ions replacing Ti^{4+} cations [28].

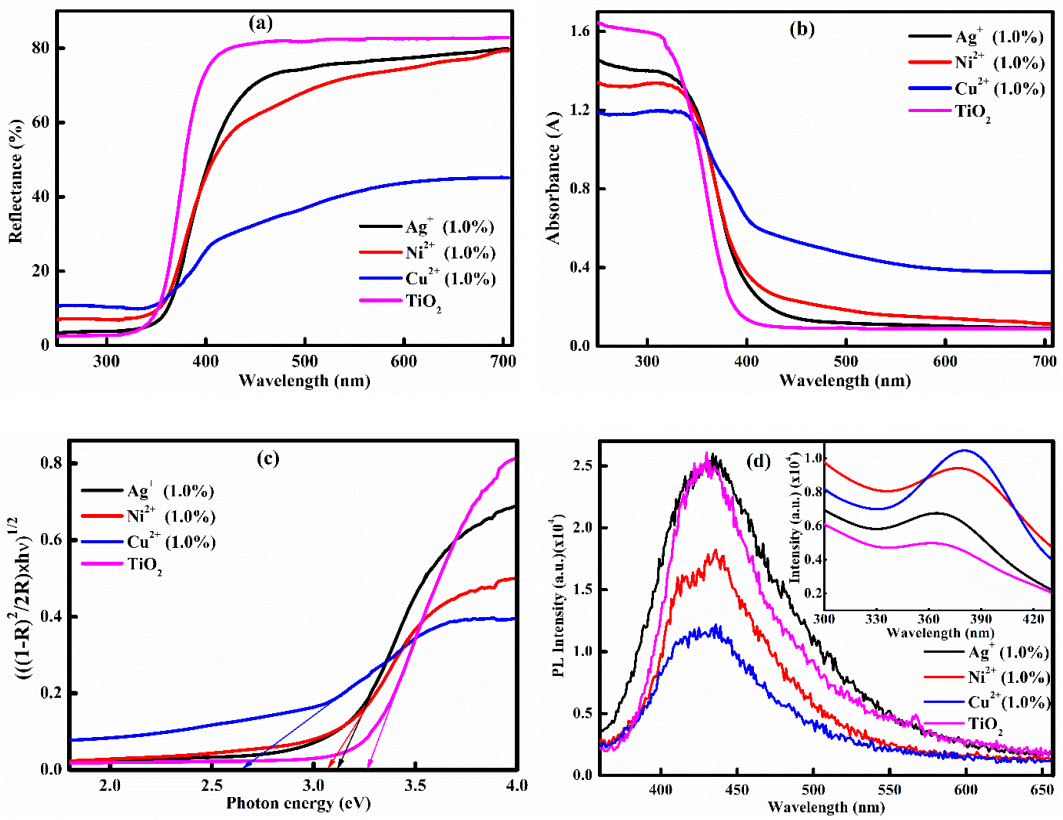

Figure 4.6. UV-vis diffuse reflectance spectra (a), absorption spectra (b), Tauc's plots correspond to the indirect bandgap (c) and PL and PL-excitation spectra (inset) (d) of TiO_2 NPs doped with various transition metal ions with excitation wavelength 340 nm.

The indirect optical bandgap of the as-prepared samples was calculated with the help of extrapolation of the tangent of the $(h\nu\alpha)^{1/2}$ vs. $h\nu$ curves tending to $(h\nu\alpha)^{1/2} = 0$, as shown in Figure 4.6(c) [29]. The estimated bandgap of undoped, 1% Ag^+, 1% Ni^{2+} and 1% Cu^{2+} doped TiO_2 NPs was found to be 3.24, 3.11, 3.06, and 2.66 eV, respectively. Thus, a reduction in optical energy bandgap was noticed for metal ions doped titania.

The PL spectra of undoped and Ag^{+}, Cu^{2+}, and Ni^{2+} ions doped titania NPs are presented in Fig. 4.6(d). The PL peak of pure TiO_2 NPs is at around 430 nm with a 340 nm excitation wavelength. The PL peak of Ag^{+} ion-doped NPs is slightly red-shifted and expands the full width at half maxima as compared with a PL band of pure TiO_2. The PL intensity decreases with the doping of Cu^{2+} and Ni^{2+} ions due to the drop in the radiative recombination rate following photoexcitation [30–32].

The fall in radiative recombination of *e-h* occurs as the excited electron migrates from CB of TiO_2 to the metal ion and is absorbed subsequently by O_2 on the surface of the metal ion. Metal ion on the surface of TiO_2 provides the additional Schottky barrier that facilitates in capturing electrons. Also, the metal defects may act as a separated energy center and help in promoting the excited electrons trapping by O_2 [30,33]. Thus, the transfer of charge carriers promoted by the presence of metal ions reduces the overall PL intensity [33]. The decrease in PL intensity is a good sign of the improvement of photoactivity of NPs. The PL-excitation spectra recorded at a fixed PL wavelength (at PL maximum) are analogous to the absorption spectra (inset of Fig. 4.6(d)) and show a clear redshift for the metal-doped TiO_2 NPs as compared to the undoped.

4.5 Photocatalytic activity

The photocatalytic activity of the as-prepared undoped and Ag^{+}, Cu^{2+}, and Ni^{2+} ions doped titania NPs was measured using a well-known cationic dye, i.e., MB, and the obtained results are shown in Fig. 4.7. The MB exhibit the lowest energy absorption band at 664 nm. The doped and undoped NPs were employed as a catalyst for the degradation of MB dissolved in an aqueous medium and kept under UV irradiation. Initially, 20 mg of the catalyst (NPs) was taken and dispersed in 30 mL solution of MB (conc. 1×10^{-5} M) in DI water and continuously stirred for 1h in the dark condition. Subsequently, the adsorption-desorption process occurs, which brings an equilibrium condition in the resultant solution.

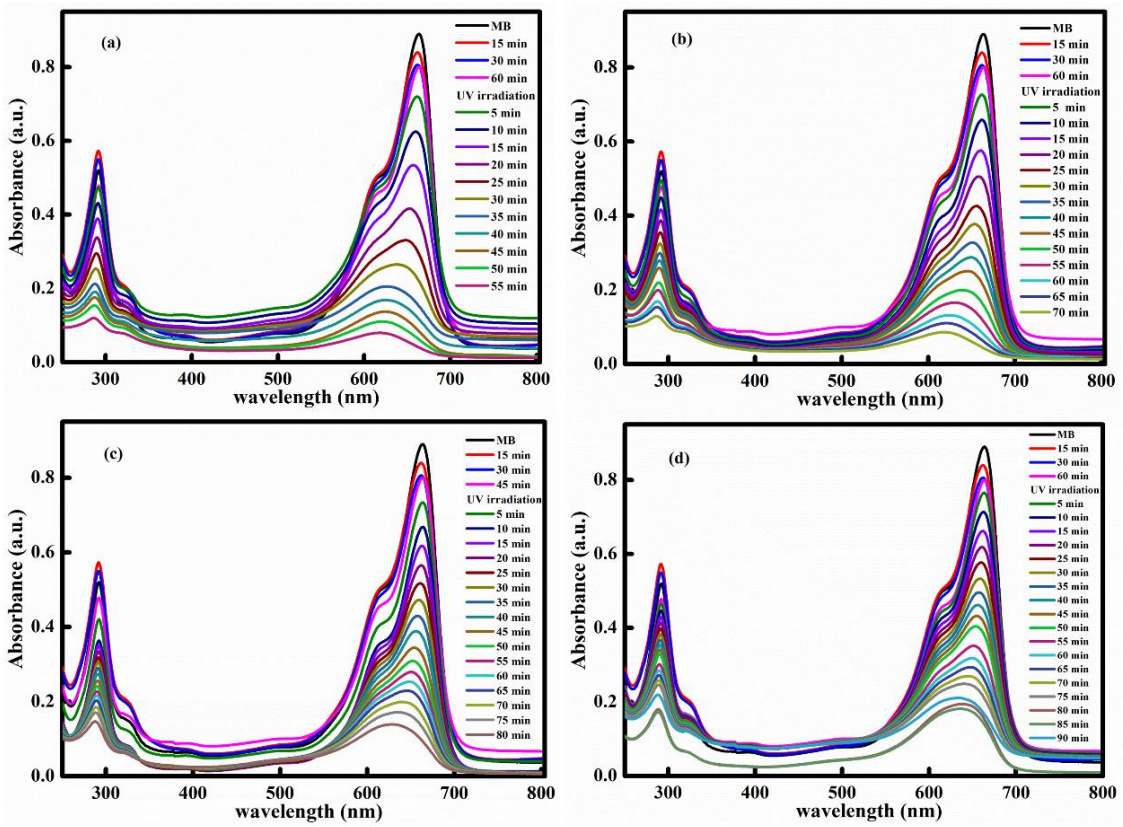

Figure 4.7. Absorption spectra of MB in water in the presence of Cu^{2+}-doped (a), Ni^{2+}-doped (b) Ag^{+}-doped (c) and undoped (d) TiO_2 NPs upon UV irradiation.

The larger particles were removed from the equilibrium solution by centrifugation at 6000 rpm. The absorption and PL spectra of the samples were measured with and without photoirradiation for comparing the effect of UV in the degradation of dye (Figs. 4.7 and 4.11). Without UV photo-irradiation, there is a small reduction in the absolute absorption intensity of the dye; this reflects the degradation of MB by the catalyst TiO_2 NPs is little, which is valid for all the metal-doped NPs. Then the equilibrium solution was irradiated with a UV light (in the presence of 254 nm) for a different duration in the presence of a catalyst (NPs). Then the absorption spectra were recorded after each dose of UV irradiation.

The absorption intensity of MB dye in the presence of Cu^{2+} doped titania catalyst decreases monotonically by the dose of UV light. Thus, the dye started degrading in the presence of a catalyst with photo-irradiation, as seen in Fig. 4.7(a). Similar studies were

performed for the $Ni^{2+}$and Ag^{+} ions doped TiO_2, and the results are illustrated in Figure 4.7. The overall decrease in the absorption intensity is different for each of TiO_2 NPs. The Cu^{2+} ion-doped TiO_2 NPs shows that the absorption of MB continuously decreases with a smaller dose of UV, *i.e.,* it decreases rapidly and a complete decrease was obtained within 55 minutes (Fig. 4.7a). On the other hand, photodegradation of MB dye with the Ni^{2+} and Ag^{+} ion-doped TiO_2 NPs takes much more time and is slow compared to Cu^{2+} ions doped TiO_2 (Fig.4.7).

Figure 4.8 displays normalized C/C_0 (A/A_0) of MB in the presence of undoped and different transition metal ion-doped TiO_2 NPs as a function of time. Where $\boldsymbol{C_0}$ (A_0) and $\boldsymbol{C}$ (A) denote the initial absorption intensity (without catalyst) and the intensity at time $\boldsymbol{t}$ of MB solution in the presence of the catalyst, respectively. The obtained plots in the presence of the different catalysts represented the photocatalytic degradation rate of MB under UV light illumination and were different for different metal ions. The Cu^{2+} doped TiO_2 catalyst demonstrated the highest photocatalytic activity as compared with other catalysts. The reaction rate constant $\boldsymbol{k}$ for the photodegradation of MB dye by undoped and metal ions doped (Ag^{+}, Cu^{2+}, and Ni^{2+}) TiO_2 NPs have been estimated using the pseudo-first-order kinetics relation $ln(C/C_0) = -kt$, where $\boldsymbol{t}$ denote the reaction time [34,35]. For each of the NPs, a linear plot between $ln(C/C_0)$ *vs* $\boldsymbol{t}$ was obtained and used to determine the kinetics of photodegradation (Fig. 4.8b). The linear relationship of $ln(C/C_0)$ *vs* $\boldsymbol{t}$ demonstrated that the rate of reaction of dye degradation following photoirradiation is pseudo-first-order kinetics [36]. The slope of the plots represented the rate of photodegradation and was different for different catalysts (NPs). The highest photodegradation rate was obtained for Cu^{2+} doped TiO_2 NPs, having the maximum rate constant of 0.05984 min^{-1}, as presented in Figure 4.8(b). On the other hand, the rate constant

was found to be 0.04093, 0.02503 and 0.02013 min^{-1} for Ni^{2+}, Ag^{+} ions doped and undoped TiO_2, respectively in the presence of 254 nm UV irradiation.

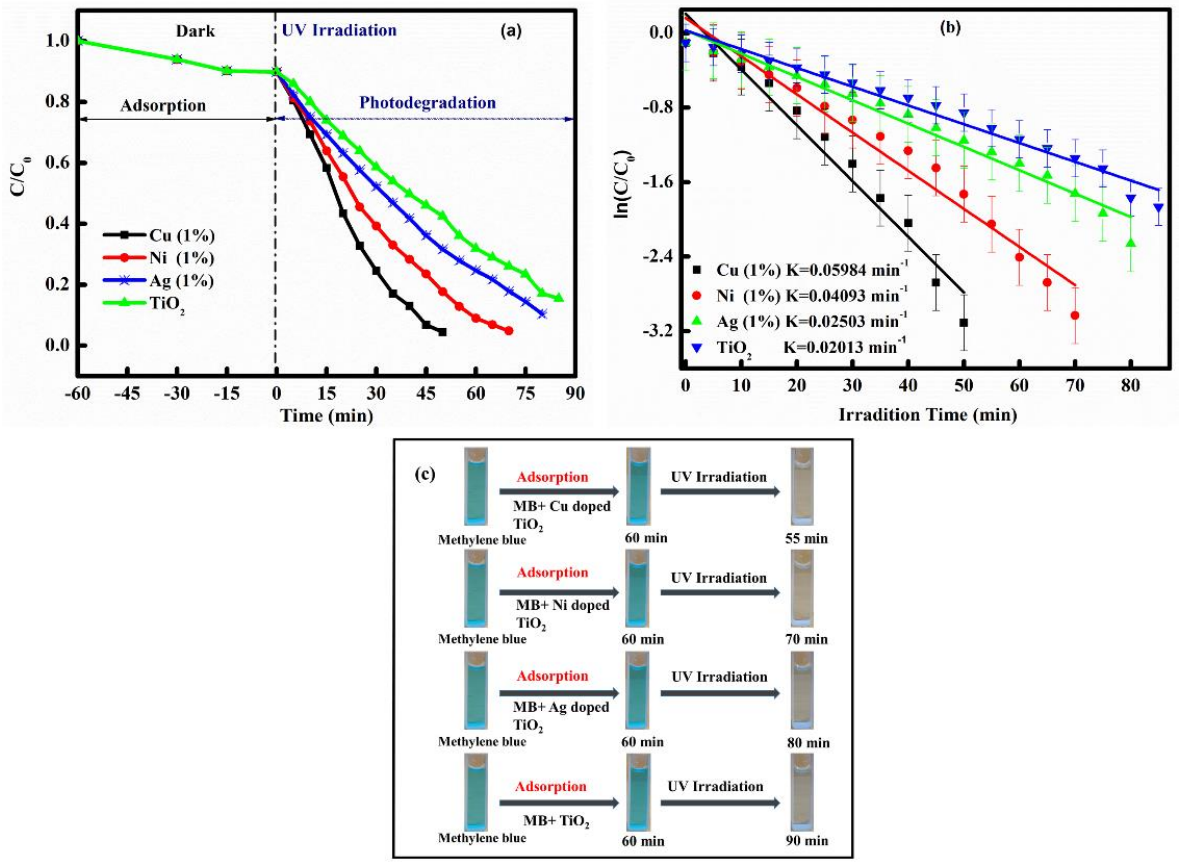

Figure 4.8. Plots of normalized C/C_0 of MB as a function of time (a) first-order reaction rate constants *k* against reaction time for undoped and different metal ions doped TiO_2 NPs (b) and digital photographs of the MB solution upon UV irradiation in the presence of undoped and various metal-doped TiO_2 NPs (c).

The degradation of the MB dye by the developed NPs upon photoirradiation can be seen with naked eyes, as shown in Fig. 4.8(c). The images of the TiO_2 NPs containing MB solution before and after UV irradiation at different time duration show that the MB was utterly degraded. However, the requirement of a dose of UV irradiation (UV irradiation time) is different for different NPs to degrade the dye completely.

In the presence of 365 nm near UV irradiation, the absorption intensity of MB dye in the presence of metal-doped titania catalyst decreases monotonically by the dose of UV

light. The overall decrease in the absorption intensity is different for each of the TiO_2 NPs in the presence of a smaller dose of UV irradiation. The rate constant was found to be 0.06022, 0.04091, 0.02496 and 0.01971 min^{-1} for Cu^{2+}, Ni^{2+}, Ag^{+} ions doped and undoped TiO_2, respectively, which is shown in Figs. 4.9 and 4.10. The pseudo-first-order reaction rate constants ***k*** of dye degradation under photoirradiation at different wavelengths for absorption is listed in Table 4.1. The resultant arrangement of catalytic degradation rate under UV irradiation was Cu-TiO_2> Ni-TiO_2 >Ag-TiO_2 >anatase TiO_2. This data suggests that bare TiO_2 NPs have a lower rate constant; hence are less efficient than doped TiO_2 NPs.

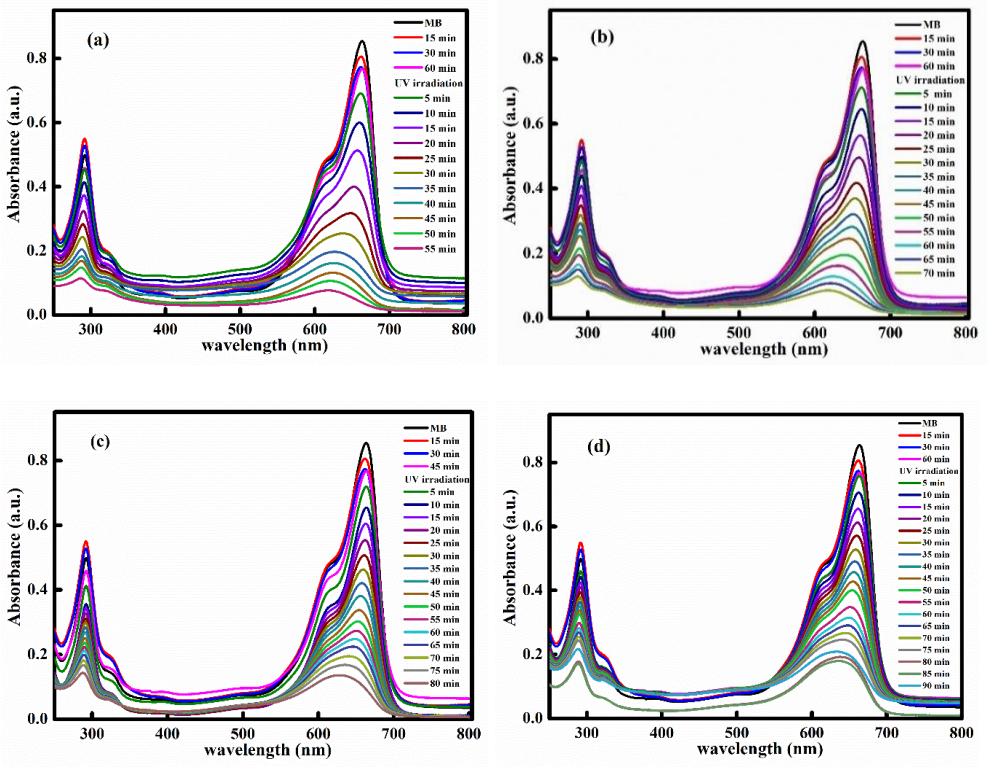

Figure 4.9. Absorption spectra of MB solution in the presence of Cu^{2+}-doped (a), Ni^{2+}-doped (b), Ag^{+}-doped (c) and undoped (d) TiO_2 NPs upon UV irradiated with 365 nm.

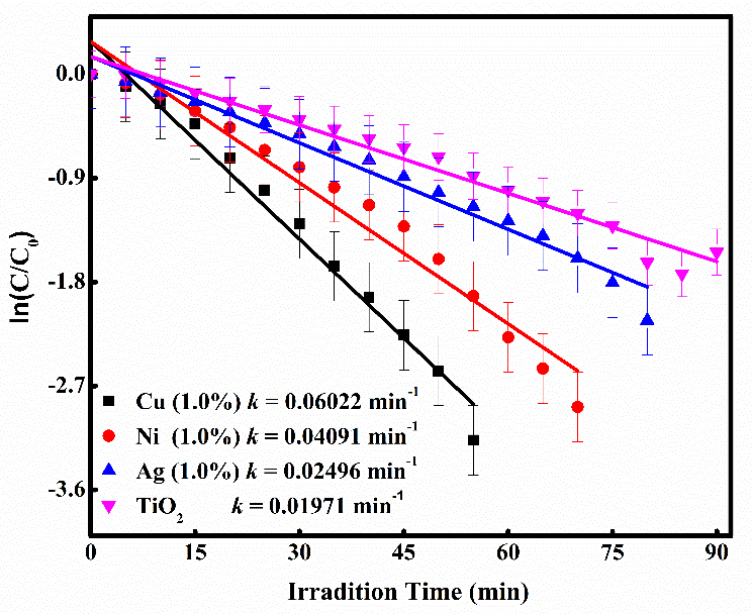

Figure 4.10. The plot of $ln(C/C_0)$ *vs.* irradiation time along with first-order reaction rate constants ***k*** for undoped and different metal ions doped TiO_2 NPs UV irradiated with 365 nm.

Table 4.1. The pseudo-first-order reaction rate constants ***k*** of dye degradation under photoirradiation at different wavelengths of UV irradiation for absorption and PL spectra.

Samples	**Absorption spectra**				**PL spectra**	
	UV irradiation (254 nm)		UV irradiation (365 nm)		UV irradiation (254 nm)	
	k (min^{-1})	χ^2	k (min^{-1})	χ^2	k (min^{-1})	χ^2
Cu^{2+}	0.05984	0.96	0.06022	0.97	0.02166	0.98
Ni^{2+}	0.04093	0.96	0.04091	0.96	0.02101	0.98
Ag^{+}	0.02503	0.97	0.02496	0.97	0.01312	0.98
Undoped TiO_2	0.02013	0.97	0.01971	0.97	0.01028	0.95

Similarly, the PL spectra of the dye were measured in the presence of the catalysts (NPs) upon UV irradiations, and the observed spectra are depicted in Fig. 4.11. The MB emits strong PL at around 688 nm and the intensity of PL decreases very fast with increasing UV irradiation to the MB solution containing the catalyst. Together with the reduction in intensity, the PL of MB shifted toward blue. Nearly after a 50% reduction of the PL intensity, a new band appeared at around 640 nm. Upon further irradiation, the intensity of the 688 nm band showed a continuous decrease, whereas the intensity of the newly developed band remained nearly constant (Fig.4.11) though the solution is colorless.

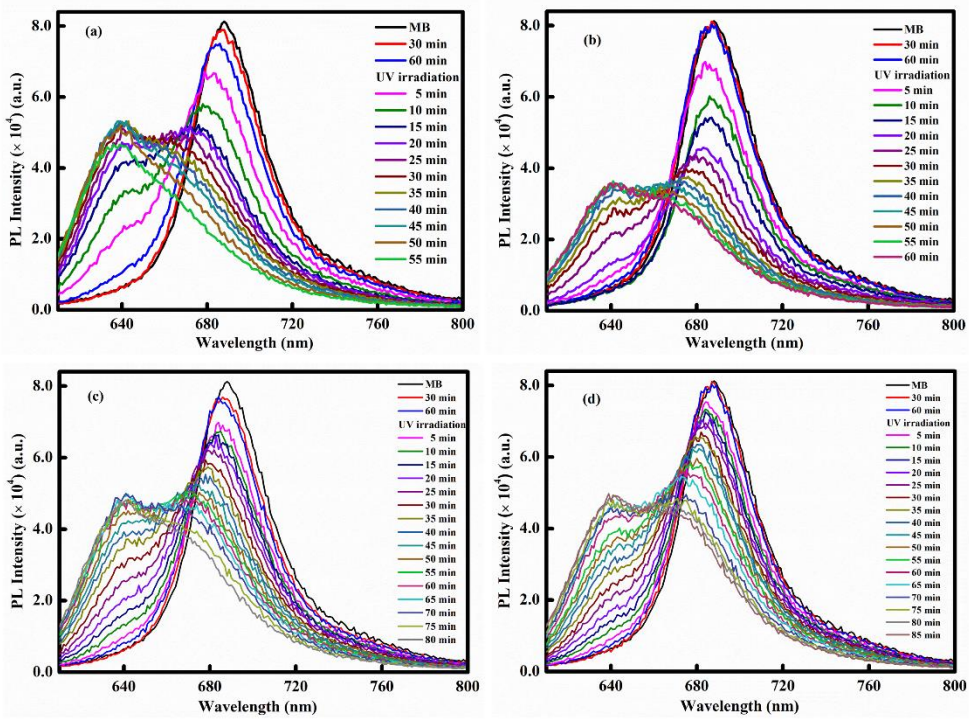

Figure 4.11. PL spectra of MB solution in the presence of Cu^{2+}-doped (a), Ni^{2+}-doped (b), Ag^{+}-doped (c) and undoped (d) TiO_2 NPs upon UV irradiation with excitation wavelength was 340 nm. Plots of C/C_0 of MB as a function of time in the presence of undoped and various transition metal-doped TiO_2 NPs (c).

The reduction in PL intensity of MB was again faster in the presence of Cu^{2+} ion-doped TiO_2 as compared to other catalysts (Fig. 4.11). The appearance of a new PL band at a higher energy region is due to the formation of new entities, i.e., thionin (Th), might

be due to the multi-demethylation (removal of $–CH_2$ group) of the MB molecules [37], which has an almost similar structure to the parent molecule (MB) but with lesser methyl groups [38]. The photodegradation rate of MB dye is plotted as a function of irradiation time and is illustrated in Fig. 4.12(a).

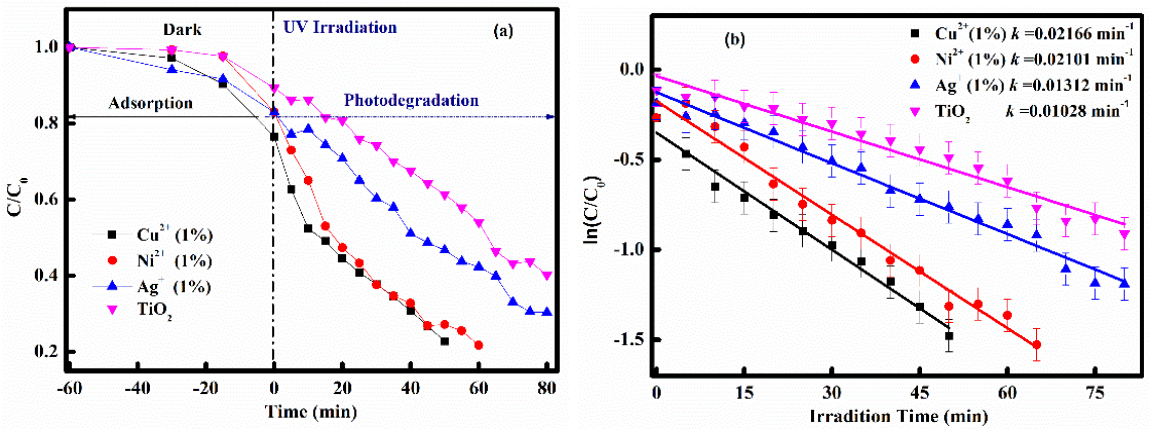

Figure 4.12 Plots of C/C_0 of MB as a function of time (a) and plots of normalized $\ln(C/C_0)$ of MB as a function of time and first-order reaction rate constants *k* against reaction time for undoped and different metal ions doped TiO_2 NPs (b).

The photodegradation rate was maximum for the Cu^{2+} doped TiO_2 (Fig. 4.12b), and obtained results agree with that of the absorption measurements. Thus, photoluminescence spectroscopy presents a new provision to analyze the degradation of dye molecules in the presence and absence of catalysts.

The titania NPs absorbed the UV light, which is equivalent to the bandgap energy of the catalyst TiO_2, electrons are excited from the top (HOMO) of the VB (O_{2p}) to the bottom (LUMO) of the CB (Ti_{3d}), which are creating separated charge carriers, *e-h* pairs. During the process, the separated *e -h* pairs react with dissolved oxygen (O_2) and hydroxyl groups of water and generate the reactive species, namely super-oxygen ions ($•O_2^-$) and hydroxyl ions (•OH). These reactive radicals participate in dye degradation and decompose it to smaller hydrocarbon and eventually to CO_2 and H_2O [7,39,40]. The schematic diagram

of photocatalytic activity of metal-doped TiO_2 NPs under UV irradiation is shown in Fig. 4.13.

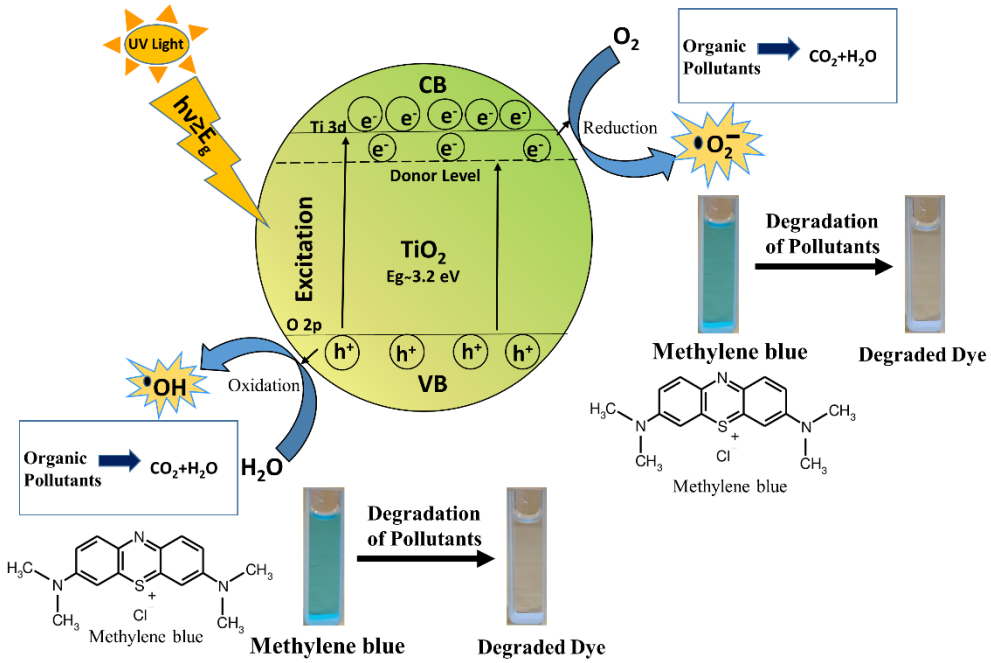

Figure 4.13 The schematic diagram photocatalytic activity of metal-doped TiO_2 NPs under UV irradiation.

The doping of transition metals in TiO_2 with Ag^+, Cu^{2+} and Ni^{2+} ions generate new trapping sites that affect the lifetime of the charge carriers and reduces the possibility of recombination. Also, it is well established that the incorporated metal ions in the host possess energy levels, which are usually lower than the CB of the host (TiO_2) [12,41]. Due to the formation of dopants energy states, the recombination rate decreases, i.e., the *e-h* recombination lifetime increases, increasing the possibility of the reaction of *e-h* with reactive species, which in turn reacted with the MB to decompose it by following advanced oxidation and reduction processes [42,43].

The PL decay profiles of MB and MB+TiO_2 with UV irradiation were recorded and illustrated in Figure 4.14. The PL decays were monitored at the peak wavelengths (λ_{max}) of 690 and 635 nm of PL spectra with excitation wavelength (λ_{ex}) of 300 nm. The observed

decay curves could not fit by a single exponential and are fitted well with bi-exponential and tri-exponential functions with a good chi-square (χ^2) values and residuals following the Eq. 4.1 [44,45]:

$$f(t) = \sum_i A_i \exp\left(-\frac{t}{\tau_i}\right), \quad (4.1)$$

where A_i represent the pre-exponential factors whereas τ_i the lifetimes.

The estimated lifetimes and corresponding pre-exponential factor values are summarized in Table 4.2, and the fitted decay curves are shown in Fig. 4.14. The average lifetime (τ_{av}) is calculated from the following Eq. (4.2):

$$\tau_{av} = \sum_i \frac{A_i \tau_i^2}{A_i \tau_i}, \quad (4.2)$$

Here, the results signify that the pure methylene blue (MB) has two lifetimes, i.e., 0.171 ± 0.023 ns and 0.386 ± 0.003 ns (Fig. 4.14), and are in line with the reported values [46]. The average lifetime (τ_{av}) estimated with Eq. 4.2 is about 0.35 ns. When TiO_2 NPs are added in MB solution and irradiated with UV for 5 minutes. The decay could not be fitted with bi-exponential functions whereas fitted well with tri-exponential function with lifetimes components of 0.170 ± 0.025, 0.385 ± 0.005 and 2.993 ± 0.205 ns (Fig. 4.14). The average lifetime, τ_{av} is increased from 0.35 to 0.57 ns (Table 4.2) with the dose of UV irradiation. The initial lifetime components are nearly the same as those observed for MB in the absence of NPs. In the presence of NPs and irradiations, the third lifetime indicates that the origin of new emitting species that produced may be due to the demethylation (removal of $–CH_2$ group) of the MB molecules, which has an almost similar structure to the parent molecule (MB) but with lesser methyl groups [37].

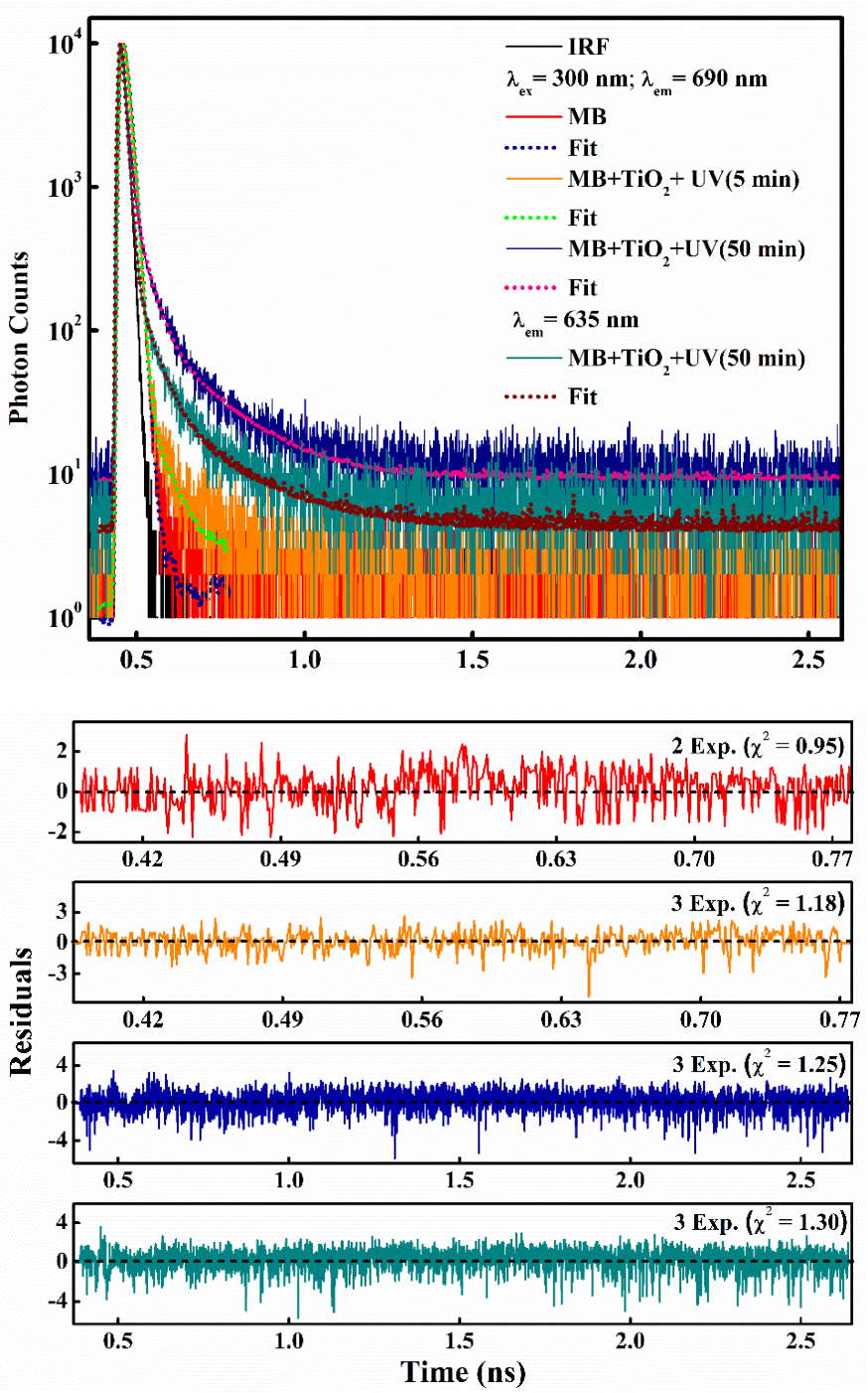

Figure 4.14. Fitted PL decay curves of MB solution and mixture solution of MB+TiO_2 irradiated with UV along with the instrument response function (IRF). The bottom curves demonstrated the weighted residuals with χ^2 values for each fitted decay.

Table 4.2. Lifetimes (τ_i) and pre-exponential factors (A_i) of MB and MB+TiO_2 with UV irradiation. The excitation wavelength (λ_{ex}) was 300 nm.

Samples	λ_{em} **(nm)**	τ_1 (ns)	τ_2 (ns)	τ_3 (ns)	A_1	A_2	A_3	τ_{av} (ns)	χ^2
Methylene Blue (MB)	690	0.171 ±0.023	0.386 ± 0.003	-	28.13	71.87	-	0.35	0.95
MB+TiO_2+UV (5 min)	690	0.170 ±0.025	0.385 ±0.005	2.993 ±0.205	30.03	68.97	1.00	0.57	1.18
MB+TiO_2+UV (50 min)	690	0.024 ±0.003	1.321 ±0.034	6.213 ±0.138	85.21	10.47	4.33	4.33	1.25
MB+TiO_2+UV (50 min)	635	0.016 ±0.002	1.734 ±0.071	8.040 ±0.434	96.13	2.87	1.00	5.03	1.30

Further, upon increasing UV irradiation time from 5 to 50 minutes, the average lifetime increases from 0.57 ns to 4.33 ns along with the shortening of the smallest lifetime component, which shows further degradation of the MB. After 50 minutes of UV irradiation, a new band appears at around 635 nm (Fig. 5). At this new band, again, the PL decay fitted well with tri-exponential function with a lifetime of 0.016 ± 0.002 ns, 1.734 ± 0.071 ns and 8.040 ± 0.434 ns (Fig. 4.14) and the τ_{av} is 5.03 ns (Table 4.2). Thus, upon UV irradiation the dye is degraded and new species arises, which has faster and slower decay rates than the pure MB.

4.6 Conclusions

The undoped TiO_2 and 1.0 w% of transition metal (Ag^+, Cu^{2+}, and Ni^{2+}) doped TiO_2 NPs were successfully synthesized via the sol-gel process. The structure of as-synthesized NPs was analyzed by XRD patterns. The calculated average crystallite size for Cu^{2+}, Ni^{2+}, Ag^+ metal ions doped titania and pristine TiO_2 are 18, 22, 27, and 30 nm, respectively. The morphological and chemical compositions of the as-prepared NPs catalysts were confirmed with FESEM, EDS, HRTEM. The formation of nanoparticles was also confirmed by FTIR analysis, which gives information about the vibration bands in the 400 to 1000 cm^{-1} region. The observed bands are associated with the Ti–O–Ti, Ti-O, R–O–Ti and R–O (where R= Ag, Cu, and Ni) bridging and stretching modes. The absorption and PL-excitation spectra of metal-doped TiO_2 NPs are shifted to the longer wavelength region, indicating a reduced bandgap than the bare TiO_2 NPs. The PL intensity of Ni^{2+} and Cu^{2+} doped TiO_2 decreases as compared to the bare NPs due to the migration of the charge carriers between metal and TiO_2. Both the bare and metal ions doped TiO_2 NPs strongly degraded the dye (MB) molecules in the presence of UV light, analyzed by absorption spectra. The rate of dye degradation is higher for metal ions doped catalyst and highest for Cu^{2+} doped TiO_2 NPs. Thus, Cu ion-doped TiO_2 shows the highest photocatalytic activity. The order of catalytic degradation rate under UV irradiation was found to be Cu-TiO_2> Ni-TiO_2 >Ag-TiO_2 >anatase TiO_2. The PL spectra and PL-decays analysis of MB reveal the formation of smaller species in the presence of NPs that emits at a shorter wavelength region with a multi-exponential decay function and an increased average PL lifetime.

References:

[1] M. A. Rauf, M. A. Meetani, S. Hisaindee, An overview on the photocatalytic degradation of azo dyes in the presence of TiO_2 doped with selective transition metals, Desalination. 276 (2011) 13–27.

[2] A. R. Khataee, M. B. Kasiri, Photocatalytic degradation of organic dyes in the presence of nanostructured titanium dioxide: Influence of the chemical structure of dyes, J. Mol. Catal. A: Chem. 328 (2010) 8–26.

[3] A. L. Ahmad, S. W. Puasa, Reactive dyes decolourization from an aqueous solution by combined coagulation/micellar-enhanced ultrafiltration process, Chem. Eng. J. 132 (2007) 257–265.

[4] M. Derudi, G. Venturini, G. Lombardi, G. Nano, R. Rota, Biodegradation combined with ozone for the remediation of contaminated soils, Eur. J. Soil Biol. 43 (2007) 297–303.

[5] J. H. Mo, Y. H. Lee, J. Kim, J. Y. Jeong, J. Jegal, Treatment of dye aqueous solutions using nanofiltration polyamide composite membranes for the dye wastewater reuse, dye. Pigment. 76 (2008) 429–434.

[6] B. Liu, E. S. Aydil, Growth of oriented single-crystalline rutile TiO_2 nanorods on transparent conducting substrates for dye-sensitized solar cells, J. Am. Chem. Soc. 131 (2009) 3985–3990.

[7] M. K. Singh, M. S. Mehata, Phase-dependent optical and photocatalytic performance of synthesized titanium dioxide (TiO_2) nanoparticles, Optik 193 (2019) 163011.

[8] Y. Ma, X. Wang, Y. Jia, X. Chen, H. Han, C. Li, Titanium dioxide-based nanomaterials for photocatalytic fuel generations, Chem. Rev. 114 (2014) 9987–10043.

[9] G. I. N. Waterhouse, A. K. Wahab, M. Aloufi, V. Jovic, D. H. Anjum, D. Sun-

Waterhouse, J. Llorca, H. Idriss, Hydrogen production by tuning the photonic band gap with the electronic band gap of TiO_2, Sci. Rep. 3 (2013) 1–5.

[10] S. F. Shaikh, R. S. Mane, B. K. Min, Y. J. Hwang, O. S. Joo, D-sorbitol-induced phase control of TiO_2 nanoparticles and its application for dye-sensitized solar cells, Sci. Rep. 6 (2016) 1–10.

[11] Y. Wan, J.Wang, X. Wang, H. Xu, S. Yuan, Q. Zhang, M. Zhang, Preparation of inverse opal titanium dioxide for photocatalytic performance research, Opt. Mater. 96 (2019) 109287.

[12] T. Wang, J. Wei, H. Shi, M. Zhou, Y. Zhang, Q. Chen, Z. Zhang, Preparation of electrospun Ag/TiO_2 nanotubes with enhanced photocatalytic activity based on water/oil phase separation, Phys. E Low-Dimensional Syst. Nanostructures. 86 (2017) 103–110.

[13] A. Kadam, R. Dhabbe, D. Shin, K. Garadkar, J. Park, Sunlight driven high photocatalytic activity of Sn doped N-TiO_2 nanoparticles synthesized by a microwave assisted method, Ceram. Int. 43 (2017) 5164–5172.

[14] H. Gerischer, Photocatalytic oxidation of organic molecules at TiO_2 particles by sunlight in aerated water, J. Electrochem. Soc. 139 (1992) 113.

[15] C. M. Wang, A. Heller, H. Gerischer, Palladium catalysis of O_2 reduction by electrons accumulated on TiO_2 particles during photoassisted oxidation of organic compounds, J. Am. Chem. Soc. 114 (1992) 5230–5234.

[16] M.K. Singh, M.S. Mehata, Enhanced photoinduced catalytic activity of transition metal ions incorporated TiO_2 nanoparticles for degradation of organic dye: Absorption and photoluminescence spectroscopy, Opt. Mater.109 (2020) 110309.

[17] P. Sharma, M. S. Mehata, Colloidal MoS_2 quantum dots based optical sensor for

detection of 2,4,6-TNP explosive in an aqueous medium, Opt. Mater. 100 (2020) 109646.

[18] M. S. Mehata, R. K. Ratnesh, Luminescence properties and exciton dynamics of core-multi-shell semiconductor quantum dots leading to QLEDs, Dalt. Trans. 48 (2019) 7619–7631.

[19] L. T. Tseng, X. Luo, N. Bao, J. Ding, S. Li, J. Yi, Structures and properties of transition-metal-doped TiO_2 nanorods, Mater. Lett. 170 (2016) 142–146.

[20] R.D. Shannon, effective ionic radii and systematic studies of inter-atomic distances in halides and chalcogenides, Acta Cryst. 32(1976) 751–767.

[21] H. Bin Lu, Y. Z. Zhou, S. Vongehr, S. C. Tang, X. K. Meng, Effects of hydrothermal temperature on formation and decoloration characteristics of anatase TiO_2 nanoparticles, Sci. China Technol. Sci. 55 (2012) 894–902.

[22] M. Khairy, W. Zakaria, Effect of metal-doping of TiO_2 nanoparticles on their photocatalytic activities toward removal of organic dyes, Egypt. J. Pet. 23 (2014) 419–426.

[23] R. Kaur, P. Singla, K. Singh, Transition metals (Mn, Ni, Co) doping in TiO_2 nanoparticles and their effect on degradation of diethyl phthalate, Int. J. Environ. Sci. Technol. 15 (2018) 2359–2368.

[24] X. Lu, X. Lv, Z. Sun, Y. Zheng, Nanocomposites of poly(l-lactide) and surface-grafted TiO_2 nanoparticles: Synthesis and characterization, Eur. Polym. J. 44 (2008) 2476–2481.

[25] M. Subramanian, S. Vijayalakshmi, S. Venkataraj, R. Jayavel, Effect of cobalt doping on the structural and optical properties of TiO_2 films prepared by sol-gel process, Thin Solid Films. 516 (2008) 3776–3782.

[26] Y. Cong, J. Zhang, F. Chen, M. Anpo, D. He, Preparation, photocatalytic activity,

and mechanism of nano-TiO_2 Co-doped with nitrogen and iron (III), J. Phys. Chem. C. 111 (2007) 10618–10623.

[27] F. Gracia, J.P. Holgado, A. Caballero, A.R. Gonzalez-Elipe, Structural, optical, and photoelectrochemical properties of Mn^{+}-TiO_2 model thin film photocatalysts, J. Phys. Chem. B. 108 (2004) 17466–17476.

[28] B. Santara, B. Pal, P. K. Giri, Signature of strong ferromagnetism and optical properties of Co doped TiO_2 nanoparticles, J. Appl. Phys. 110 (2011) 114322.

[29] E. A. Davis, N. F. Mott, Conduction in non-crystalline systems V. Conductivity, optical absorption and photoconductivity in amorphous semiconductors, Philosophical Magazine 22 (1970) 903-922.

[30] F. B. Li, X. Z. Li, Photocatalytic properties of gold/gold ion-modified titanium dioxide for wastewater treatment, Appl. Catal. A Gen. 228 (2002) 15–27.

[31] J. G. Yu, H. G. Yu, B. Cheng, X. J. Zhao, J. C. Yu, W. K. Ho, The effect of calcination temperature on the surface microstructure and photocatalytic activity of TiO_2 thin films prepared by liquid phase deposition, J. Phys. Chem. B. 107 (2003) 13871–13879.

[32] D. H. Kim, D. K. Choi, S. J. Kim, K. S. Lee, The effect of phase type on photocatalytic activity in transition metal doped TiO_2 nanoparticles, Catal. Commun. 9 (2008) 654–657.

[33] F. B. Li, X. Z. Li, The enhancement of photodegradation efficiency using Pt-TiO_2 catalyst, Chemosphere. 48 (2002) 1103–1111.

[34] P. Dulian, W. Nachit, J. Jaglarz, P. Zieba, J. Kanak, W. Zukowski, Photocatalytic methylene blue degradation on multilayer transparent TiO_2 coatings, Opt. Mater. 90 (2019) 264–272.

[35] R. V. Nair, M. Jijith, V. S. Gummaluri, C. Vijayan, A novel and efficient surfactant-

free synthesis of Rutile TiO_2 microflowers with enhanced photocatalytic activity, Opt. Mater. 55 (2016) 38–43.

[36] H. Guo, Y. Ke, D. Wang, K. Lin, R. Shen, J. Chen, W. Weng, Efficient adsorption and photocatalytic degradation of Congo red onto hydrothermally synthesized NiS nanoparticles, J. Nanoparticle Res. 15 (2013).

[37] G. S. Singhal, E. Rabinowitch, Changes in the absorption spectrum of methylene blue with pH, J. Phys. Chem. 71 (1967) 3347–3349.

[38] M. A. Rauf, M. A. Meetani, A. Khaleel, A. Ahmed, Photocatalytic degradation of methylene blue using a mixed catalyst and product analysis by LC/MS, Chem. Eng. J. 157 (2010) 373–378.

[39] T. Shahwan, S. Abu Sirriah, M. Nairat, E. Boyaci, A.E. Eroĝlu, T.B. Scott, K.R. Hallam, Green synthesis of iron nanoparticles and their application as a Fenton-like catalyst for the degradation of aqueous cationic and anionic dyes, Chem. Eng. J. 172 (2011) 258–266.

[40] S. Liu, E. Guo, L. Yin, Tailored visible-light driven anatase TiO_2 photocatalysts based on controllable metal ion doping and ordered mesoporous structure, J. Mater. Chem. 22 (2012) 5031–5041.

[41] J. Low, B. Cheng, J. Yu, Surface modification and enhanced photocatalytic CO_2 reduction performance of TiO_2 : a review, Appl. Surf. Sci. 392 (2017) 658–686.

[42] Y. Nam, J. H. Lim, K. C. Ko, J. Y. Lee, Photocatalytic activity of TiO_2 nanoparticles: A theoretical aspect, J. Mater. Chem. A. 7 (2019) 13833–13859.

[43] M. Humayun, F. Raziq, A. Khan, W. Luo, Modification strategies of TiO_2 for potential applications in photocatalysis: A critical review, Green Chem. Lett. Rev. 11 (2018) 86–102.

[44] P. Sharma, M. S. Mehata, Rapid sensing of lead metal ions in an aqueous medium

by MoS_2 quantum dots fluorescence turn-off, Mater. Res. Bull.131 (2020) 110978.

[45] R. K. Ratnesh, M. S. Mehata, Tunable single and double emission semiconductor nanocrystal quantum dots: a multianalyte sensor, Methods Appl. Fluoresc. 6 (2018) 035006.

[46] L. M. Moreira, J. P. Lyon, A. P. Romani, D. Severino, M. R. Rodrigues, H. P. M. de Oliveira, Phenotiazinium dyes as photosensitizers (PS) in photodynamic therapy (PDT), in: Spectroscopic properties and photochemical mechanisms, Advanced Aspects of Spectroscopy, InTech. (2012) 393-422.

Chapter-5

Temperature and time-dependent Photoluminescence of TiO_2 nanoparticles*

5.1 Introduction

Metal oxide semiconductors as photocatalysts are extensively studied due to their numerous applications like production of clean hydrogen energy, air purification, water splitting, wastewater treatment, self-cleaning surfaces, CO_2 reduction and disinfection in terms of fortification of the precious environment [1–5]. Among the various semiconductor materials, titanium dioxide (TiO_2) became the most significant photocatalytic material due to its high chemical and thermal stability, non-toxic behavior, and good degradation efficiency. TiO_2 nanoparticles (NPs) generally exist in two polymorphic phases, popularly known as the rutile and the anatase phase of TiO_2 materials. The anatase phase was found efficient in photovoltaic and photocatalytic applications due to its lattice structure and surface area [6]. In comparison, the rutile phase of the TiO_2 was employed majorly in sectors that involve high-end optics and electronics because of its high dielectric constant [7]. Thermodynamically, the rutile phase is more stable than anatase, and its formation begins at the annealing temperature of 550 °C and above [8]. The TiO_2 samples annealed at 550 - 800 °C give rise to a mixed-phase, which combines both anatase and rutile phase properties and is called the inorganic heterojunction. The reduced size of the TiO_2 NPs makes it a wideband semiconductor holding a bandgap of 3.0 and 3.2 eV for the rutile and anatase phase, respectively [9].

*Content of this chapter have been published in **Ceramics International 47 (2021) 32534–32544.**

The studies show that the mixed-phase, which contains the anatase and rutile heterojunction, is more active towards the photocatalytic characteristics than the individual anatase and rutile phases for degradation of environmental pollutants and photocatalytic H_2 evolution [10–12]. The improved photocatalytic activity ascribed to reduced charge recombination and effective charge separation at anatase-rutile phase junctions. The charge transfer has been studied theoretically and experimentally at inorganic heterojunctions and paid attention to the electron transfer mechanism. The process of electron transfer in the phase transformation from rutile to anatase was extensively studied employing surface photovoltage spectroscopy (SPV) [13], solid-state NMR spectroscopy [14], time-resolved terahertz spectroscopy [15] and electron paramagnetic resonance spectroscopy [16]. In support of these, the band orientation of rutile and anatase phases could be determined through X-ray photoelectron spectroscopy analysis [17,18]. The process of electron transfer from anatase to rutile was also examined by using SPV [19], EPR [20], time-resolved mid-infrared spectroscopy [21] and transmission electron microscopy (TEM) [22]. Another method for studying the reaction dynamics of photogenerated charge carriers in semiconductor is to use time-resolved microwave conductivity (TRMC) [23,24]. TRMC method has been applied to study the charge carrier lifetime and interfacial electron-transfer rate constant in anatase, rutile, anatase/rutile mixtures, and in quantum-sized TiO_2 [25].

Photoluminescence (PL) characteristics are a very prevailing and philosophical procedure to track the evolution of oxygen vacancies in TiO_2. PL spectrum of materials generated as an outcome of the recombination of photoinduced charge carriers, also known as radiative recombination of self-trapped excitons (STEs) [26]. The PL spectrum gives information about the electronic structure of the semiconductor NPs, as well as describes the photochemical and optical characteristics due to the oxygen vacancies and defects from

the surface, typically assigned to oxygen vacancies, Ti^{3+} sites, O^{-} centers, and surface hydroxide species [27,28]. The reduction in PL intensity was observed because the lessening in the recombination rate of photon-generated electron-hole pairs simultaneously enhances the photocatalytic characteristics of semiconductor catalysts [29,30]. Instead of the steady-state PL, the time-resolved PL (TRPL) method was opted to resolve the mechanism of photogenerated electrons and holes [31,32]. The TRPL study has revealed that decay curve has two components i.e., exponential decay and power law which reflecting two different formation process of STEs from photocarriers. The exponential component was attributed to a direct formation process of STEs, whereas the power law component was attributed to an indirect formation process involving carriers trapped at lattice defects or impurities [33–35].

In this work, TiO_2 NPs has been synthesized by employing the sol-gel routes and calcined at different temperatures to form pure anatase, pure rutile and mixed (anatase/rutile) phases. The optical and structural characteristics were performed at different temperatures and analyzed with the help of low-temperature PL, TRPL and other characterization techniques [36].

5.2 Experimental

Titanium (IV) isopropoxide (TTIP, $C_{12}H_{28}O_4Ti$, 97%, Alfa Asear) as titanium precursor, absolute ethanol (C_2H_5OH, analytical grade), iso-propyl alcohol (IPA, $(CH_3)_2CHOH$, 99%, assay), hydrochloric acid (HCl, Thomas Baker, analytical grade), deionized (DI) water (specific resistivity =18.2 MΩ.cm) were used as precursors.

The detailed procedure for the preparation of TiO_2 NPs has opted from published articles [3]. As per the procedure, 0.05 M solution of TTIP has been drop by drop mixed in a specific amount of IPA and DI water under vigorous stirring. The pH value maintains at 3 by using diluted HCl solution under continuous stirring at 60 °C. After a certain period,

the resultant solution turned into gel. The obtained gel was several times washed with DI water and dried in the oven. The obtained powder was annealed at numerous temperatures (400, 600 & 900°C). Finally, TiO_2 nanocrystalline powder was obtained with different phases corresponding to different annealing temperatures. The solid powder of TiO_2 was used in all the experiments, including PL and TRPL, at low temperatures.

5.3 Characterization techniques

A low-temperature X-ray diffractometer (Bruker D8 Discover equipped with CuKα source of radiation) has been used to measure the diffraction patterns of TiO_2 NPs. The morphological analysis was performed by field emission scanning electron microscopy (FE-SEM, Gemini electron-optics). The absorption and UV–vis diffuse reflectance (DRS) spectra were recorded with a UV/VIS/NIR spectrometer (Perkin Elmer, lambda 750). The PL and TRPL spectra were recorded on a spectrofluorometer (Fluorolog-3, Horiba Jobin Yvon) attached with a source of Xenon and flash lamps. The temperature controller system, Janis VNF-100 cryostat (Janis Research Company, Inc.), is a versatile variable temperature liquid nitrogen cryostat with a temperature controller (Cryo. Con 22C, Cryogenic Control Systems Inc.) attached with silicon diode thermometer and 50 Ω cartridge heater was used for varying the temperature of the samples. The sample is located in a flowing stream of nitrogen vapor. The sample temperature was accurately controlled between 77 K to 300 K with an error of ±1 K. The temperature control system is mounted in a spectrofluorometer to performed low-temperature experiments with the TiO_2 samples. Time-correlated single-photon counting (TCSPC) was used to measure PL decay profiles. TCSPC (DeltaFlex-01-DD, Horiba Jobin Yvon) fitted out with PPD 850 detector and wavelength 340 nm DeltaDiode used as a source. The ludox scatterer was used to measure the instrument response function. TRPL data were analyzed using DAS software.

5.4 Results and discussion

The TiO_2 NPs were annealed at various temperatures, i.e., 400, 600 & 900 °C, to achieve different phases. The powder XRD patterns at low-temperature of the TiO_2 samples were measured between 290 K - 77 K temperatures, as shown in Figure 5.1. The sample annealed at 400 °C show the intense peaks at Bragg's angle 2θ = 25.2°, 37.8°, 48.1°, 53.9°, 55.0°, 62.7° and 69.1° are the signature XRD peaks of pure anatase phase of TiO_2 with tetragonal structure. Meanwhile, the intense peaks at Bragg's angle 2θ = 25.3°, 27.3°, 36.1°, 41.2°, 47.9°, 53.9°, 62.7°, and 68.8° was recorded for the sample annealed at 600 °C, indicating the formation of mixed-phase (anatase/rutile) of the TiO_2 sample. Whereas, the presence of narrow and intense peaks in the recorded patterns at 2θ = 27.4°, 36.4°, 39.1°, 41.1°, 54.3°, 56.5°, 64.2° and 69.1° demonstrated the formation of pure rutile phase of TiO_2 having tetragonal structure obtained at 900 °C.

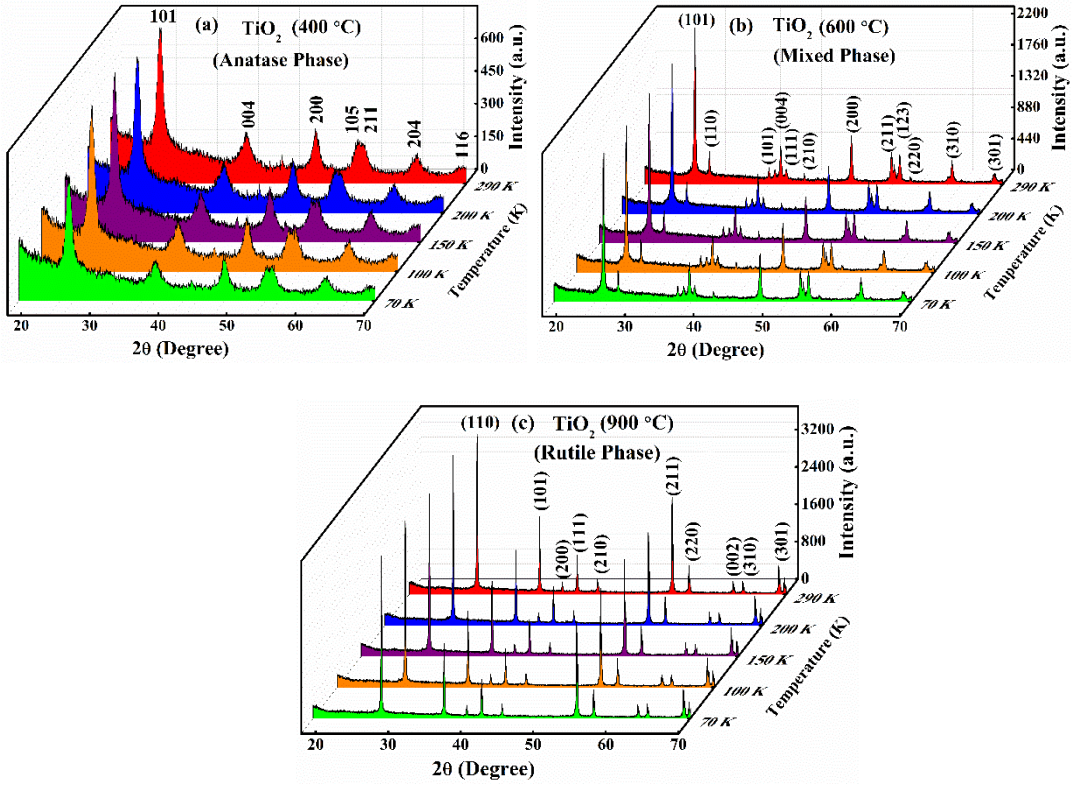

Figure 5.1. XRD patterns of TiO_2 NPs obtained at varying temperatures for 400 °C (a), 600 °C (b) and 900 °C (c).

The obtained diffraction patterns were well indexed with the standard data (JCPDS no.: 01-21-1272, 01- 084-1286 and 01-073-1765). It has been noticed that as the calcination temperature increases (400 to 900 °C), the intensity of the peaks increases but widths (FWHM) decrease, which illustrates the increment in particle size of the TiO_2 NPs [3]. As the temperature decreases from 290 K to 77 K, a usual trend was observed in the XRD patterns, with no change in the fundamental structural phases of TiO_2. The intensity and widths increase due to different kinds of internal tension (tensile and compressive) [37]. Therefore, no change in the peak positions (2θ) illustrates that the lattice parameters or the unit cell volume do not change throughout the temperature range.

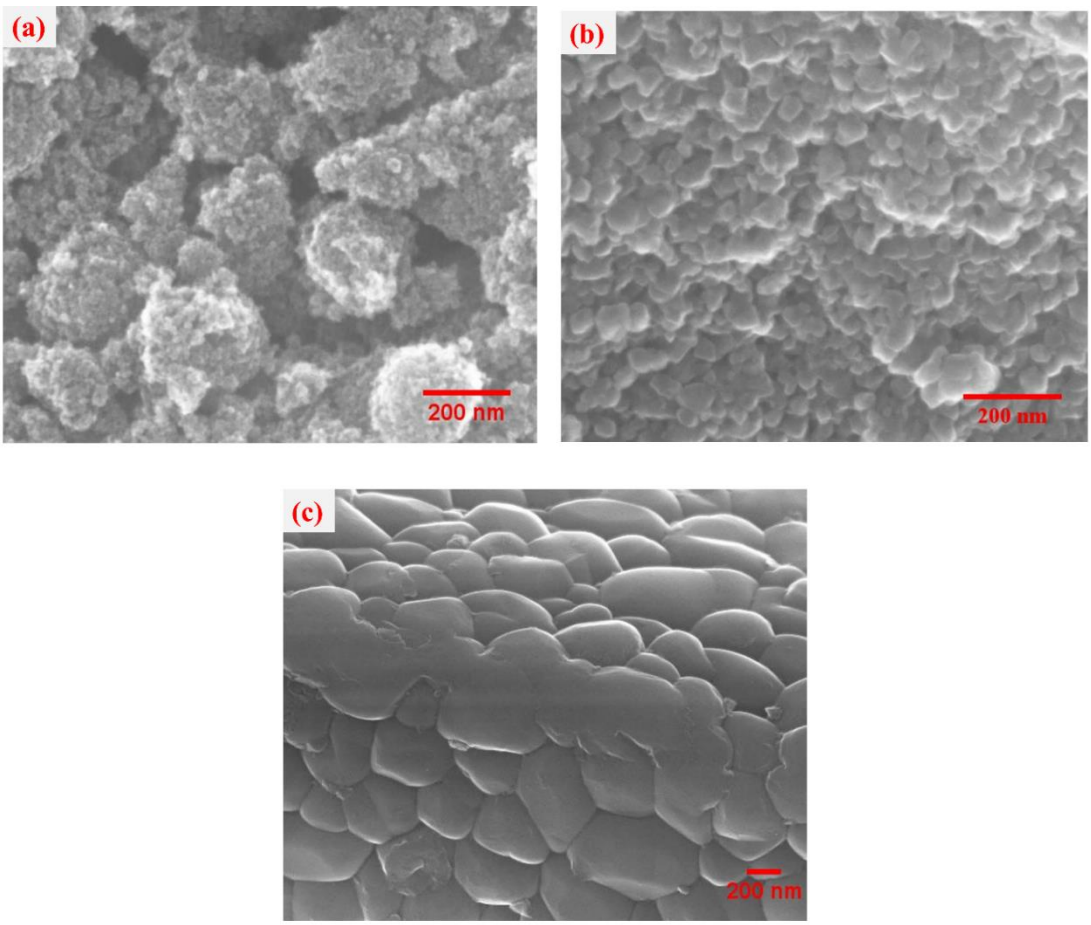

Figure 5.2. FE-SEM images of TiO_2 NPs formed at room temperature of 400 °C (a), 600 °C (b) and 900 °C (c).

Surface morphological studies of the synthesized TiO_2 samples were scanned by FE-SEM and are displayed in Figure 5.2. Around the scan area, it can be found that the TiO_2 NPs are densely aggregated with the average particle size of 5-20 nm range. From the SEM images, it was noticed that the particle size of anatase phase TiO_2 NPs (Fig. 5.2a) is smaller than the mixed (Fig. 5.2b) and rutile phases (Fig. 5.2c). The particle size and crystallinity of the TiO_2 were increased with annealing temperature, which might be because of the structural phase transformation as also revealed in the XRD patterns [3]. The smaller particle size further can endorse the larger contact between catalysts and dye compounds, enhancing the photocatalytic activity.

The DRS and absorption spectra of TiO_2 NPs observed at room temperature (RT=300 K) and pressure and are presented in Figure 5.3. The typical band-edge absorption properties were noticed for anatase and rutile phases of TiO_2 NPs. With the increase in calcination temperature from 400 °C to 900 °C, the absorption edge shifted from a shorter to longer wavelength region (326 to 380 nm). This shift is associated with the phase conversion from anatase to rutile of TiO_2 NPs with enhancing crystallinity and the size of NPs [3].

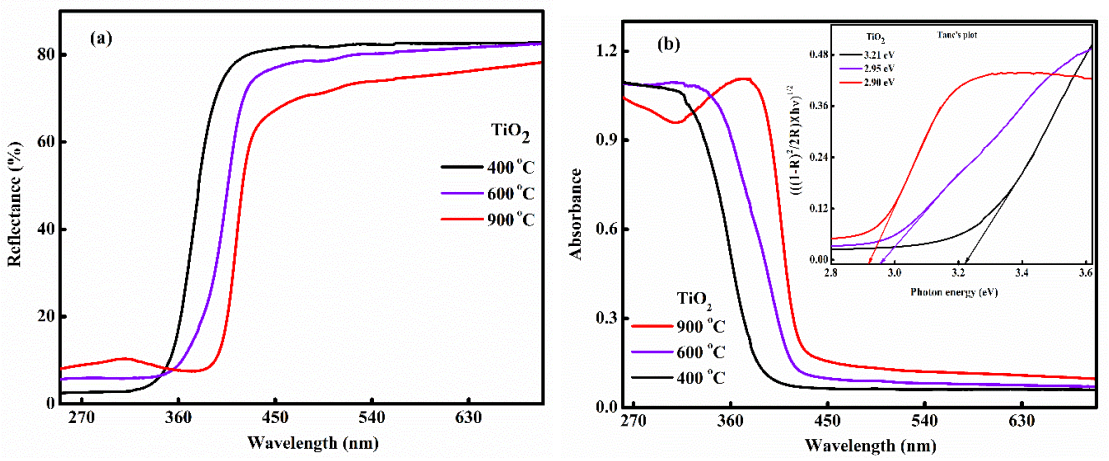

Figure 5.3. UV–vis diffuse reflectance (a) absorption (b) with Tauc's plot (inset) of TiO_2 NPs at room temperature.

The band structure of TiO_2 has the occupied valance band (VB) and unoccupied conduction band (CB) illustrates as O(2p) and Ti(3d) levels, respectively [38]. Thus, the absorption spectrum of TiO_2 corresponds to the transitions from O(2p) to Ti(3d) level, which denotes band-to-band transition. The determination of the phase-dependent optical bandgap of TiO_2 NPs was determined by the positions of CB and VB, which is strongly related to its phase composition, crystal structure, morphology, and grain size [38]. The bandgap of mixed-phase of TiO_2 NPs should possess the value intermediate of the pure anatase and rutile phases [39]. The optical bandgap estimated by Tauc's plot are 3.21, 2.95 and 2.90 eV for 400 °C, 600 °C & 900 °C, respectively [3].

5.5 Temperature-dependent photoluminescence

The temperature dependence photoluminescence (TD-PL) spectra for TiO_2 NPs were recorded with varying temperatures from 290 K to 77 K at the excitation wavelength of 340 nm. The observed results are shown in Figure 5.4. For the anatase phase, PL spectrum consists of two well-defined bands, namely a shorter wavelength band at around 410 nm at 290 K and a longer wavelength band around 530 nm at 77 K, as shown in Fig. 5.4(a,a′). The 530 nm band starts originating while temperature lowered to 200 K and became prominent at 100 K and 77 K (Fig. 5.4(a,a′)). At 77 K, the intensity of the 530 nm band is nearly fifteen-fold higher than the 410 nm band, whereas the intensity of the 410 nm band is affected slightly. For the mixed phase, the PL spectrum is observed at around 420 nm at 290 K. While decreasing temperature, a 530 nm band arises and is prominent at 100 K and 77 K, as shown in Fig. 5.4(b,b′), similar to that observed for anatase phase of TiO_2. In the mixed phase, in addition to the two well-resolved bands, a weak PL band was also observed in the NIR region at around 820 nm and showed the highest intensity at around 200 K (Fig. 5.4(b,b′)). This feature is considered to be the rutile phase of the TiO_2 NPs. The rutile phase of TiO_2 NPs consists of three well-resolved bands, two in the visible region and one in the

NIR region, which arises at around 420 nm at 290 K and strong bands at 520 nm and 820 nm at 77 K. The intensity of 820 nm band is highest. It is nearly ten times higher than the 520 nm band at the low temperature of 77 K, unlike the anatase and mixed phases in which the 520 nm band is fifteen-fold higher than the blue PL (410 nm/420 nm).

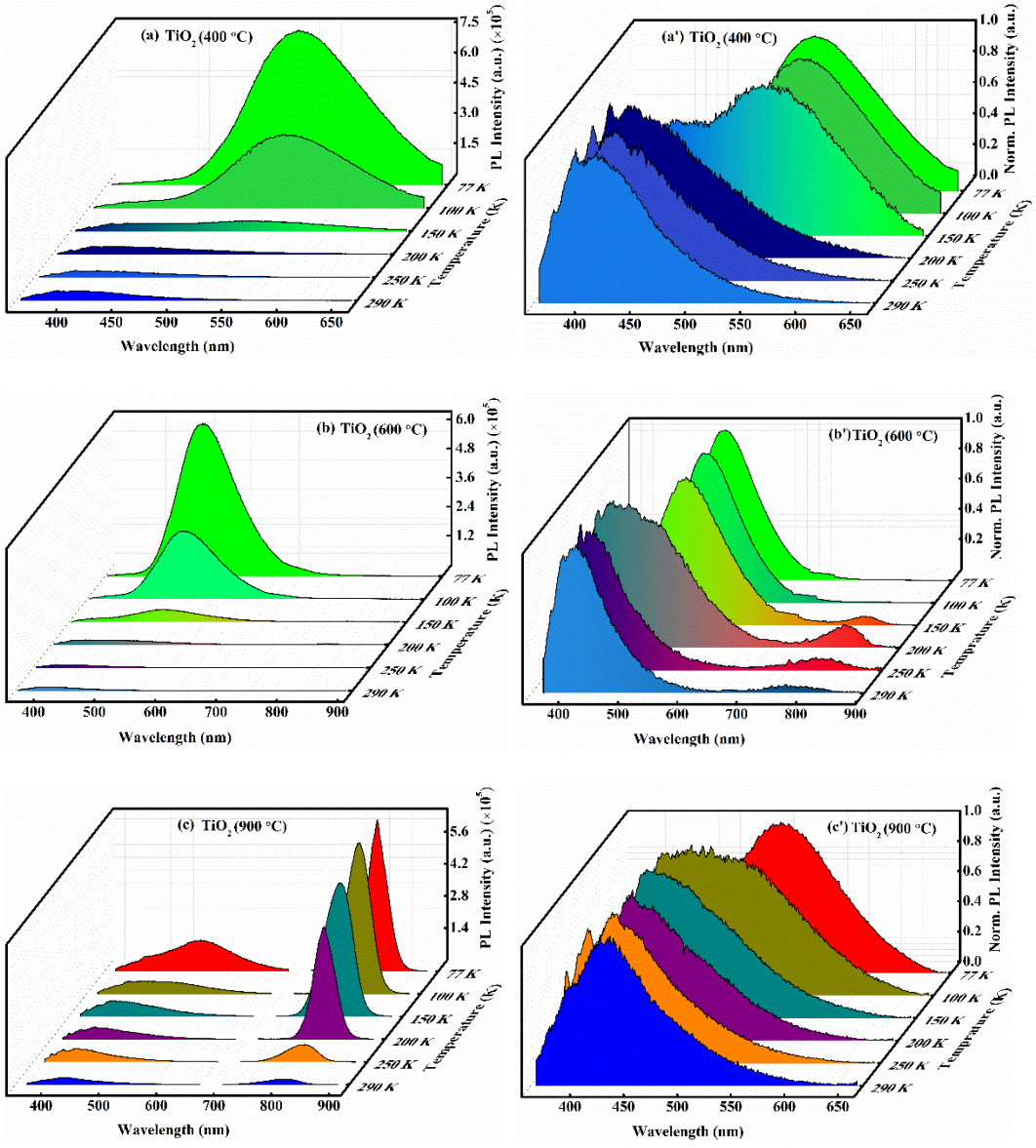

Figure 5.4. Temperature-dependent PL spectra and normalized PL spectra at excitation λ_{ex} = 340 nm of TiO_2 NPs formed at varying temperature of 400 °C (a), 600 °C (b) and 900 °C (c).

The crystalline structure of TiO_2 determines the position of PL bands [40]. The visible and NIR PL bands of TiO_2 attribute to the development of oxygen vacancies in the

anatase phase and the intrinsic defects in the rutile phase [41]. Furthermore, donor-acceptor recombination and charged oxygen defects are also responsible for the visible PL band in TiO_2. This implicates the presence of both the trapped electrons and holes are closely related to visible PL. Besides, the trap state is responsible for the NIR PL band. As a result, either trapped electrons or trapped holes should be accountable for the NIR PL band. Figure 5.5 depicts the PL evolution with the phase conversion of TiO_2 NPs by a surge at calcination temperature.

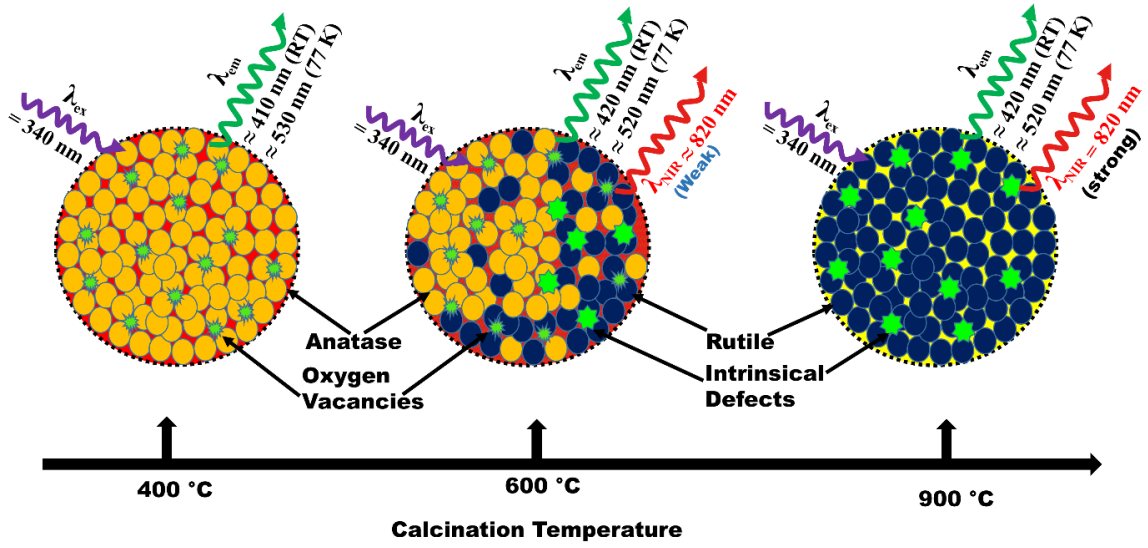

Figure 5.5. Schematic representation of the evolution of photoluminescence with the phase transformation of TiO_2 NPs by increasing calcination temperature.

At a low temperature of 77 K, the PL intensity of 530 and 820 nm bands (except in the anatase phase) raised significantly for all phases of TiO_2, without change in band position. When the temperature increases from 77 K, the PL band of anatase and mixed-phase of TiO_2 appear in the visible region (530 nm) is decreased rapidly and almost disappeared as the temperature touches 200 K [41,42]. As the temperature increases, the trapped carriers begin to recombine non-radiatively, which might be due to the separation of charges [43]. As the temperature rises from 77 to 100 K, the NIR PL band intensity of rutile TiO_2 remains relatively unchanged whereas diminished at high temperatures. As a

mechanism, the multiphonon-induced radiationless process better explains the changes that occurred [42,44]. This originates owing to the formation of deep energy levels of the trap states in the rutile phase. The trapped carriers cannot be excited thermally to the CB in the rutile phase at 100 K [41].

The TD-PL spectra in the form of contour maps of TiO_2 NPs can be seen in Figure 5.6. The contour plots evidence the PL in the visible region with an emission range from 420 to 580 nm and excitation range 300 to 400 nm, emphasized by the red elliptical circle ascribed to the anatase phase of TiO_2. The PL in the NIR region with emission range 790 to 880 nm and excitation range 300 to 380 nm, highlighted by red elliptical circle ascribed to rutile phase of TiO_2 NPs. Figure 5.6 (a,b) represented the anatase phase, which lies in the visible region. As the applied temperature decreases from 290 K to 77 K, the highlighted red elliptical circle shifted towards a longer wavelength region from 420 – 460 nm to 500 – 550 nm.

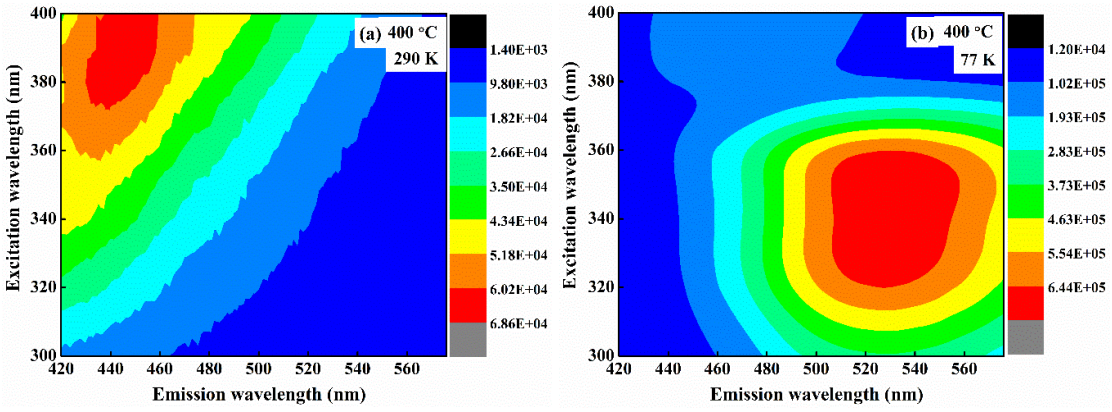

Figure 5.6: The photoluminescence contour map images obtained at 290 K and 77 K of TiO_2 NPs formed at 400 °C (a,b). Excitation wavelength (λ_{ex}) = 340 nm.

The mixed-phase PL contour map is shown in Figure 5.6 (c,d), which lies in the visible and NIR regions. When applied temperature decreases from 290 K to 77 K, the highlighted red elliptical circle shifted towards longer wavelength region from range 420 –

460 nm to 480 – 550 nm, along with a weak NIR PL region at around 800 – 830 nm was also observed, which show the formulation of the rutile phase of TiO_2 over the surface.

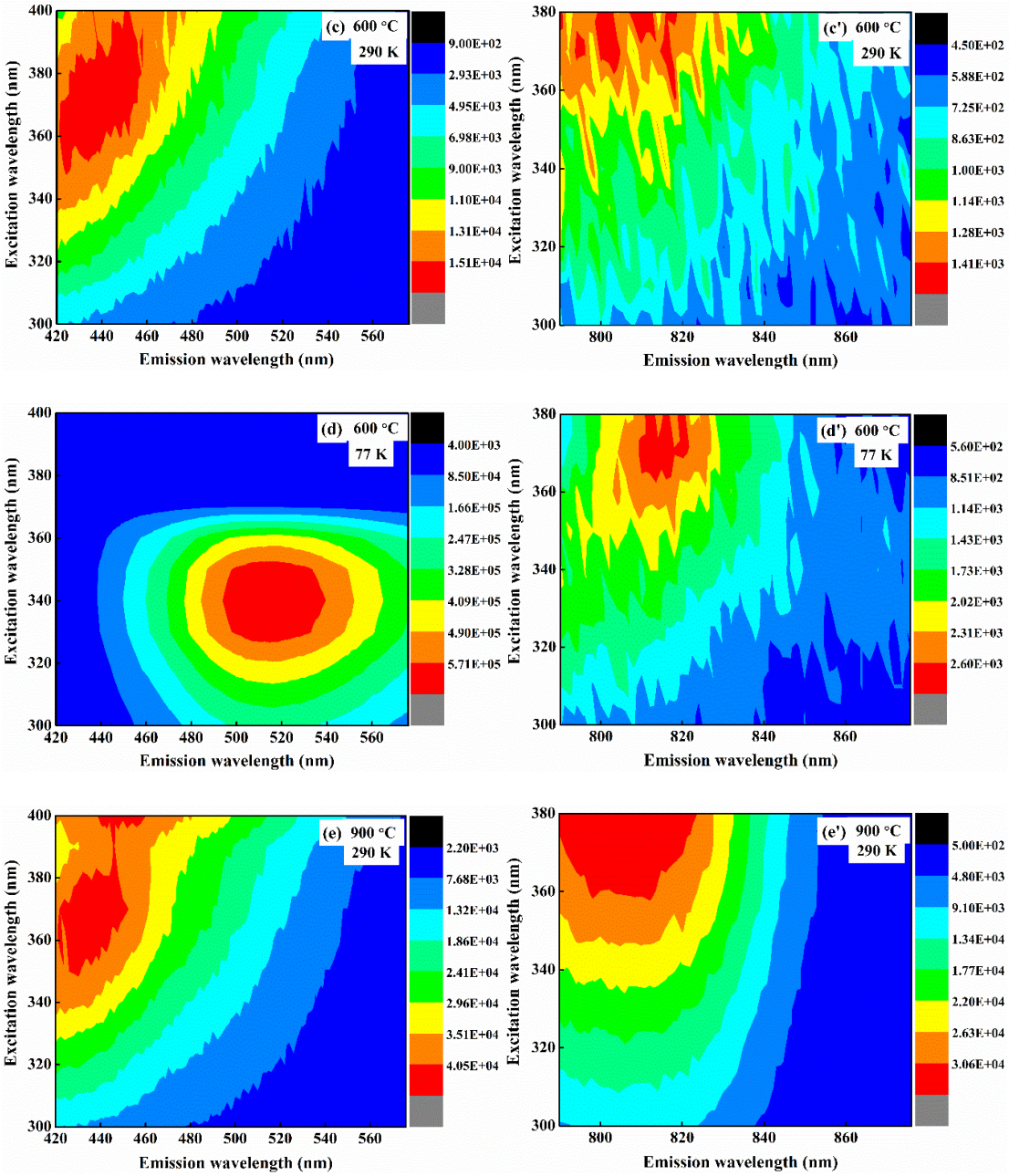

Figure 5.6: The photoluminescence contour map images obtained at 290 K and 77 K of TiO_2 NPs formed at 600 °C (c,d) and 900 °C (e,f). Excitation wavelength (λ_{ex}) = 340 nm.

Figure 5.6 (e,f) shows the visible and NIR PL for the rutile phase with a decrease in temperature from 290 K to 77 K. As a result, the highlighted red elliptical circle

wavelength region from range 420 – 450 nm to 430 – 530 nm. In the range of 800 – 830 nm wavelength, a red elliptical circle shows a strong NIR luminescence band confirm to the rutile phase, in which the deep traps are present. Figure 5.6 (f, f′) clearly indicates the two visible and one NIR bands when the excitation wavelength increases from 330 to 400 nm at a lowering temperature of 77 K. The contour maps of all the other three phases of TiO_2 obtained at different temperatures (250 K – 100 K) are shown in Figure 5.7(1), 5.7(2), and 5.7(3).

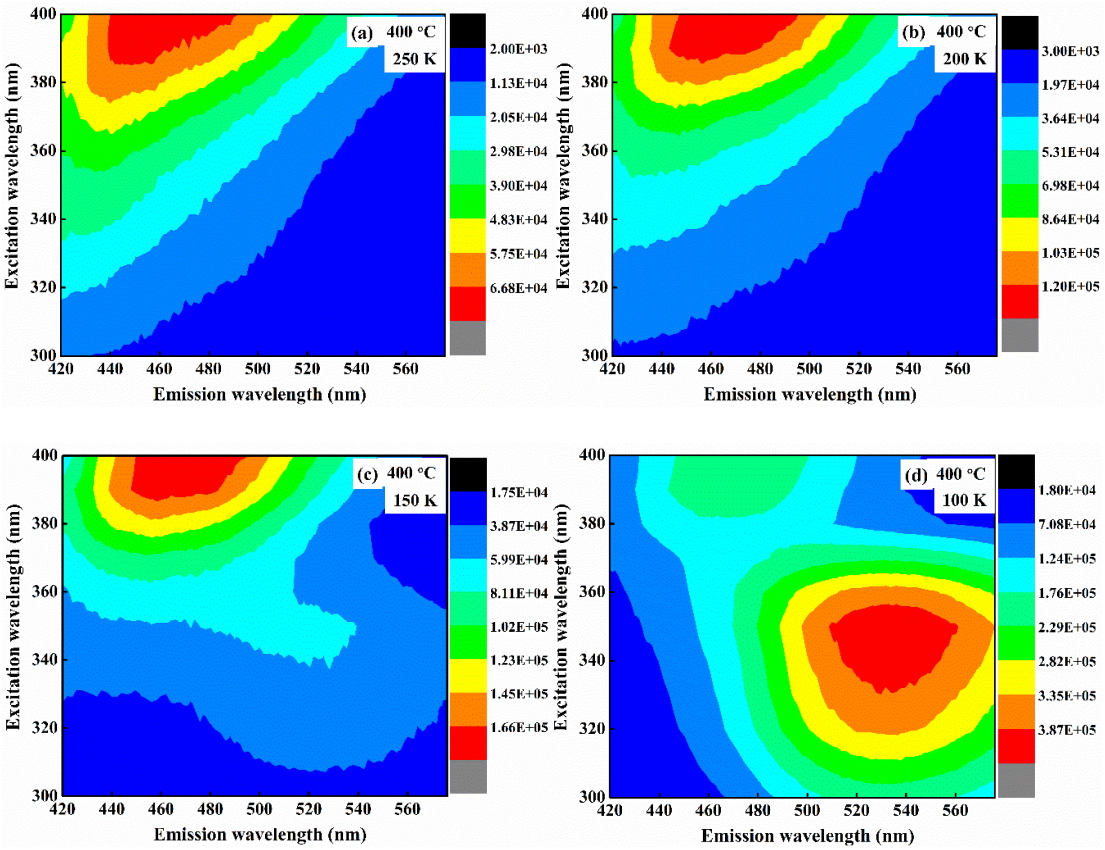

Figure 5.7(1). The photoluminescence contour map images of anatase phase of TiO_2 NPs (400 °C) obtained at varying temperatures from 290 K to 77 K.

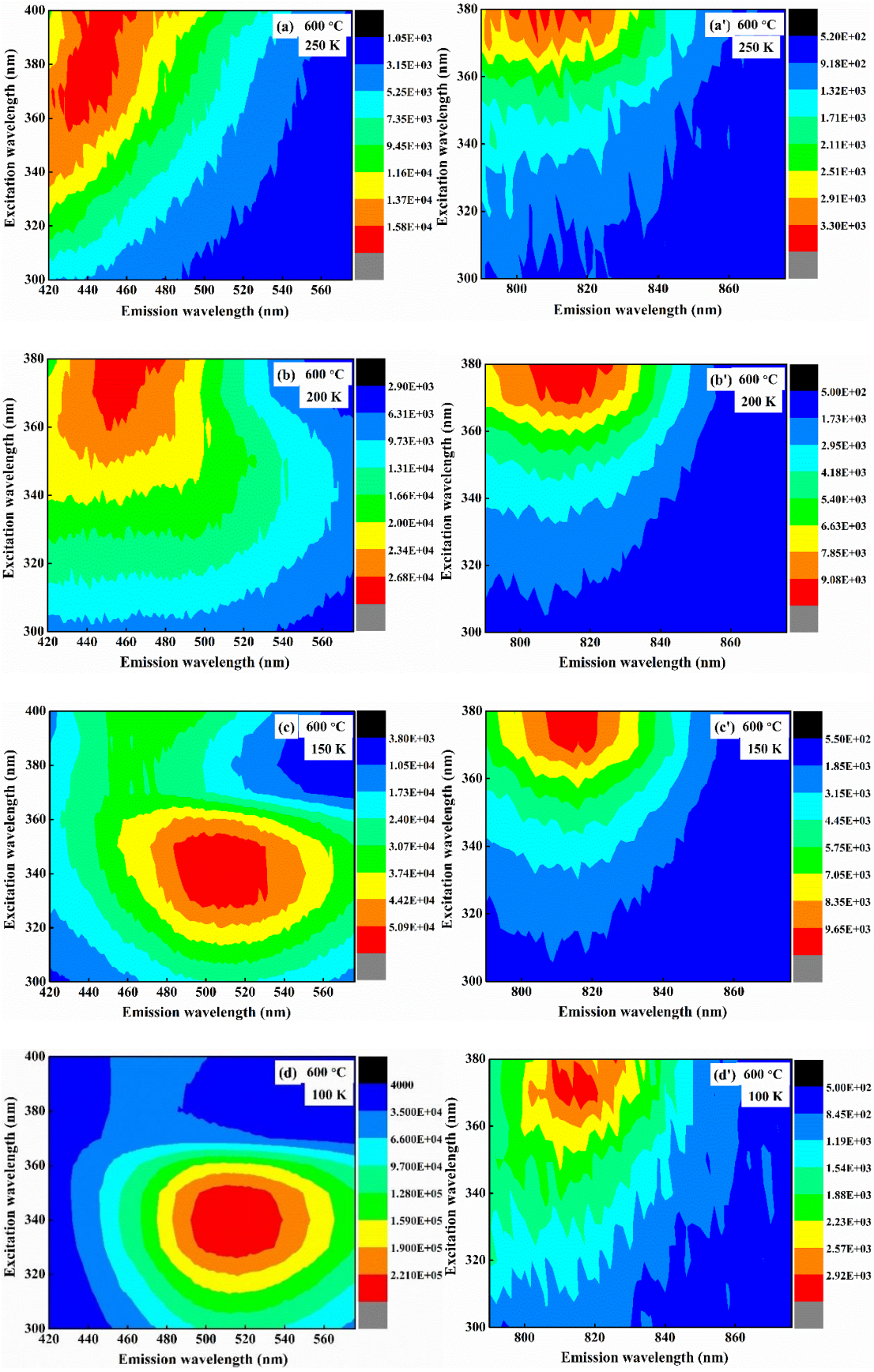

Figure 5.7(2). The photoluminescence contour map images of mixed-phase of TiO_2 NPs (600 °C) at a varying temperature from 290 K to 77 K.

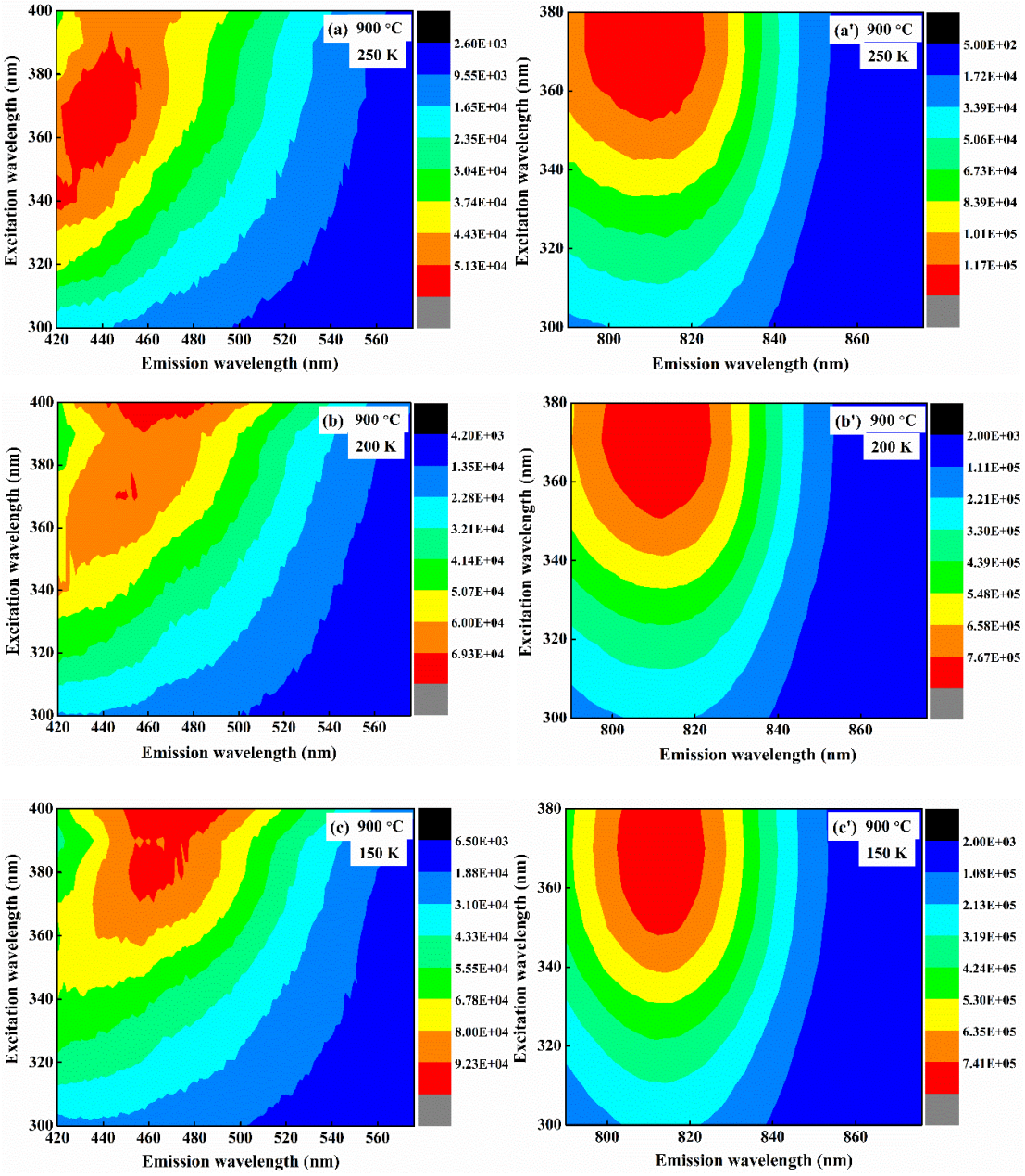

Figure 5.7(3). The photoluminescence contour map images of the rutile phase of TiO_2 NPs (900 °C) obtained at a varying temperature from 290 K to 77 K.

The Commission International de I'Eclairage (CIE) chromaticity plots were estimated from TD-PL spectra of TiO_2 NPs under the excitation wavelength 340 nm. The CIE plots and calculated CIE chromaticity coordinates are presented in Figure 5.8 and listed in Table 5.1. It can be seen from Figure 5.8 that the CIE coordinates are shifted from the

blue region to green as temperature decreases from 290 K to 77 K, indicating that PL of the NPs originated/shifted from shorter to longer wavelength region.

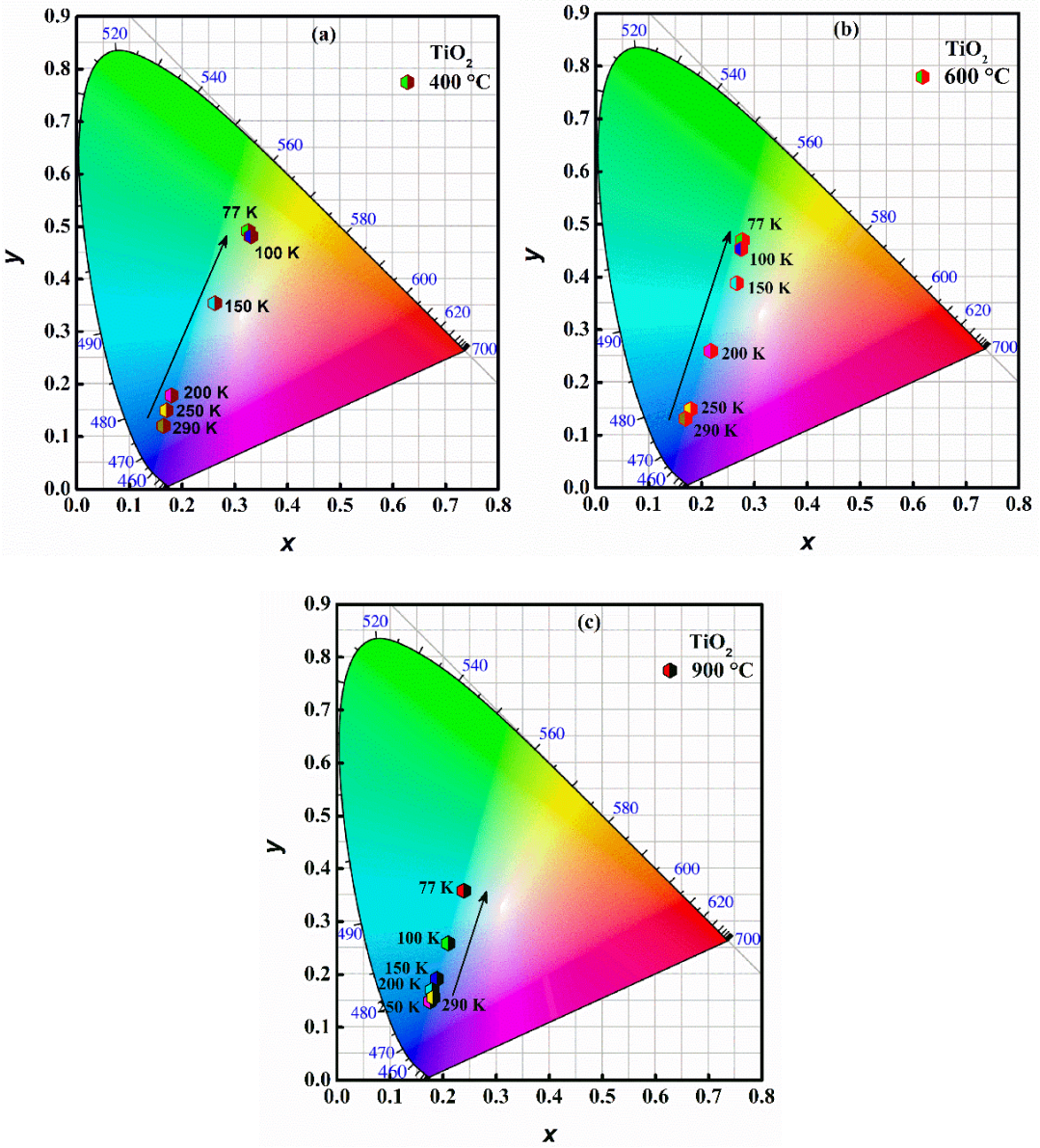

Figure 5.8. CIE diagrams of TiO_2 NPs formed at 400 °C (a), 600 °C (b) and 900 °C (c). Excitation wavelength (λ_{ex}) = 340 nm.

Table 5.1. The calculated values of the CIE chromaticity coordinate with excitation λ_{ex} = 340 nm at various temperatures of different phases of TiO_2 formed at 400 °C, 600 °C and 900 °C.

Samples	**CIE Color Coordinates (x, y) measurement at various temperature**					
	77 K	**100 K**	**150 K**	**200 K**	**250 K**	**290 K**
Anatase (400 °C)	(0.326,0.492)	(0.331,0.482)	(0.262,0.354)	(0.180,0.179)	(0.171,0.150)	(0.165,0.121)
Mixed (600 °C)	(0.277,0.470)	(0.275,0.453)	(0.267,0.389)	(0.218,0.259)	(0.179,0.149)	(0.170,0.131)
Rutile (900 °C)	(0.239,0.358)	(0.209,0.258)	(0.188,0.191)	(0.179,0.170)	(0.176,0.149)	(0.182,0.156)

5.6 Temperature-dependent time-resolved photoluminescence

The PL decay curves of different TiO_2 NPs (powder) phases were collected and at the peak PL wavelength with the excitation wavelength of (λ_{ex}) 340 nm generated from DeltaDiode and flash lamps. The acquired decays could be fitted well with mono and bi-exponential functions depending on the monitoring wavelengths and temperature. The decay curves fitted with the exponential function as shown in Eq. (5.1) [45–47]:

$$f(t) = \sum_i A_i \exp\left(-\frac{t}{\tau_i}\right), \quad (5.1)$$

where A_i and τ_i clarifies the pre-exponential factors and lifetime components, respectively. The average lifetime (τ_{av}) calculated using Eq. (5.2) [48]:

$$\tau_{av} = \sum_i \frac{A_i \tau_i^2}{A_i \tau_i}, \quad (5.2)$$

At 430 nm, when excited with a flash lamp, the PL decay is single exponential with a lifetime component of 3 – 4 μs for all the phases of TiO_2 (Tables 5.2 – 5.4). Upon decreases temperature, from 290 K to 77 K, the lifetime of anatase and rutile phases increases slightly up to 5 μs, whereas the lifetime of mixed-phase increases gradually and becomes 25 μs at 77 K (Table 5.3), indicating the decrease of non-radiative rates. However, when excited

with a 340 nm (Delta Diode), a dominant lifetime component of <10 ps along with two more lifetime components of about 38-41 ns and 2-3 ns exists, though the contribution of both the longer lifetimes is less than 1%, indicating to the presence of defect states. The typical fitted PL decay curves of three different phases of TiO_2 NPs obtained with 340 nm are shown in Figure 5.9.

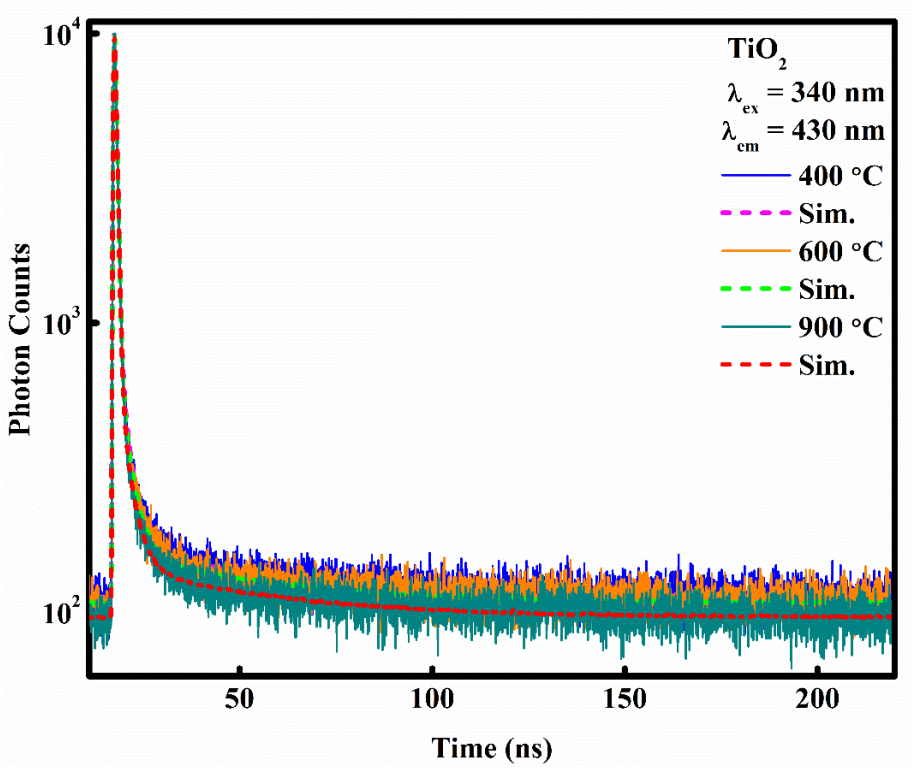

Figure 5.9. The simulated decay profiles of TiO_2 NPs obtained at room temperature with excitation wavelength (λ_{ex}) of 340 nm. PL wavelength, λ_{em} was 430 nm.

It has been mentioned that when the pulse laser is used, the decay process of the TiO_2 NPs is swift. Fujihara *et al.* [49] demonstrated the decay processes of TiO_2 NPs (anatase & rutile phase) got complete in the nanosecond time range when suspended in aqueous solutions. Harada *et al.* [50] illustrated that even at 10 K, the lifetime of both the phases (anatase and rutile) are for few nanoseconds or less than 2 µs. However, with the excitation of flash lamps, long lifetimes of milliseconds are observed, demonstrating that the PL mechanism is strongly linked to the trap states influenced by weak excitation. This

is considered because trap states first capture photogenerated electrons and holes under weak excitation conditions. Then the recombination of the non-radiative or radiative charge carriers results in the trap state emission.

Table 5.2. PL lifetimes (τ) of anatase phase of TiO_2 at different temperatures with excitation (λ_{ex}) of 340 nm.

Sample at	**λ_{em} (nm)**	$\boldsymbol{\tau_1(ms)}$
77 K	420	0.0048 ± 0.0002
100 K	420	0.0047 ± 0.0002
150 K	420	0.0045± 0.0001
200 K	420	0.0045± 0.0002
250 K	420	0.0044± 0.0001
290 K	420	0.0041± 0.0001

Table 5.3. PL lifetimes (τ) of mixed-phase of TiO_2 at different temperatures with excitation (λ_{ex}) of 340 nm.

Sample at	**λ_{em} (nm)**	$\boldsymbol{\tau_1(ms)}$
77 K	420	0.025 ± 0.002
100 K	420	0.007 ± 0.001
150 K	420	0.005 ± 0.001
200 K	420	0.004 ± 0.001
250 K	420	0.004 ± 0.001
290 K	420	0.003± 0.001

The recombination rate increases because of the trap-filling effect when pulsed laser light is used as an excitation source [51,52]. The photoinduced charge carriers are instantly trapped and occupy states inside the particle, increasing the charge carrier's mobility and enhancing the recombination rate. Hence, under the influence of weak excitation, the trap states play a unique role in the relaxation process of photoinduced carriers. In terms of energy levels or trap width, the trap states differ significantly. The depth of energy levels

of the trap states varies and influences how quickly the trapping happens and how much trap states live [53]. Therefore, the decay processes will sensitively represent the trap state properties of TiO_2 under the weak excitation condition.

Table 5.4. PL lifetimes (τ_i) and pre-exponential factors (A_i) of rutile phase of TiO_2 NPs at different temperatures with excitation (λ_{ex}) of 340 nm. The PL wavelengths were 420 and 530 nm.

Sample at	**λ_{em} (nm)**	$\boldsymbol{\tau_1(ms)}$
77 K	420	0.005 ± 0.001
100 K	420	0.005 ± 0.001
150 K	420	0.004 ± 0.001
200 K	420	0.004 ± 0.001
250 K	420	0.004 ± 0.001
290 K	420	0.004 ± 0.001

Sample at	**λ_{em} (nm)**	$\boldsymbol{\tau_1(ms)}$	$\boldsymbol{\tau_2(ms)}$	$\boldsymbol{A_1}$	$\boldsymbol{A_2}$	$\boldsymbol{\tau_{av}(ms)}$
77 K	530	0.046 ± 0.002	0.004 ± 0.001	0.193	0.807	0.046
100 K	530	0.007 ± 0.001	-	1.0	-	0.007
150 K	530	0.006 ± 0.001	-	1.0	-	0.006
200 K	530	0.005± 0.001	-	1.0	-	0.005
250 K	530	0.003 ± 0.001	-	1.0	-	0.003
290 K	530	0.0007± 0.0001	-	1.0	-	0.0007

In continuation of the PL of TiO_2 NPs originated at 530 and 820 nm at low temperatures, temperature-dependent time-resolved photoluminescence (TD-TRPL) decays were collected with 340 nm excitation by monitored at the peak PL wavelengths (530 nm and 820 nm) originated at temperatures from 290 K to 77 K. In the TiO_2 NPs, the properties of photogenerated carriers play an important role in the photochemical reaction. The mono and bi-exponential functions can simulate the observed decay curve well using Eqs. (5.1) and (5.2) are shown in Figure 5.10.

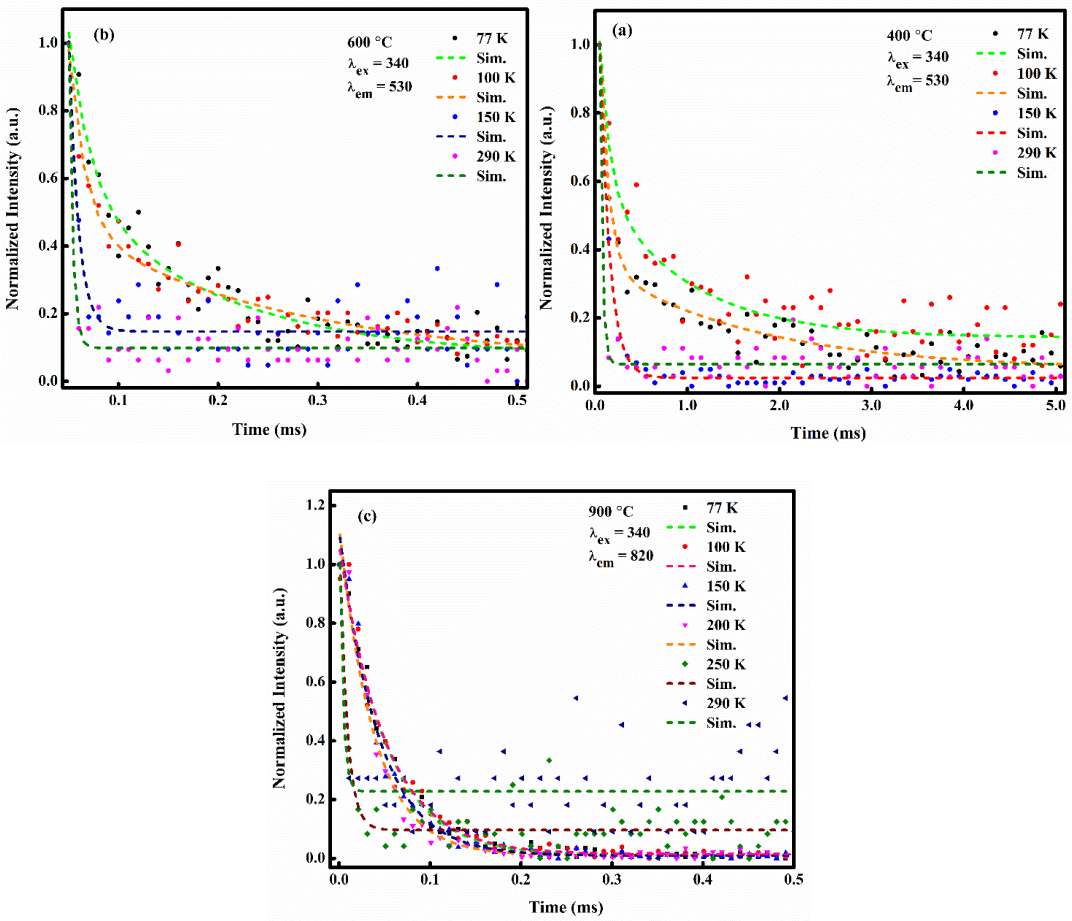

Figure 5.10. The simulated decay curves of different phases of TiO_2 NPs formed at 400 °C (a), 600 °C (b) and 900 °C (c) observed at the varying temperature from 290 K to 77 K monitored at PL wavelength of 530 nm and 820 nm with the excitation wavelength of 340 nm.

Figure 5.10 (a,b,c) shows TD-TRPL decay curves of anatase, mixed, and rutile phases of the TiO_2 NPs, which were monitored at the PL wavelength 530 nm and 820 nm with excited by 340 nm wavelength. The decay curves simulated by considering mono- and bi-exponential functions and the simulated results are shown in Tables 5.4 – 5.6. For the anatase and mixed phases of TiO_2 NPs, the mono-exponential lifetime with 0.004 ms at 290 K becomes longer as the measurement temperature lowered to 77 K, which corresponds to the increase of PL intensity. This suggests that trap states in both phases (anatase and mixed) of TiO_2 have a shallow depth. As a consequence, ambient temperature has a substantial impact on the trapped carriers.

Table 5.4. Photoluminescence lifetimes (τ_i) and pre-exponential factors (A_i) of anatase phase of TiO_2 (400 °C) with 340 nm excitation (λ_{ex}) at different temperatures.

Samples at	λ_{PL} **(nm)**	$\boldsymbol{\tau_1(ms)}$	$\boldsymbol{\tau_2(ms)}$	$\boldsymbol{A_1}$	$\boldsymbol{A_2}$	$\boldsymbol{\tau_{av}(ms)}$
77 K	530	0.016 ± 0.002	0.222 ± 0.017	0.958	0.042	0.0931
100 K	530	0.022 ± 0.005	0.150 ± 0.017	0.870	0.130	0.0868
150 K	530	0.009 ± 0.001	-	1.0	-	0.009
200 K	530	0.008 ± 0.001	-	1.0	-	0.008
250 K	530	0.005 ± 0.001	-	1.0	-	0.005
290 K	530	0.004 ± 0.001	-	1.0	-	0.004

Oxygen vacancies trap the carriers, and these recombinations contributed to the fast component of the decay in TiO_2 NPs. The TD-TRPL decays of both anatase and mixed-phase of the TiO_2 NPs have also been monitored at the peak PL wavelength 420 nm with excited by 340 nm wavelength and the decay curves simulated by the single exponential function. The lifetime increases slightly with lowing temperature for the anatase phase,

whereas it increases from 0.003 ms to 0.025 ms for mixed-phase TiO_2 NPs, increasing radiative recombination of the carries.

Table 5.5. Photoluminescence lifetimes (τ_i) and pre-exponential factors (A_i) of mixed-phase of TiO_2 (600 °C) with 340 nm excitation (λ_{ex}) at different temperatures.

Samples at	**λ_{PL} (nm)**	$\boldsymbol{\tau_1(ms)}$	$\boldsymbol{\tau_2(ms)}$	$\boldsymbol{A_1}$	$\boldsymbol{A_2}$	$\boldsymbol{\tau_{av}(ms)}$
77 K	530	0.016 ± 0.002	0.222 ± 0.017	0.958	0.042	0.0931
100 K	530	0.022 ± 0.005	0.150 ± 0.017	0.870	0.130	0.0868
150 K	530	0.009 ± 0.001	-	1.0	-	0.009
200 K	530	0.008 ± 0.001	-	1.0	-	0.008
250 K	530	0.005 ± 0.001	-	1.0	-	0.005
290 K	530	0.004 ± 0.001	-	1.0	-	0.004

Table 5.6. Photoluminescence lifetimes (τ_i) of rutile phase of TiO_2 (900 °C) with 340 nm excitation (λ_{ex}) at different temperatures.

Samples at	**λ_{PL} (nm)**	$\boldsymbol{\tau_1(ms)}$
77 K	820	0.050 ± 0.001
100 K	820	0.050 ± 0.001
150 K	820	0.043 ± 0.001
200 K	820	0.038± 0.002
250 K	820	0.008 ± 0.001
290 K	820	0.004 ± 0.003

Figure 5.10(c) shows the TD-TRPL decay curves of the rutile phased TiO_2 sample monitored at the peak PL wavelength 820 nm with excited by 340 nm wavelength. The

decay curves are fitted well with a single exponential function and the results are arranged in Table 5.6. As the temperature decreases from 290 K, the lifetime increases significantly from 0.004 ms to 0.050 ms, thus decreasing non-radiative recombination. It is to be considered that many shallow trap states in TiO_2 are found near the edge of the energy band, allowing them to catch exciting carriers more efficiently at high temperatures before relaxing to luminescent sites through trap-to-trap hopping [54].

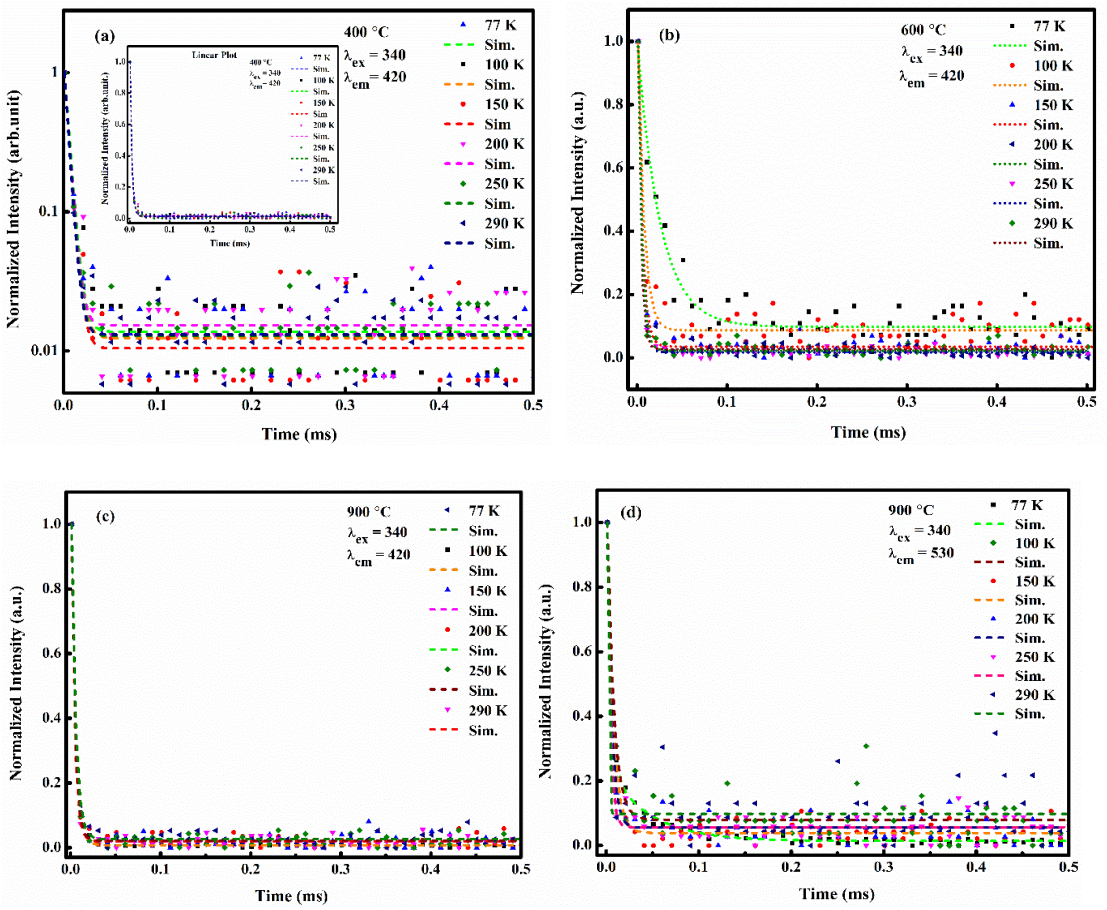

Figure 5.11. The simulated decay curves of different phases of TiO_2 NPs formed at 400 °C (a), 600 °C (b) and 900 °C (c,d) obtained at a varying temperature from 290 K to 77 K at 420 and 530 PL wavelength with excitation wavelength λ_{ex} = 340 nm.

The TD-TRPL spectra of the rutile phased TiO_2 sample were also monitored at the peak PL wavelength 420 nm and 530 nm excited by 340 nm wavelength. The decay curves were simulated with single and bi-exponential functions. The simulated decay curves and

lifetime parameters are shown in Figure 5.11 and Tables 5.2 – 5.4. The emission wavelengths were 420 nm and 530 nm, and the excitation wavelength was 340 nm.

5.7 Plausible dynamics of photogenerated charge carriers in different phases of TiO_2 NPs

With the change in the annealing temperature, the anatase crystalline structure of TiO_2 transforms into the rutile. The specific surface area decreases and the crystallinity increases dramatically through the transformation process, which results in the reduction in the number of defect states and a significant change in the trap state properties, as demonstrated in Figure 5.12. In the anatase phase of TiO_2, the visible PL band is generated by donor-acceptor recombination. The most common trapping sites for trapped electrons and holes are surface hydroxyl groups and oxygen vacancies [55,56]. The fast decay components have been observed in trapped charge carriers (electrons and holes). Some carriers were initially trapped by shallow defect states over trap-to-trap hopping before quenched to luminescent sites, resulting in a visible PL band [41,57]. These shallow-trap electrons are primarily responsible for the slow decay component anatase TiO_2 NPs [32].

The NIR PL band is obtained in the rutile phase of the TiO_2 NPs originated because of the recombination of electron-hole pairs at a deep trapped state. The origin of the trapped electrons aids the exponential component of the decay processes at the site of luminescence [58]. First, the additional electrons are seized by the non-radiative trap states and subsequently relax to the radiative centers via trap-to-trap hopping [40]. Indirect trap processes are responsible for the power-law component in rutile TiO_2 and these processes involve two paths. The first path consists of the quenching of the excited electrons to the lowest CB state and then relaxes to the luminescent centers via trap-to-trap hopping. Whereas in another path, the excited electrons with excess energy are captured directly by deep non-radiative trap states before settling to luminescent centers [41,57].

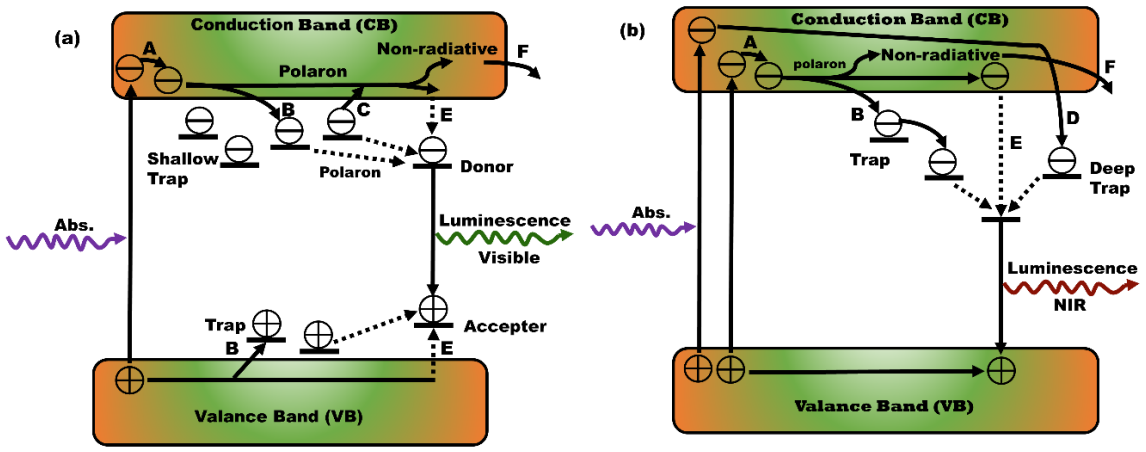

Figure 5.12. Schematic representation of relaxation processes of the photogenerated carriers in anatase phase (a) and rutile phase of TiO_2 (b). After excitation with 340 nm, the electrons jump to the conduction band where the different process involves, i.e., electrons quenched to the bottom of the conduction band (A), carriers captured by traps (B), thermal excitation from traps (C), electrons captured directly by deep traps (D), carriers relax to luminescent sites (E) and non-radiative recombination process (F).

Furthermore, the presence of the trap states heavily influences the photocatalytic properties of the anatase phase of TiO_2. Trapped carrier and slow decay process may take place to improve catalytic performance. In the mixed phase, the charge transfer process at the surface junction of anatase and rutile phases and the presence of trap states help to improve the photocatalytic activity. The shallow traps are ideal for separating the excited carriers and therefore stimulates photocatalytic activity [12,59,60]. On the other hand, the deep trap states present in the rutile phase, which produces the NIR PL, the energy levels do not favor photocatalytic reactions [59,60]; thus, satisfied and justified our previous work [3]. The photocatalytic performances of all three phases of TiO_2 with rhodamine B (RhB) dye have been discussed and found that both anatase and mixed-phases of TiO_2 NPs are efficient to degrade the RhB dye under UV light. Of which, the mixed-phase of NPs is most efficient for the degradation of dye. While the rutile phase of TiO_2 NPs does not have taken part in photocatalytic activity.

5.8 Conclusions

TiO_2 NPs have been synthesized by employing the sol-gel routes and annealed at a different temperature from 400 to 900 °C and three different types of the structure formed, i.e., anatase, mixed (anatase/rutile) and rutile phases. The results show that the phase changed from anatase to mixed to rutile with varying annealing temperatures. The specific surface area decreases and the crystallinity increases dramatically through the transformation process, a resultant reduction in the number of defect states and a significant change in the trap state properties. The structure and morphology of as-synthesized NPs were confirmed using XRD and FESEM analysis. The XRD analysis of TiO_2 NPs was carried out in the 290 K to 77 K temperature range and found no significant change in XRD patterns that means thermally stable TiO_2 NPs. The PL spectra and contour maps of TiO_2 NPs show that the anatase phase falls in the visible region. However, mixed and rutile phases fall in both visible and NIR regions as the temperature decreases from 290 K to 77 K. The visible PL band is ascribed to donor-acceptor recombination. In contrast, oxygen vacancies serve as donors and hydroxyl groups function as accepter sites. NIR emission band attributed to the trapped electrons in rutile TiO_2, which recombine with free holes and intrinsic defects. The fast component of the decay processes was aided by the immediate formation of trapped electrons in luminescence sites. The indirect trap processes were responsible for the power-law component, which was the recombination of trapped electrons formed via a deep trap state. It was observed that the electron-hole pairs thermally separated, preventing the formation of STEs directly. The PL and PL decay studies under weak excitation conditions prove to be a more valuable and appropriate method to evaluate the trap states distribution and their carrier dynamic effects, which were vibrant to understand the photocatalytic processes better.

References:

[1] H.G. Yang, C.H. Sun, S.Z. Qiao, J. Zou, G. Liu, S.C. Smith, H.M. Cheng, G.Q. Lu, Anatase TiO_2 single crystals with a large percentage of reactive facets, Nature. 453 (2008) 638–641.

[2] L. Liu, H. Zhao, J.M. Andino, Y. Li, Photocatalytic CO_2 reduction with H_2O on TiO_2 nanocrystals: Comparison of anatase, rutile, and brookite polymorphs and exploration of surface chemistry, ACS Catal. 2 (2012) 1817–1828.

[3] M. K. Singh, M.S. Mehata, Phase-dependent optical and photocatalytic performance of synthesized titanium dioxide (TiO_2) nanoparticles, Optik 193 (2019) 163011.

[4] L. Kumar, V. Ragunathan, M. Chugh, N. Bharadvaja, Nanomaterials for remediation of contaminants: a review, Environ. Chem. Lett. (2021).

[5] Y. Kim, S. Yang, E.H. Jeon, J. Baik, N. Kim, H.S. Kim, H. Lee, Enhancement of photo-oxidation activities depending on structural distortion of Fe-doped TiO_2 nanoparticles, Nanoscale Res. Lett. 11 (2016) 1–8.

[6] Y. Liang, S. Gan, S.A. Chambers, E.I. Altman, Surface structure of anatase TiO_2(001): Reconstruction, atomic steps, and domains, Phys. Rev. B - Condens. Matter Mater. Phys. 63 (2001) 1–7.

[7] H. Cheng, A. Selloni, Surface and subsurface oxygen vacancies in anatase TiO_2 and differences with rutile, Phys. Rev. B. 79 (2009) 092101.

[8] N.D. Abazović, L. Mirenghi, I.A. Janković, N. Bibić, D. V. Šojić, B.F. Abramović, M.I. Čomor, Synthesis and characterization of rutile TiO_2 nanopowders doped with iron ions, Nanoscale Res. Lett. 4 (2009) 518–525.

[9] M. K. Singh, M.S. Mehata, Enhanced photoinduced catalytic activity of transition metal ions incorporated TiO_2 nanoparticles for degradation of organic dye: Absorption and photoluminescence spectroscopy, Opt. Mater. 109 (2020) 110309.

[10] T. Ohno, K. Tokieda, S. Higashida, M. Matsumura, Synergism between rutile and anatase TiO_2 particles in photocatalytic oxidation of naphthalene, Appl. Catal. A Gen. 244 (2003) 383–391.

[11] Q. Xu, Y. Ma, J. Zhang, X. Wang, Z. Feng, C. Li, Enhancing hydrogen production activity and suppressing CO formation from photocatalytic biomass reforming on Pt/TiO_2 by optimizing anatase-rutile phase structure, J. Catal. 278 (2011) 329–335.

[12] J. Zhang, Q. Xu, Z. Feng, M. Li, C. Li, Importance of the relationship between surface phases and photocatalytic activity of TiO_2, Angew. Chemie - Int. Ed. 47 (2008) 1766–1769.

[13] X. Zhang, Y. Lin, D. He, J. Zhang, Z. Fan, T. Xie, Interface junction at anatase/rutile in mixed-phase TiO_2: Formation and photogenerated charge carriers properties, Chem. Phys. Lett. 504 (2011) 71–75.

[14] X. Sun, W. Dai, G. Wu, L. Li, N. Guan, M. Hunger, Evidence of rutile-to-anatase photoinduced electron transfer in mixed-phase TiO_2 by solid-state NMR spectroscopy, Chem. Commun. 51 (2015) 13779–13782.

[15] G. Li, C. P. Richter, R. L. Milot, L. Cai, C. A. Schmuttenmaer, R. H. Crabtree, G. W. Brudvig, V.S. Batista, Synergistic effect between anatase and rutile TiO_2 nanoparticles in dye-sensitized solar cells, Dalton Trans. (2009) 10078–10085.

[16] D. C. Hurum, A.G. Agrios, K.A. Gray, T. Rajh, M.C. Thurnauer, Explaining the enhanced photocatalytic activity of Degussa P25 mixed-phase TiO_2 using EPR, J. Phys. Chem. B. 107 (2003) 4545–4549.

[17] D.O. Scanlon, C.W. Dunnill, J. Buckeridge, S.A. Shevlin, A.J. Logsdail, S.M. Woodley, C.R.A. Catlow, M.J. Powell, R.G. Palgrave, I.P. Parkin, G.W. Watson, T.W. Keal, P. Sherwood, A. Walsh, A.A. Sokol, Band alignment of rutile and anatase TiO_2, Nat. Mater. 12 (2013) 798–801.

[18] V. Pfeifer, P. Erhart, S. Li, K. Rachut, J. Morasch, J. Brötz, P. Reckers, T. Mayer, S. Rühle, A. Zaban, I. Mora Seró, J. Bisquert, W. Jaegermann, A. Klein, Energy band alignment between anatase and rutile TiO_2, J. Phys. Chem. Lett. 4 (2013) 4182–4187.

[19] L. Jing, S. Li, S. Song, L. Xue, H. Fu, Investigation on the electron transfer between anatase and rutile in nano-sized TiO_2 by means of surface photovoltage technique and its effects on the photocatalytic activity, Sol. Energy Mater. Sol. Cells. 92 (2008) 1030–1036.

[20] K. Komaguchi, H. Nakano, A. Araki, Y. Harima, Photoinduced electron transfer from anatase to rutile in partially reduced TiO_2 (P-25) nanoparticles: An ESR study, Chem. Phys. Lett. 428 (2006) 338–342.

[21] S. Shen, X. Wang, T. Chen, Z. Feng, C. Li, Transfer of photoinduced electrons in anatase-rutile TiO_2 determined by time-resolved mid-infrared spectroscopy, J. Phys. Chem. C. 118 (2014) 12661–12668.

[22] T. Kawahara, Y. Konishi, H. Tada, N. Tohge, J. Nishii, S. Ito, A patterned TiO_2 (Anatase)/TiO_2 (Rutile) bilayer-type photocatalyst: Effect of the anatase/rutile junction on the photocatalytic activity, Angew. Chem. 114 (2002) 2935-2937.

[23] S. T. Martin, H. Herrmann, W. Choi, M. R. Hoffmann, Time-resolved microwave conductivity. Part 1.-TiO_2 photoreactivity and size quantization J. Chem. Soc., Faraday Trans. 90 (1994) 3315-3322.

[24] M.R. Hoffmann, S.T. Martin, W. Choi, D.W. Bahnemann, Environmental applications of semiconductor photocatalysis, Chem. Rev. 95 (1995) 69–96.

(ii) [25] S. T. Martin, H. Herrmann, W. Choi, M. R. Hoffmann, Time-resolved microwave conductivity. Part 2.- Quantum-sized TiO_2 and the effect of adsorbates and light intensity on charge-carrier dynamics J. Chem. Soc., Faraday Trans. 90 (1994) 3323-3330.

[26] W. F. Zhang, M.S. Zhang, Z. Yin, Q. Chen, Photoluminescence in anatase titanium dioxide nanocrystals, Appl. Phys. B Lasers Opt. 70 (2000) 261–265.

[27] D.K. Pallotti, L. Passoni, P. Maddalena, F. Di Fonzo, S. Lettieri, Photoluminescence mechanisms in anatase and rutile TiO_2, J. Phys. Chem. C 121 (2017) 9011–9021

[28] S. Lettieri, M. Pavone, A. Fioravanti, L.S. Amato, P. Maddalena, Charge carrier processes and optical properties in TiO_2 and TiO_2-based heterojunction photocatalysts: A review, Materials 14 (2021) 1645.

[29] C. P. Saini, A. Barman, D. Banerjee, O. Grynko, S. Prucnal, M. Gupta, D.M. Phase, A.K. Sinha, D. Kanjilal, W. Skorupa, A. Kanjilal, Impact of self-trapped excitons on blue photoluminescence in TiO_2 nanorods on chemically etched Si Pyramids, J. Phys. Chem. C. 121 (2017) 11448–11454.

[30] R. Brüninghoff, K. Wenderich, J.P. Korterik, B.T. Mei, G. Mul, A. Huijser, Time-dependent photoluminescence of nanostructured anatase TiO_2 and the role of bulk and surface processes, J. Phys. Chem. C. 123 (2019) 26653–26661.

[31] Y. Yamada, Y. Kanemitsu, Determination of electron and hole lifetimes of rutile and anatase TiO_2 single crystals, Appl. Phys. Lett. 101 (2012) 133907.

[32] L. Cavigli, F. Bogani, A. Vinattieri, V. Faso, G. Baldi, Volume versus surface-mediated recombination in anatase TiO_2 nanoparticles, J. Appl. Phys. 106 (2009) 053516.

[33] M. Watanabe, S. Sasaki, T. Hayashi, Time-resolved study of photoluminescence in anatase TiO_2, J. Lumin. 87 (2000) 1234–1236.

[34] M. Watanabe, T. Hayashi, H. Yagasaki, S. Sasaki, Luminescence process in anatase TiO_2 studied by time-resolved spectroscopy, Int. J. Mod. Phys. B. 15 (2001) 3997–4000.

[35] M. Watanabe, T. Hayashi, Time-resolved study of self-trapped exciton luminescence in anatase TiO_2 under two-photon excitation, J. Lumin. 112 (2005) 88–91.

[36] M.K. Singh, M.S. Mehata, Temperature-dependent photoluminescence and decay times of different phases of grown TiO2 nanoparticles: Carrier dynamics and trap states, Ceramics International 2021.

[37] N. Patra, A. Biswas, C.L. Prajapat, A. Ghosh, P.U. Sastry, S. Tripathi, P.D. Babu, A. Biswas, S.N. Jha, D. Bhattacharyya, Structural and magnetic characterization of the $Ni_{55}Fe_{19}Ga_{26}$ shape memory alloy thin film, J. Alloys Compd. 723 (2017) 1098–1112.

[38] S. Dai, Y. Wu, T. Sakai, Z. Du, H. Sakai, M. Abe, Preparation of highly crystalline TiO_2 nanostructures by acid-assisted hydrothermal treatment of hexagonal-structured nanocrystalline titania/cetyltrimethyammonium bromide nanoskeleton, Nanoscale Res. Lett. 5 (2010) 1829–1835.

[39] H. A. Mahmoud, K. Narasimharao, T.T. Ali, K.M.S. Khalil, Acidic peptizing agent effect on anatase-rutile ratio and photocatalytic performance of TiO_2 nanoparticles, Nanoscale Res. Lett. 13 (2018) 01-13.

[40] J. Shi, J. Chen, Z. Feng, T. Chen, Y. Lian, X. Wang, C. Li, Photoluminescence characteristics of TiO_2 and their relationship to the photoassisted reaction of water/methanol mixture, J. Phys. Chem. C. 111 (2007) 693–699.

[41] X. Wang, Z. Feng, J. Shi, G. Jia, S. Shen, J. Zhou, C. Li, Trap states and carrier dynamics of TiO_2 studied by photoluminescence spectroscopy under weak

excitation condition, Phys. Chem. Chem. Phys. 12 (2010) 7083–7090.

[42] Y. Wang, N. Herron, Photoluminescence and relaxationn dynamics of CdS superclusters in zeolites, J. Phys. Chem. 92 (1988) 4988–4994.

[43] C. Ye, X. Fang, M. Wang, L. Zhang, Temperature-dependent photoluminescence from elemental sulfur species on ZnS nanobelts, J. Appl. Phys. 99 (2006) 063504.

[44] P. Jing, J. Zheng, M. Ikezawa, X. Liu, S. Lv, X. Kong, J. Zhao, Y. Masumoto, Temperature-dependent photoluminescence of CdSe-Core CdS/CdZnS/ZnS-multishell quantum dots, J. Phys. Chem. C 113 (2009) 13545–13550.

[45] V. Sharma, M. S. Mehata, Synthesis of photoactivated highly fluorescent Mn^{2+}-doped ZnSe quantum dots as effective lead sensor in drinking water, Mater. Res. Bull. 134 (2021) 111121.

[46] P. Sharma, M.S. Mehata, Rapid sensing of lead metal ions in an aqueous medium by MoS_2 quantum dots fluorescence turn-off, Mater. Res. Bull. 131 (2020) 110978.

[47] V. Sharma, M.S. Mehata, Rapid optical sensor for recognition of explosive 2,4,6-TNP traces in water through fluorescent ZnSe quantum dots, Spectrochim. Acta Part A Mol. Biomol. Spectrosc. 260 (2021) 119937.

[48] P. Sharma, M.S. Mehata, Colloidal MoS_2 quantum dots based optical sensor for detection of 2,4,6-TNP explosive in an aqueous medium, Opt. Mater. 100 (2020) 109646.

[49] K. Fujihara, S. Izumi, T. Ohno, M. Matsumura, Time-resolved photoluminescence of particulate TiO_2 photocatalysts suspended in aqueous solutions, J. Photochem. Photobiol. A Chem. 132 (2000) 99–104.

[50] N. Harada, M. Goto, K. Iijima, H. Sakama, N. Ichikawa, H. Kunugita, K. Ema, Time-resolved luminescence of TiO_2 powders with different crystal structures, Japanese J. Appl. Physics, Part 1 Regul. Pap. Short Notes Rev. Pap. 46 (2007) 4170–

4171.

[51] T. Yoshihara, R. Katoh, A. Furube, Y. Tamaki, M. Murai, K. Hara, S. Murata, H. Arakawa, M. Tachiya, Identification of reactive species in photoexcited nanocrystalline TiO_2 films by wide-wavelength-range (400-2500 nm) transient absorption spectroscopy, J. Phys. Chem. B. 108 (2004) 3817–3823.

[52] A. V. Barzykin, M. Tachiya, Mechanism of charge recombination in dye-sensitized nanocrystalline semiconductors: Random flight model, J. Phys. Chem. B. 106 (2002) 4356–4363.

[53] J. Z. Zhang, Interfacial charge carrier dynamics of colloidal semiconductor nanoparticles, J. Phys. Chem. B. 104 (2000) 7239–7253.

[54] H. Zhao, Q. Zhang, Y.X. Weng, Deep surface trap filling by photoinduced carriers and interparticle electron transport observed in TiO_2 nanocrystalline film with time-resolved visible and mid-IR transient spectroscopies, J. Phys. Chem. C. 111 (2007) 3762–3769.

[55] B. Choudhury, M. Dey, A. Choudhury, Shallow and deep trap emission and luminescence quenching of TiO_2 nanoparticles on Cu doping, Appl. Nanosci. 4 (2014) 499–506. B. Choudhury, M. Dey, A. Choudhury, Shallow and deep trap emission and luminescence quenching of TiO_2 nanoparticles on Cu doping, Appl. Nanosci. 4 (2014) 499–506.

[56] S.G. Kumar, L.G. Devi, Review on modified TiO_2 photocatalysis under UV/visible light: Selected results and related mechanisms on interfacial charge carrier transfer dynamics, J. Phys. Chem. A. 115 (2011) 13211–13241.

[57] X. Wang, S. Shen, Z. Feng, C. Li, Time-resolved photoluminescence of anatase/rutile TiO_2 phase junction revealing charge separation dynamics, Cuihua Xuebao/Chinese J. Catal. 37 (2016) 2059–2068.

[58] J.J.M. Vequizo, S. Kamimura, T. Ohno, A. Yamakata, Oxygen induced enhancement of NIR emission in brookite TiO_2 powders: Comparison with rutile and anatase TiO_2 powders, Phys. Chem. Chem. Phys. 20 (2018) 3241–3248.

[59] L. Zhang, H.H. Mohamed, R. Dillert, D. Bahnemann, Kinetics and mechanisms of charge transfer processes in photocatalytic systems: A review, J. Photochem. Photobiol. C Photochem. Rev. 13 (2012) 263–276.

[60] R. Qian, H. Zong, J. Schneider, G. Zhou, T. Zhao, Y. Li, J. Yang, D.W. Bahnemann, J.H. Pan, Charge carrier trapping, recombination and transfer during TiO_2 photocatalysis: An overview, Catal. Today. 335 (2019) 78–90.

Chapter-6

Electroabsorption spectroscopy of molybdenum disulfide thin-film*

6.1 Introduction

Two-dimensional (2D) layered materials have always been fascinated the scientific community due to their distinct properties such as high electron mobility, superior heat conductivity, excellent electrical conductivity and physical properties [1–4]. Graphene is the most popular 2D material and holds great potential for numerous applications. Despite these extravagant properties, the zero-band gap of graphene restricts its direct application in various electronic and optoelectronic devices [5]. Due to these constraints, the researchers, moved towards the 2D semiconductor materials such as molybdenum disulfide (MoS_2), which could overcome the drawbacks of graphene in electronic and optoelectronic devices.

The MoS_2 is a 2D transition metal dichalcogenide formed through the atomic layer of molybdenum sandwiched between two sulfur atom layers. In MoS_2 nanosheets (NSs), there is a strong intra-layer covalent bonding of Mo atoms with the S atoms in a trigonal prismatic arrangement. The hexagonal plane of molybdenum atoms is sandwiched between two hexagonal planes of sulfur atoms and its interlayer stacking are strengthened with weak van der Waals forces [6,7]. The interlayer coordination of 2D MoS_2 comprised of the weak Van der walls forces enables the formation of the monolayer MoS_2 NS. The thickness of the monolayer MoS_2 is 0.65 nm.

---

* Contents of this chapter has been published in **The Journal of Physical Chemistry: C, 2021 (Manuscript Accepted)**

Bulk MoS_2 crystal is an indirect bandgap semiconductor material with several S-Mo-S layers and switched to the direct bandgap when brought to the monolayer. It has a tunable bandgap when the film exfoliates from layers (~1.2 eV) to a single layer (~1.8 eV) [8,9]. The tunable bandgap with few layers to monolayer facilitates photoluminescence (PL) characteristics in MoS_2 NSs and could be employed in various optoelectronic, catalytic and sensing applications [10–13]. MoS_2 is used as photocatalysts because of its optical bandgap, which falls in the visible region and overcomes the shortcoming of other renowned photocatalysts, like metal oxides (TiO_2, ZnO, SnO_2, etc.) [14]. As the application of most of the catalysts are limited to the UV range (UV region, which possesses only 5% of total sunlight) hence limiting their direct use to the real world [15,16].

Although the optical properties of MoS_2 NSs have been studied over the years, theoretical and experimental. External electric-field effect on absorption has been used to study the electronic structure, in addition to excited-state dynamics following photoexcitation, including electron and/or hole mobility [17–19]. Vella *et al.* [20] have reported electroabsorption (E-A) spectra of MoS_2 monolayer by fabricating transistor (using c-plane sapphire as the transparent substrate) with ITO as the transparent back-gate electrode and Ti/Au as a source and drain electrodes. The E-A analysis with the derivative method has been discussed at a different gate voltage of transistors. The exciton band 'A' observed at 1.9 eV consists of two electronic resonance bands, namely A^0 and A^-.

In the present study, MoS_2 nanosheets were manufactured using a hydrothermal method and embedded in a PMMA thin film. The XRD and TEM analysis confirmed the crystalline and layered structure of MoS_2 nanosheets. Temperature-dependent absorption and electroabsorption (E-A) spectra of MoS_2 thin film have been measured. The effect of external electric field on the absorption spectra is discussed and the change in polarizability ($\Delta\bar{\alpha}$) and electric dipole moment ($|\Delta\mu|$) between the transition states are estimated.

6.2 Experimental section

All reagents were of AR (analytically pure) grade and received from Sigma Aldrich. The ammonium heptamolybdate tetrahydrate (AHM) was used as a precursor and primary source of Mo. Thioacetamide (TAA) was taken as a sulfur source for the synthesis of the required compound. Also, citric acid (CA) was used to reducing reagents. Polymethyl methacrylate (PMMA) was also obtained from Sigma Aldrich and purified before preparing MoS_2 NSs doped thin film through tetrahydrofuran (THF). A fluorine-doped tin oxide (FTO) coated glass substrates were used.

MoS_2 NSs were synthesized by dissolving 0.5 g of ammonium molybdate as Mo source in de-ionized (DI) water with 0.2 g of citric acid for reducing Mo from Mo^{+6} to Mo^{+4} state. The above mixture is allowed to stir for 2 h at room temperature and afterward, 0.5 g of thioacetamide as S source is added to the mixture. Then, the mixture was transferred to the Teflon line autoclave at 200 ℃ for 24 h and cool down to room temperature naturally. Finally, the obtained black precipitates were washed at 8000 rpm for 30 min with deionized (DI) water and ethanol. The black powder sample was kept in a hot air oven at 60 ℃ for 12 h for drying and the final product as MoS_2 NSs were obtained [21].

To prepare the solid thin film of MoS2 NSs for the application of external electric field, i.e., for the measurement of E-A spectra, a certain amount of MoS2 NSs and PMMA (poly (methyl methacrylate)) were mixed in a selected volume of THF. After making a homogeneous mixture, it was spin-coated at fixed rpm over an FTO-coated glass plate. The FTO was pre-etched for about a quarter of its length before spin coating. The thickness of the MoS2 doped thin film over the FTO substrate came out to be typically 0.42 μm, as recorded by an alpha step profiler (Veeco Dektak 150). The thickness of the film (d) is used to assess the applied field strength (F) by dividing the applied voltage (V). The FTO layer serves as an electrode. For the other electrode, an aluminum (Al) film thickness of about

20 nm was deposited over the MoS2 thin film with thermal evaporation techniques. This semi-transparent aluminum (Al) film and FTO layer serve as electrodes for the E-A measurements. The schematic representation of the synthesis of MoS_2 NSs and thin-film preparation is shown in Figure 6.1.

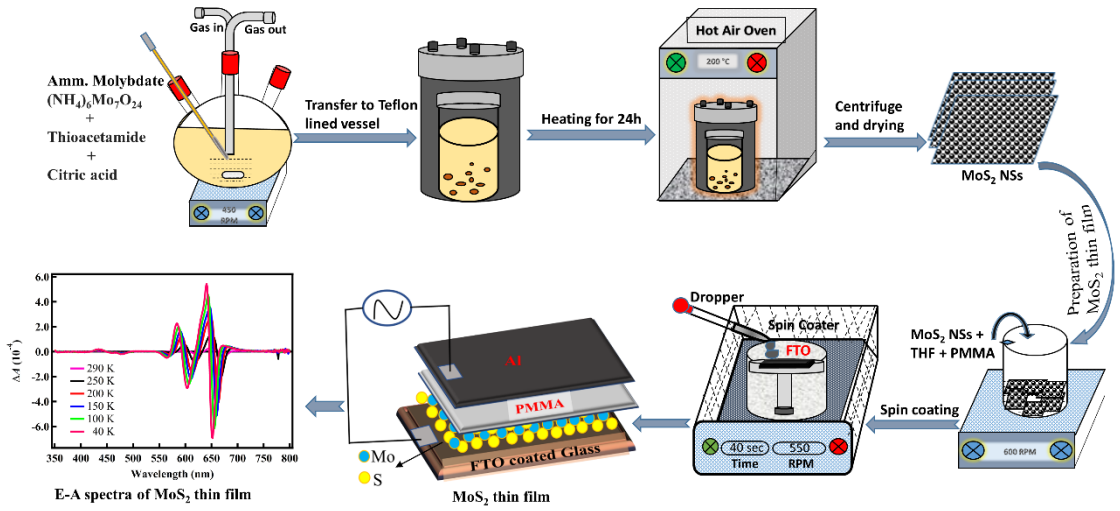

Figure 6.1. The schematic representation of the synthesis of MoS_2 NSs thin film.

All the optical measurements were recorded under vacuum conditions. The absorption spectra of MoS_2 NSs doped in a PMMA thin film were measured with a Jasco, FP- 777 spectrophotometer using an external PMT. For the E-A measurement, a modulated external electric field was applied to the sample film, which was simultaneously shined by the 150 W continuous xenon lamp (from FP-777), incorporated and controlled altogether in the apparatus, as described elsewhere [22]. The temperature-dependent E-A spectra were obtained by using Daikin, a V202C5LR cryogenic refrigerating system equipped with quartz optical windows. A temperature controller (Scientific Inst. model 9600) was used to control the sample film's temperature with a silicon diode thermometer attached to the sample. X-ray diffractometer (Bede D1 with CuKα radiation) was used to measure the X-ray diffraction (XRD) patterns of MoS_2 thin film at acceleration voltage and applied current of 40 kV and 50 mA, respectively. High resolution-transmission electron microscopy (HR-

TEM) images were recorded by TALOS (Thermo scientific instruments) with an accelerating 80-200 kV voltage.

6.3 Results and discussion

Figure 6.2 (a) shows the XRD pattern of the as-synthesized MoS_2 NSs thin film observed in the range of 10^o to 70^o at a varying temperature range of 290 - 40 K. The XRD pattern exhibits the hexagonal crystal structure of MoS_2, as demonstrated in Figure 6.2(b). No other impure phase was observed in the sample, indicating the formation of a pure hexagonal phase of MoS_2.

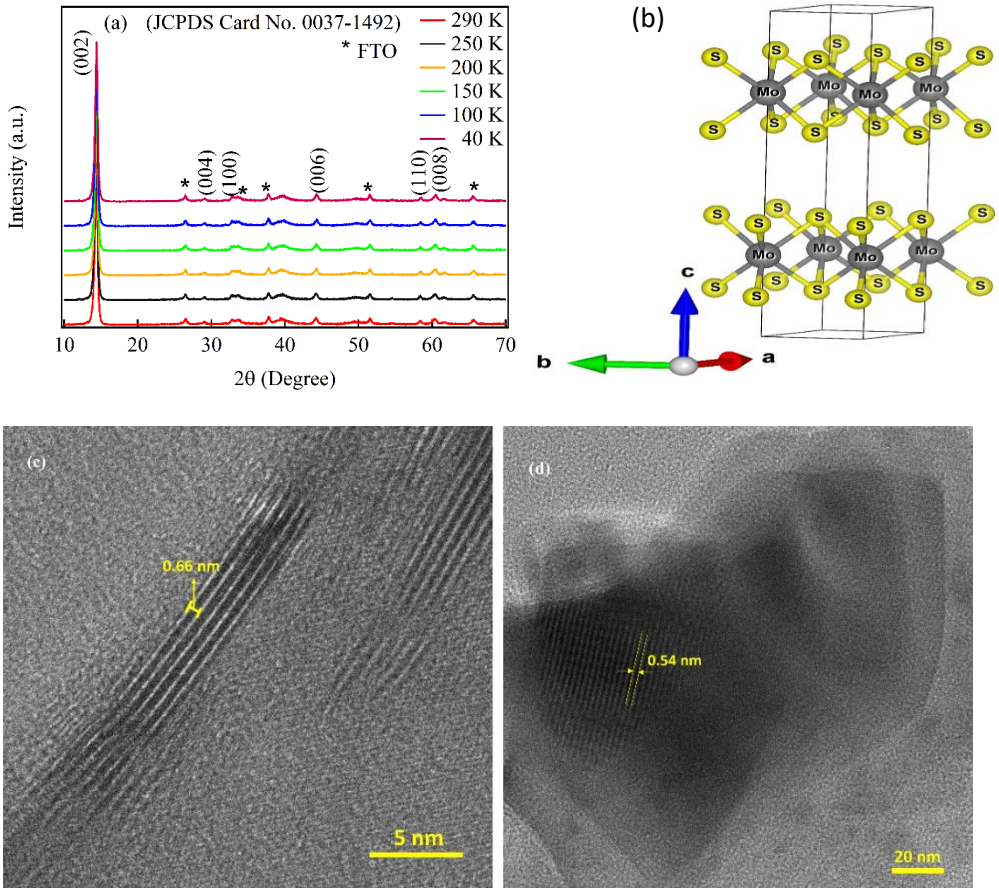

Figure 6.2. XRD patterns of MoS_2 NSs obtained at varying temperatures (a) and hexagonal crystal structure (b) and HRTEM images with lattice fringes (c, d).

The dominant peak of the MoS_2 crystal at $2\theta = 14.28^o$ designates the MoS_2 layers piled orderly along (002) direction with a d-spacing of 0.61 nm. The diffraction peaks of MoS_2 at $2\theta = 14.28^o$, 44.21^o, and 60.31^o show layered stacks along (002), (006) and (008)

planes. The (100) reflection at 32.58^{o} and (110) reflection at 58.18^{o} was observed in as-synthesized samples. As the temperature reduced from 290 K to 40 K, there is no variation in peak intensity and peak position of the XRD pattern of MoS_2 NSs, indicating no change in crystalline structure even at 40 K. The HRTEM images of MoS_2 NSs thin film (Figure 6.2(c)) proving the layered structure of MoS_2 NSs upto a few layers, which are well stacked with an interlayer distance of 0.66 nm separation. Similarly, Figure 6.2(d)) shows the ordered lattice fringes of MoS_2 NSs with a d-spacing of 0.54 nm corresponds to the (002) oriented crystal plane of the 2H-MoS_2 structure.

Figure 6.3(a) shows the absorption spectra of as-synthesized MoS_2 NSs doped in a thin PMMA film in the range of 12500-28580 cm^{-1} at various temperatures ranging from 290 to 40 K. At 290 K, four characteristic absorption peaks appeared and are designated as A, B, C and D excitonic bands (Figure 6.3a). The exciton peaks A and B, which are at 14663 cm^{-1} and 15573 cm^{-1} at 290 K, respectively, originated due to the spin-orbit splitting of interband excitonic transitions at the K point of the 2D Brillouin zone [23,24]. The absorption peaks C and D, which are at 21322 cm^{-1} and 24691 cm^{-1} at 290 K, respectively, arise from the interband transitions between the higher density of state regions, from the occupied d_{z2} orbital to the unoccupied d_{xy}, d_{x2-y2} and d_{xz}, d_{yz} orbitals [25,26]. The broadening in overall absorption bands, excitonic bands A, B, C and D, which are the characteristic peaks of MoS_2 NSs, may be due to the Mie scattering induced background [27]. Also, the non-uniform size distribution of the sheets may contribute to the broadening of the individual peaks.

When the temperatures decreased from 290 K to 40 K, the absorption bands A and B showed a blue shift, while the spectral shift was negligible for the C and D bands, as shown in Figure 6.3. The blue shifts with decreasing temperature could be due to a change

in the orbitals overlap, forming the band in the thermally expanded crystals [28]. Such transformation is considered very small for the C and D bands (Fig. 6.3a).

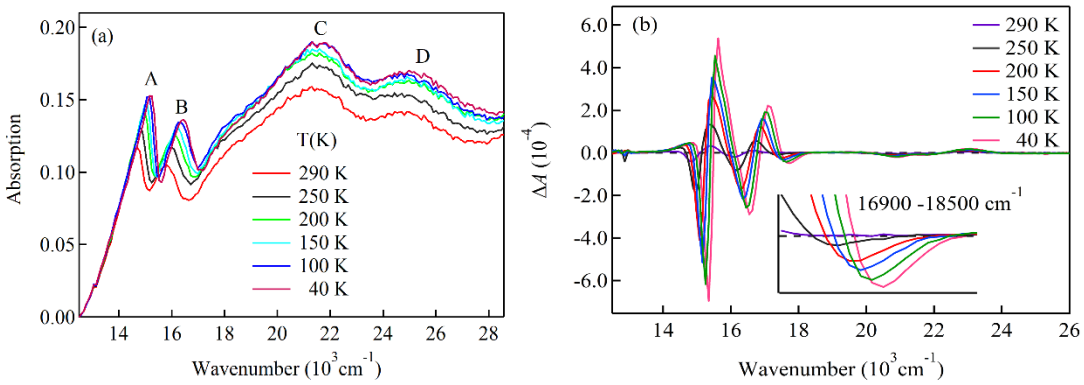

Figure 6.3. Absorption spectra (a) and E-A spectra (b) of MoS_2 thin-film obtained at different temperatures. Inset figure in (b) shows an extended view of the E-A spectra in the range of 16900 to 18500 cm^{-1}.

Figure 6.3 (b) shows the E-A spectra of as-synthesized MoS_2 NSs doped in a PMMA film measured at the second harmonic of the modulation frequency of applied electric field (1.0 kHz) at different temperatures (290 - 40 K) with a field strength of 0.5 $MVcm^{-1}$. The E-A signal is quite strong at room temperature for the excitonic resonance bands (A and B). The E-A signal intensity increased and the spectrum shifted towards the higher energy side as the temperature decreased. In contrast, no shift in the E-A spectrum was observed in the short wavelength region corresponding to the C and D bands, as shown in the inset of Figure 6.3b. A similar blue shift was also noticed in the absorption spectrum, i.e., for the A and B bands, with decreasing the temperature from 290 to 40 K. As the temperature decreased from 290 to 40 K, a new band appeared between 16900 to 18500 cm^{-1} and shifted towards higher energy and selectively shown in the inset Figure 6.3(b). The blue shift of the A and B bands in the absorption and as well as E-A spectra might be due to the lattice contraction nanosheets. E-A spectra of MoS_2 NSs at 290 and 40 K were measured with different applied field strengths in the range 0.1 - 0.5 $MVcm^{-1}$, and the results are shown in Figure 6.4(a) and (b), respectively. The E-A signal exhibit maxima at

15337 cm^{-1} and 15601 cm^{-1} and minima at 14859 cm^{-1} and 15347 cm^{-1} at 290 K and 40 K, respectively. The E-A signals at two different temperatures are proportional to the square of the applied electric field (Fig. 6.4(c,d)), indicating that the E-A signals of the excitonic bands originated from the Stark shift.

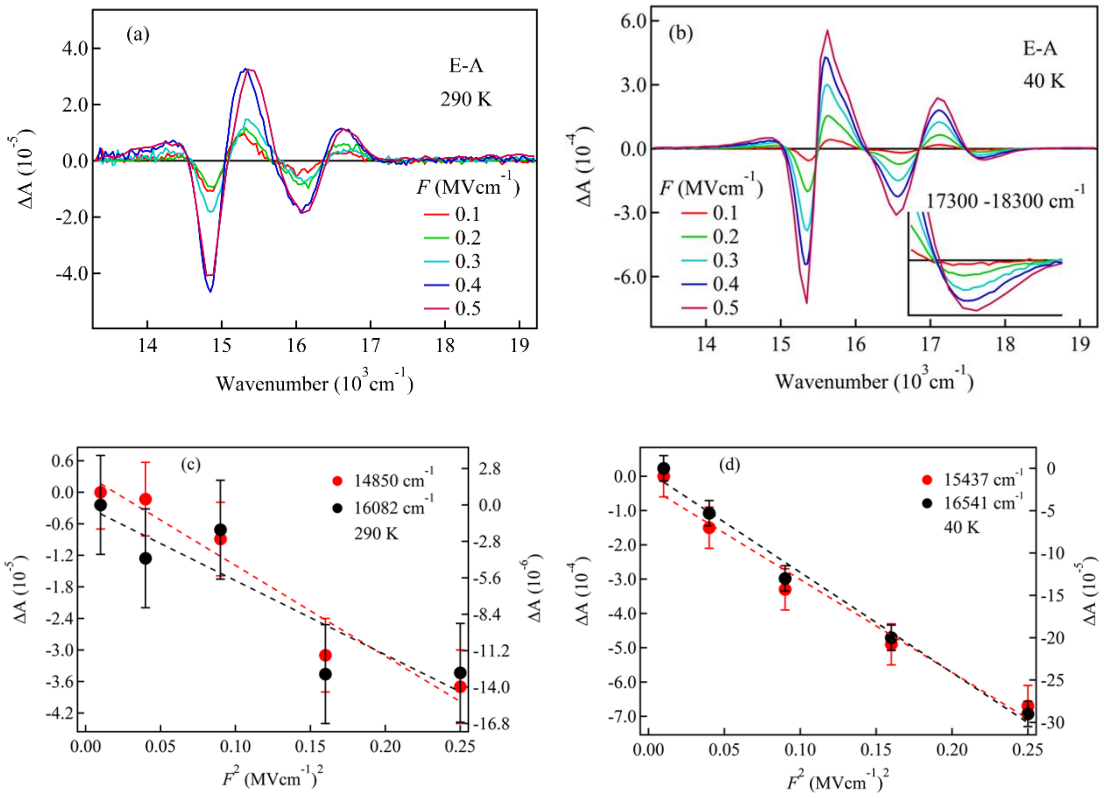

Figure 6.4. E-A spectra of MoS_2 thin film observed with different electric-field strengths at 290 K (a) and 40 K (b), plots of the dependence of the applied field strength of ΔA as a function of the squared field at 290 K (c) and 40 K (d). The inset of (b) shows an extended view of the E-A spectra at 40 K from 17300-18300 cm^{-1}.

Here, the Stark effect is considered. When an external electric field is applied to the MoS_2 NSs, the energy associated with the absorption transitions may shift to the lower and higher side following the factors $-\Delta\mu-\Delta\alpha F^2/2$, in which $\Delta\mu$ and $\Delta\alpha$ are the difference of electric dipole moment and polarizability between the states concerned, namely the electronically excited state (e) and ground state (g) (i.e., $\Delta\mu = \mu_e - \mu_g$ and $\Delta\alpha = \alpha_e - \alpha_g$). Therefore, the electric field-induced change in the absorption spectrum of MoS_2 NSs at

wavenumber (ν) recorded at the second harmonic (2ν) of modulation frequency, that is, ΔA(ν) is taken as a sum of the zeroth, first, and second derivatives of the absorption intensity A(ν), as shown below [17-19,29-34].

$$\Delta A=(fF)^2\left[A_\chi A(\nu)+B_\chi \nu\frac{d}{d\nu}\left(\frac{A(\nu)}{\nu}\right)+C_\chi \nu\frac{d^2}{d\nu^2}\left(\frac{A(\nu)}{\nu}\right)\right], \quad (6.1)$$

where F = |F| and *f* denotes the internal field factor. A_χ is a zeroth derivative coefficient and drives the field-induced change in a transition moment. The coefficient B_χ is responsible for the spectral shift of absorption bands and arises mainly due to Δα following absorption. At the same time, C_χ is accountable for a spectral broadening of the absorption bands, which occurs mainly due to Δμ. The parameters, Δα and Δμ, can be described in terms of the coefficients B_χ and C_χ, as follows:

$$B_\chi=\frac{\Delta\bar{\alpha}}{2hc} \text{ and } C_\chi=\frac{|\Delta\mu|^2}{6\,h^2c^2}, \quad (6.2)$$

where, Δᾱ represents the trace of Δα (i.e., Δᾱ = (1/3) Tr (Δα)). The absorption spectra of MoS_2 NSs represents the overlap of excitonic bands, and the separation into each band is difficult. Therefore, an integral method is considered to be more advantageous for the E-A spectrum analysis [31]. If an E-A spectrum is stated by equation (6.1), then its integral along the wavenumber is given as follows:

$$\int \Delta A(\nu)d\nu \cong (fF)^2\left[A_\chi\int A(\nu)d\nu+B_\chi A(\nu)+C_\chi\frac{dA(\nu)}{d\nu}\right], \quad (6.3)$$

Further integrating equation (6.3) over the wavenumber gives

$$\int\{\int \Delta A(\nu)d\nu\}d\nu \cong (fF)^2\left[A_\chi\int\{\int A(\nu)d\nu\}d\nu+B_\chi\int A(\nu)d\nu+C_\chi A(\nu)\right], \quad (6.5)$$

The first and second terms on the right-hand side of the equation (4) show monotonic increments/decrements as a function of ν, depending on the sign of the coefficients Aχ and Bχ. The third term of Eq. (6.4) is equivalent to the absorption spectrum in shape. The absorption spectrum is decomposed into seven Gaussian bands, i.e., g1-g6 and X, to simulate the observed E-A spectra. The band positions are given in Table 6.1.

Table 6.1: Peak positions of g1, g2, g3, g4, g5, g6 and X bands of absorption bands in wavenumbers (cm^{-1}).

Temperature (K)	**g1 Band (cm^{-1})**	**g2 Band (cm^{-1})**	**g3 Band (cm^{-1})**	**g4 Band (cm^{-1})**	**g5 Band (cm^{-1})**	**g5 Band (cm^{-1})**	**X Band (cm^{-1})**
290 K	14144	14706	15625	17825	21231	25000	16260
250 K	14245	14793	15798	17921	21322	25063	16367
200 K	14347	14970	16000	17921	21231	25000	16367
150 K	14430	14993	16000	18018	21322	25189	16529
100 K	14514	15152	16077	18018	21413	25189	16639
40 K	14620	15152	16181	18018	21413	25189	16722

The peak position, intensity and band shape, i.e., band-width, of these bands as well as the coefficients Aχ, Bχ and Cχ were determined to reproduce the absorption spectrum, E-A spectra and their first and second integral spectra. These data at different temperatures are summarized in Table 6.2. The simulated E-A and integral spectra at 290 K and 40 K are presented in Figure 6.5. The magnitudes of the change in electric dipole moment ($|\Delta\mu|$) and polarizability ($\Delta\bar{\alpha}$) were determined with Eq. (6.2) at each temperature in the range of 290-40 K. The results are summarized in Table 6.3. The X band was not necessary to reproduce the absorption spectra. However, this band was necessary to reproduce was necessary to reproduce the E-A spectra.

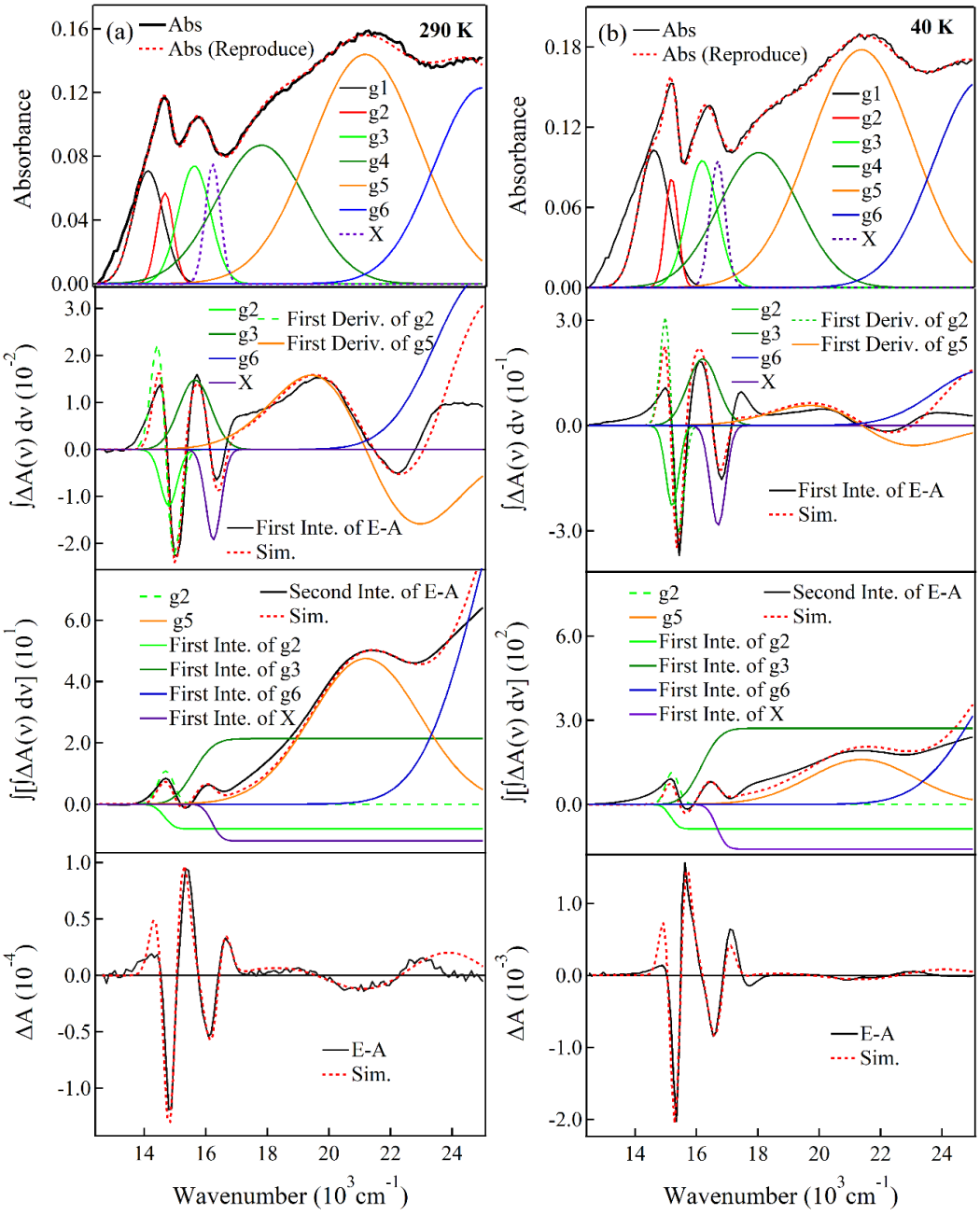

Figure 6.5. Integral analysis of the E-A spectra of MoS_2 thin-film obtained at 290 K (a), 40 K (b). From top to bottom, the absorption spectrum along with the Gaussian bands g1-X, the first integral of the E-A spectrum and first derivative of g2 and g5 spectrum along with g2, g3, g6 and X bands, the second integral of the E-A spectrum and first integral of g2, g3, g6 and X bands along with g2 and g5 bands, and the E-A spectra along with the simulated spectra (bottom).

For which the absorption band intensity was assumed to be one-twentieth of the g3 band at the peak. The E-A spectra obtained at each temperature could be reproduced with a linear combination of the derivatives of g2, g3, g5, g6 and X bands. With decreasing temperature from 290 to 100 K, the magnitude of $|\Delta\mu|$ and $\Delta\bar{\alpha}$ increases for the band g2, i.e., 4.2 D and -30 $Å^3$ at 290 K and 10.9 D and -286 $Å^3$ at 100 K, respectively. For the g3 band, the $\Delta\bar{\alpha}$ value increases with decreasing temperature, i.e., 30 $Å^3$ at 290 K and 357 $Å^3$ at 100 K. The second derivative and first-derivative of the absorption spectrum mainly contributes to the E-A spectrum for the g5 and g6 bands, respectively, and both $|\Delta\mu|$ for g5 and $\Delta\bar{\alpha}$ for g6 increase with decreasing temperature, i.e., 5.2 D at 290 K and 9.3 D at 100 K for g5 and 45.7 $Å^3$ at 290 K and 172 $Å^3$ at 100 K for g6. The first derivative of the X band has a significant contribution to the E-A spectrum, indicating that the magnitude of $\Delta\bar{\alpha}$ increased with decreasing temperature, i.e., -728 $Å^3$ at 290 K and -8568 $Å^3$ at 100 K. The g1 and g4 bands do not contribute to the E-A spectrum at any temperature. For the g2, g3, g6 and X bands, the plots of $\Delta\bar{\alpha}$ *vs.* temperature show a nearly linear relation, *i.e.*, the value of $\Delta\bar{\alpha}$ increased monotonically with decreasing temperature. The magnitude of $|\Delta\mu|$ also increases with decreasing temperature, as observed for g2 and g5 bands. Both $|\Delta\mu|$ and $\Delta\bar{\alpha}$ values are found maximum at 100 K and nearly constant thereafter. Thus, both $|\Delta\mu|$ and $\Delta\bar{\alpha}$, which are directly related to the charge separation and electron distribution following photoexcitation are very sensitive to the temperature. A large value of $|\Delta\mu|$ implies a charge transfer from chalcogen (S) to Mo following absorption, which substantially enhances with decreasing temperature, as observed for the g2 and g5 bands. The weak negative peak observed at low temperatures in the region of 17000 – 18500 cm^{-1} could not be reproduced (see Figure 6.5 at 40 K). This peak was not observed at a high temperature of 290 K (see Figure 6.4a). As shown in Figure 6.4b, the spectral shape in this region depends on the applied field strength, and the zero-crossing point at around 17483 cm^{-1} as well as the

minimum position located between 17857 cm^{-1} and 17544 cm^{-1} shows a blue shift with increasing applied field strength. Further, a positive signal again appeared in the shorter wavelength region than the zero-crossing at around 18349 cm^{-1}. Then, this negative E-A signal may be assigned to the F-K oscillation, which is familiar in the band-edge absorption of semiconductor materials [32]. Note that the shape of the E-A spectra caused by the Stark effect, given by Eq. (6.1), is independent of the applied field strength.

The observed absorption spectra were reproduced with a linear combination of six Gaussian bands, but only g2, g3 g5, g6 and X bands are required to reproduce the E-A spectra. The g1 and g4 bands have a negligible contribution in the E-A spectrum, whereas the band X substantially contributes. The g1, g2, g3 and X bands show a blue shift with decreasing temperature, but the separation between g1 and g2 and between g3 and X is nearly independent of the temperature, as shown in Table 6.1. Based on the E-A analysis of the transistor configuration of the MoS_2 layer, it has been emphasized that the excitonic band A that appeared at 1.9 eV is an overlapping of two electronic resonances, namely (A^0) and (A^-) [20]. Then, g1, g2, g3 and X bands may be considered of splitting of A and B excitonic bands and assigned to the (A^-), (A0) and (B^-), (B0) resonances, respectively, which behave differently with the applied field. The g1 band assigned to the (A^-) feature does not contribute to the overall E-A spectrum. However, the relatively narrow band (g2) corresponding to the exciton contributes significantly to the E-A spectrum. Likewise, the g3 and X bands corresponding to the (B^-) and (B^0) features substantially contribute to the E-A spectrum. It is stressed that the exciton X band, which is not clear in the absorption spectra, contributes largely to the E-A spectra. In monolayer MoS_2 NS, the exciton band B of the absorption spectrum consists of two overlapping electronic resonances, i.e., (B^0) and (B^-), where (B^0) from the neutral ground state to a neutral exciton state and (B^-) from a charged ground state to a charged exciton state (trion) [20,35] Thus, it has been concluded

that in multilayer MoS_2 NSs both A and B excitonic bands consist of the two resonance bands, which depend on the applied electric field. For example, the $|\Delta\mu|$ and $\Delta\bar{\alpha}$ values of corresponding transitions increase substantially with lowering the temperature. The $|\Delta\mu|$ value increased about two times whereas $\Delta\bar{\alpha}$ more than ten times. These values do not further increase upon lowering the temperature below 100 K. It can be mentioned that the amount of charge transfer following photoexcitation increases significantly upon lowering the temperature.

Table 6.2: The coefficients of Aχ, Bχ, and Cχ of Eq. 1 derived from the E-A spectra at different temperatures of MoS_2 with the Integral Method Analysis.

Temp. (K)	**g2 band**		**g3 band**	**g5 band**	**g6 band**	**X band**
	B_χ	C_χ	B_χ	C_χ	B_χ	B_χ
290 K	-0.21	200	0.20	320	0.32	-5.1
250 K	-1.00	650	1.00	500	0.80	-25
200 K	-1.80	1100	2.00	800	0.80	-40
150 K	-1.95	1300	2.40	1000	1.10	-50
100 K	-2.00	1400	2.50	1000	1.20	-60
40 K	-2.00	1400	2.50	1000	1.20	-60

Note: B_χ (cm MV^{-2}) and C_χ (MV^{-2})

Table 6.3: Magnitudes of $|\Delta\mu|$ and $\Delta\bar{\alpha}$ for g2, g3, g5, g6 and X bands at the different temperature of MoS_2 thin film.

T (K)	g2 band		g3 band	g5 band	g6 band	X band
	Change in Electric dipole moment	Change in Polarizability	Change in Polarizability	Change in Electric dipole moment	Change in Polarizability	Change in Polarizability
	$\|\Delta\mu\|$ (D)	$\Delta\bar{\alpha}$ (Å^3)	$\Delta\bar{\alpha}$ (Å^3)	$\|\Delta\mu\|$ (D)	$\Delta\bar{\alpha}$ (Å^3)	$\Delta\bar{\alpha}$ (Å^3)
290 K	4.2	-30	30	5.2	45.7	-728
250 K	7.4	-143	143	6.5	114	-3570
200 K	9.7	-257	286	8.2	114	-5712
150 K	10.5	-278	343	9.3	157	-7140
100 K	10.9	-286	357	9.3	172	-8568
40 K	10.9	-286	357	9.3	172	-8568

Note: Intensity of the X band was assumed to be 20 time smaller than the intensity of g3 band.

6.4 Conclusions

MoS_2 NSs were synthesized with a hydrothermal method. The crystallinity and layered structure of the MoS_2 NSs were confirmed with HRTEM images and temperature-dependent XRD patterns. The layers of MoS_2 NSs are well stacked with an interlayer distance of 0.66 nm. The absorption and E-A spectra of MoS_2 NSs as a function of temperature (290-40 K) and electric field strength (0.1-0.5 MVcm^{-1}) have been measured in vacuum conditions, and E-A spectra were analyzed with an integral method by assuming that the E-A signal arises from the Stark shift. Both A and B excitonic bands are splitting into the resonance states. The values of $|\Delta\mu|$ and $\Delta\bar{\alpha}$ for excitonic resonances increased with lowering the temperature and became constant at around 100 K. The values of

$|\Delta\mu|$ and $\Delta\tilde{\alpha}$ were estimated for excitonic resonances at different temperatures. The X band exhibits massive changes in $\Delta\tilde{\alpha}$, depending on temperature, likely because of a temperature-dependent lattice deformation. The transitions from a charged ground state to charged exciton states, *i.e.*, the trion transitions, were also noticed in MoS_2 NSs, corresponding to A and B excitonic bands. Thus, the study is essential for optoelectronic device operation where the application of electric field is essential.

References

(1) Zheng, L.; Chen, Y.; Li, N.; Zhang, J.; Liu, N.; Liu, J.; Dang, W.; Deng, B.; Li, Y.; Gao, X.; et al., H. Robust Ultraclean Atomically Thin Membranes for Atomic-Resolution Electron Microscopy. Nat. Commun. 2020, 11,541.

(2) Arao, Y.; Kuwahara, R.; Ohno, K.; Tanks, J.; Aida, K.; Kubouchi, M.; Takeda, S.ichi. Mass Production of Low-Boiling Point Solvent-And Water-Soluble Graphene by Simple Salt-Assisted Ball Milling. Nanoscale Adv. 2019, 12, 4955–4964.

(3) Chen, Y.; Fan, Z.; Zhang, Z.; Niu, W.; Li, C.; Yang, N.; Chen, B.; Zhang, H. Two-Dimensional Metal Nanomaterials: Synthesis, Properties, and Applications. Chem. Rev. 2018, 118 (13), 6409–6455.

(4) Jin, H.; Guo, C.; Liu, X.; Liu, J.; Vasileff, A.; Jiao, Y.; Zheng, Y.; Qiao, S. Z. Emerging Two-Dimensional Nanomaterials for Electrocatalysis. Chem. Rev. 2018, 118 (13), 6337–6408.

(5) Xu, M.; Liang, T.; Shi, M.; Chen, H. Graphene-like Two-Dimensional Materials. Chem. Rev. 2013, 113, 3766–3798.

(6) Radisavljevic, B.; Radenovic, A.; Brivio, J.; Giacometti, V.; Kis, A. Single-Layer MoS_2 Transistors. Nat. Nanotechnol. 2011, 6, 147–150.

(7) Varrla, E.; Backes, C.; Paton, K. R.; Harvey, A.; Gholamvand, Z.; McCauley, J.; Coleman, J. N. Large-Scale Production of Size-Controlled MoS_2 Nanosheets by Shear Exfoliation. Chem. Mater. 2015, 27 (3), 1129–1139.

(8) Zhou, W.; Zou, X.; Najmaei, S.; Liu, Z.; Shi, Y.; Kong, J.; Lou, J.; Ajayan, P. M.; Yakobson, B. I.; Idrobo, J.C. Intrinsic Structural Defects in Monolayer Molybdenum Disulfide. Nano Lett. 2013, 13, 2615-2622.

(9) Jaiswal, H. N.; Liu, M.; Shahi, S.; Yao, F.; Zhao, Q.; Xu, X.; Li, H. Localized Surface Plasmon Resonance on Two-Dimensional $HfSe_2$ and $ZrSe_2$. Semicond. Sci. Technol. 2018, 33, 124014.

(10) Sharma, P.; Mehata, M. S. Colloidal MoS_2 Quantum Dots Based Optical Sensor for Detection of 2,4,6-TNP Explosive in an Aqueous Medium. Opt. Mater. 2020, 100, 109646.

(11) Sharma, P.; Mehata, M. S. Rapid Sensing of Lead Metal Ions in an Aqueous Medium by MoS_2 quantum Dots Fluorescence Turn-Off. Mater. Res. Bull. 2020, 131, 110978.

(12) Pham, T.; Li, G.; Bekyarova, E.; Itkis, M. E.; Mulchandani, A. MoS_2-Based Optoelectronic Gas Sensor with Sub-Parts-per-Billion Limit of NO_2 Gas Detection. ACS Nano 2019, 13 (3), 3196–3205.

(13) Kim, Y.; Bark, H.; Kang, B.; Lee, C. Wafer-Scale Substitutional Doping of Monolayer MoS_2 Films For High-Performance Optoelectronic Devices. ACS Appl. Mater. Interfaces 2019, 11 (13), 12613–12621.

(14) Parzinger, E.; Miller, B.; Blaschke, B.; Garrido, J. A.; Ager, J. W.; Holleitner, A.; Wurstbauer, U. Photocatalytic Stability of Single- And Few-Layer MoS_2. ACS Nano 2015, 9 (11), 11302–11309.

(15) Singh, M. K.; Mehata, M. S. Enhanced Photoinduced Catalytic Activity of Transition Metal Ions Incorporated TiO_2 Nanoparticles for Degradation of Organic Dye: Absorption and Photoluminescence Spectroscopy. Opt. Mater.2020, 109, 110309.

(16) Singh, M. K.; Mehata, M. S. Phase-Dependent Optical and Photocatalytic Performance of Synthesized Titanium Dioxide (TiO_2) Nanoparticles. Optik 2019, 193, 163011.

(17) Ohta, N. Electric Field Effects on Photochemical Dynamics in Solid Films. Bull. Chem. Soc. Jpn. 2002, 75, 1637–1655.

(18) Jalviste, E.; Ohta, N. Theoretical Foundation of Electroabsorption Spectroscopy: Self-Contained Derivation of the Basic Equations with the Direction Cosine Method and the Euler Angle Method. J. Photochem. Photobiol. C Photochem. Rev. 2007, 8, 30–46.

(19) Ohta, N.; Awasthi, K.; Okoshi, K.; Manseki, K.; Miura, H.; Inoue, Y.; Nakamura, K.; Kono, H.; Diau, E. W. G. Stark Spectroscopy of Absorption and Emission of Indoline Sensitizers: A Correlation with the Performance of Photovoltaic Cells. J. Phys. Chem. C 2016, 120, 26206–26216.

(20) Vella, D.; Ovchinnikov, D.; Martino, N.; Vega-Mayoral, V.; Dumcenco, D.; Kung, Y.-C.; Antognazza, M.-R.; Kis, A.; Lanzani, G.; Mihailovic, D.; et al., Unconventional Electroabsorption in Monolayer MoS_2. 2D Mater. 2017, 4, 021005.

(21) Chaudhary, N.; Khanuja, M.; Abid; Islam, S. S. Hydrothermal Synthesis of MoS_2 Nanosheets for Multiple Wavelength Optical Sensing Applications. Sensors Actuators, A Phys. 2018, 277, 190–198.

(22) Umeuchi, S.; Nishimura, Y.; Yamazaki, I.; Murakami, H.; Yamashita, M.; Ohta, N. Electric Field Effects on Absorption and Fluorescence Spectra of Pyrene Doped in a PMMA Polymer Film. Thin Solid Films 1997, 311, 239–245.

(23) Beal, A. R.; Knights, J. C.; Liang, W. Y. Transmission Spectra of Some Transition Metal Dichalcogenides. I. Group IVA: Octahedral Coordination. J. Phys. C Solid State Phys. 1972, 5, 3531–3539.

(24) Murray, R. B.; Yoffe, A. D. The Band Structures of Some Transition Metal Dichalcogenides: Band Structures of the Titanium Dichalcogenides. J. Phys. C Solid State Phys. 1972, 5, 3038–3046.

(25) Liu, G.; Ma, H.; Teixeira, I.; Sun, Z.; Xia, Q.; Hong, X.; Tsang, S. C. E. Hydrazine-Assisted Liquid Exfoliation of MoS_2 for Catalytic Hydrodeoxygenation of 4-Methylphenol. Chem.- A Eur. J. 2016, 22, 2910–2914.

(26) Ahmad, R.; Srivastava, R.; Yadav, S.; Singh, D.; Gupta, G.; Chand, S.; Sapra, S. Functionalized Molybdenum Disulfide Nanosheets for 0D-2D Hybrid Nanostructures: Photoinduced Charge Transfer and Enhanced Photoresponse. J. Phys. Chem. Lett. 2017, 8, 1729–1738.

(27) Wang, K.; Wang, J.; Fan, J.; Lotya, M.; O'Neill, A.; Fox, D.; Feng, Y.; Zhang, X.; Jiang, B.; Zhao, Q.; Zhang, H.; Coleman, J.N.; Zhang, L.; Blau, W.J. Ultrafast Saturable Absorption of Two-Dimensional MoS_2 Nanosheets. ACS Nano 2013, 7, 9260–9267.

(28) Yalon, E.; Aslan, Ö. B.; Smithe, K. K. H.; McClellan, C. J.; Suryavanshi, S. V.; Xiong, F.; Sood, A.; Neumann, C. M.; Xu, X.; Goodson, K. E.; et al. Temperature-Dependent Thermal Boundary Conductance of Monolayer MoS_2 by Raman Thermometry. ACS Appl. Mater. Interfaces 2017, 9, 43013–43020.

(29) Bublitz, G. U.; Boxer, S. G. Stark Spectroscopy: Applications in Chemistry, Biology, and Materials Science. Annu. Rev. Phys. Chem. 1997, 48, 213–242.

(30) Locknar, S. A.; Peteanu, L. A. Investigation of the Relationship between Dipolar Properties and Cis-Trans Configuration in Retinal Polyenes: A Comparative Study Using Stark Spectroscopy and Semiempirical Calculations. J. Phys. Chem. B 1998, 102, 4240–4246.

(31) Awasthi, K.; Iimori, T.; Ohta, N. Integral Method Analysis of Electroabsorption Spectra and Its Application to Quantum Dots of PbSe. J. Phys. Chem. C 2014, 118, 18170–18176.

(32) Rana, S.; Awasthi, K.; Bhosale, S. S.; Diau, E. W. G.; Ohta, N. Temperature-Dependent Electroabsorption and Electrophotoluminescence and Exciton Binding Energy in $MAPbBr_3$ Perovskite Quantum Dots. J. Phys. Chem. C 2019, 123, 19927–19937.

(33) Kattoor, V.; Awasthi, K.; Jokar, E.; Diau, E. W. G.; Ohta, N. Integral Method Analysis of Electroabsorption Spectra and Electrophotoluminescence Study of $(C_4H_9NH_3)_2PbI_4$ Organic-Inorganic Quantum Well. J. Phys. Chem. C 2018, 122, 26623–26634.

(34) Mehata, M. S.; Iimori, T.; Yoshizawa, T.; Ohta, N. Electroabsorption Spectroscopy of 6-Hydroxyquinoline Doped in Polymer Films: Stark Shifts and Orientational Effects. J. Phys. Chem. A 2006, 110, 10985–10991.

(35) Mak, K. F.; He, K.; Lee, C.; Lee, G. H.; Hone, J.; Heinz, T. F.; Shan, J. Tightly Bound Trions in Monolayer MoS_2. Nat. Mater. 2013, 12, 207–211.

Chapter-7

Summary and Scope of Future Work

7.1 Summary

The research topic of the thesis entitled "*Investigations of Metal Assisted Titanium Dioxide (TiO_2) Nanocrystals*" disclosed the structural, morphological, compositional and optical properties of TiO_2 nanoparticles (NPs) and discussed their utility for photocatalytic applications.

In the current thesis, TiO_2 NPs were prepared using the sol-gel method and comprehensively explored their properties. The crystalline structural and optical characteristics of TiO_2 NPs (like X-ray diffraction, absorption, photoluminescence, and time-resolved photoluminescence) along with photocatalytic applications have also been discussed in detail in the previous chapter.

7.2 Important Findings of Research Work

Nanocrystals of anatase, mixed and rutile phases of TiO_2 and metal-doped TiO_2 have been synthesized via the sol-gel method. The prepared samples were characterized by various analytical tools. For the structural and surface morphology analysis, essential tools such as XRD, SEM and TEM were used. EDX analysis has been carried out for elemental identification present in prepared nanomaterials. TGA, FTIR spectroscopy, Raman spectroscopy, UV-visible & PL spectroscopy, time-resolved photoluminescence (TRPL) spectroscopy at varying temperatures were used to understand the structural and transitions following photoexcitation.

TiO_2 NPs were prepared by the sol-gel method with titanium isopropoxide as a precursor at different annealing temperatures. The analyzed XRD patterns, Raman and Fourier transform infrared spectra demonstrated the structural transformation from

amorphous to anatase and further to rutile phase while increasing annealing temperature. In addition, a mixed-phase of TiO_2 NPs is formed, which consists of both phases. The absorption and photoluminescence (PL) spectra of mixed and rutile phases are shifted towards a longer wavelength region. The indirect band gap structure changed into the direct band gap during the structural transformation. Both absorption and PL spectra shifted towards lower energy regions, which might be due to the increase in size or the induced oxygen vacancies produced at a higher temperature.

Furthermore, the photocatalytic activity of all the three different structural TiO_2 NPs was examined. Furthermore, the photocatalytic performance of the different types of TiO_2 NPs was examined through the degradation of a dye, rhodamine B (RhB), under UV radiation and measuring changes in absorption and PL spectra. The anatase phase structure shows higher photocatalytic activity than the rutile phase. However, the mix phase has the highest photocatalytic activity among all the structures, which degraded RhB entirely at a faster rate. On the other hand, the rutile phase is unable to take part in this process. Thus, the mix phase of TiO_2 NPs is beneficial for industrial and environmental applications.

The transition metal ions (Ag^+, Cu^{2+}, and Ni^{2+}) doped and undoped TiO_2 NPs have been synthesized using a cost-effective sol-gel method with a 1.0 wt% dopant concentration. The microstructure and chemical compositions of these NPs were examined using various techniques such as x-ray diffractometric, field emission scanning electron microscopy, high-resolution transmission electron microscopy, Fourier transform infrared and absorption and photoluminescence (PL) spectroscopy. The absorption and photoluminescence (PL)-excitation spectra of metal-doped TiO_2 NPs are shifted to the longer wavelength region, which indicates a reduced bandgap than the bare TiO_2 NPs. The absorption and PL spectra of methylene blue (MB) in the presence of undoped and metal ions doped TiO_2 NPs show dramatic changes upon UV-irradiation. The absolute absorption

intensity reduced entirely and the solution of MB became colorless in the presence of UV irradiation. The PL of the degraded dye exhibits a new band in the shorter wavelength region, which has a multi-exponential decay function and an increased average PL lifetime. The dye degradation rate is higher for metal ions doped catalyst and highest for Cu^{2+} doped TiO2 NPs. Thus, Cu ions-doped TiO_2 shows the highest photocatalytic activity. The order of catalytic degradation rate under UV irradiation was found to be Cu– TiO_2 > Ni– TiO_2 >Ag– TiO_2 >anatase TiO_2. The analysis of the PL spectra and PL-decays reveals the formation of smaller species that emits at a shorter wavelength region, thus helps in understanding the degradation of dye molecules.

TiO_2 NPs synthesized by employing the sol-gel routes and annealed at a different temperature from 400 to 900 °C. Three different nanostructures were formed, namely anatase, mixed (anatase/rutile) and rutile phases. The structure and morphology of as-synthesized NPs were confirmed using XRD and FESEM analysis. The XRD analysis of TiO_2 NPs was carried out in the 290 K to 77 K temperature range and found no significant change in XRD patterns that means thermally stable TiO_2 NPs. The PL spectra and contour maps of TiO_2 NPs show that the anatase phase falls in the visible region. However, mixed and rutile phases fall in both visible and NIR regions as the temperature decreases from 290 K to 77 K. The visible PL band is ascribed to donor-acceptor recombination. In contrast, oxygen vacancies serve as donors and hydroxyl groups function as accepter sites. NIR PL band attributed to the trapped electrons in rutile TiO_2, which recombine with free holes and intrinsic defects. The fast component of the decay processes was aided by the immediate formation of trapped electrons in luminescence sites. The indirect trap processes were responsible for the power-law component in the rutile phase, which was the recombination of trapped electrons formed via a deep trap state. It was observed that the electron-hole pairs thermally separated, preventing the formation of STEs directly. The PL

and PL decay studies under weak excitation conditions prove to be a more valuable and appropriate method to evaluate the trap states distribution and their carrier dynamic effects, which were vibrant to understand the photocatalytic processes better.

Two-dimensional (2D) layered MoS_2 nanosheets (NSs), which possess a vast range of unique properties and hold great potential for various applications. MoS_2 NSs were synthesized by a hydrothermal method and the obtained NSs bear crystalline and layered structure. Absorption and electroabsorption (E-A) spectra of MoS_2 doped in a PMMA thin film were measured at different temperatures (290-40 K). The E-A spectra observed at the second harmonic of the modulation frequency of the applied electric field (1.0 kHz) were analyzed with an integral method by assuming the Stark effect as a dominant feature. The absorption spectra consist of multiple transitions, among which five transitions are contributed to the E-A spectra. The changes in electric dipole moment ($\Delta\mu$) and polarizability ($\Delta\alpha$) of each transition were determined at different temperatures. Two electronic resonance states were identified for two excitonic bands of MoS_2 NSs, which showed a strong E-A signal

7.3 Future Scope of the Work

- To synthesis the nanocrystal of TiO_2 doped with alkaline, transition metals and rare earth metals via different techniques such as sol-gel, hydrothermal and CVD.
- To study the structural, optical, electrical, magnetic, dielectric, thermal and morphological properties of prepared nanomaterials have to elucidate.
- To synthesize the nanocomposite nanomaterials to enhance the photocatalytic properties and use in batteries application.
- To investigate the photocatalytic activity of other organics dyes (Rhodamine Blue, Brilliant Green, Congo Red, etc.)
- To study the antibacterial of various prepared types of nanomaterials.